



Valentin Dzhankhotov

**HYBRID LC FILTER FOR POWER ELECTRONIC DRIVES:
THEORY AND IMPLEMENTATION**

Thesis for the degree of Doctor of Science (Technology) to be presented with due permission for public examination and criticism in the auditorium 1382 at Lappeenranta University of Technology, Lappeenranta, Finland on the 23th of October, 2009, at noon.

Acta Universitatis
Lappeenrantaensis
354

- Supervisors Professor Juha Pyrhönen
Lappeenranta University of Technology
Finland
- Professor Pertti Silventoinen
Lappeenranta University of Technology
Finland
- Reviewers Professor Emeritus Tapani Jokinen
Department of Electrical Engineering
Helsinki University of Technology
Finland
- Professor Valery Vodovozov
Faculty of Power Engineering:
Department of Electrical Drives and Power Electronics
Tallinn University of Technology
Estonia
- Opponents Professor Emeritus Tapani Jokinen
Department of Electrical Engineering
Helsinki University of Technology
Finland
- Professor Valery Vodovozov
Faculty of Power Engineering:
Department of Electrical Drives and Power Electronics
Tallinn University of Technology
Estonia

ISBN 978-952-214-826-1
ISBN 978-952-214-827-8 (PDF)
ISSN 1456-4491

Lappeenranta Teknillinen Yliopisto
Digipaino 2009

Abstract

Kand. Nauk Valentin Dzhankhotov

Hybrid LC Filter for Power Electronic Drives: Theory and Implementation

Lappeenranta, 2009

110 p.

Acta Universitatis Lappeenrantaensis 354

Diss. Lappeenranta University of Technology

ISBN 978-952-214-826-1, ISBN 978-952-214-827-8 (PDF)

ISSN 1456-4491

Power electronic converter drives use, for the sake of high efficiency, pulse-width modulation that results in sequences of high-voltage high-frequency steep-edged pulses. Such a signal contains a set of high harmonics not required for control purposes. Harmonics cause reflections in the cable between the motor and the inverter leading to faster winding insulation ageing. Bearing failures and problems with electromagnetic compatibility may also result.

Electrical du/dt filters provide an effective solution to problems caused by pulse-width modulation, thereby increasing the performance and service life of the electrical machines. It is shown that RLC filters effectively decrease the reflection phenomena in the cable. Improved (simple, but effective) solutions are found for both differential- and common-mode signals; these solutions use a galvanic connection between the RLC filter star point and the converter DC link.

Foil chokes and film capacitors are among the most widely used components in high-power applications. In actual applications they can be placed in different parts of the cabinet. This fact complicates the arrangement of the cabinet and decreases the reliability of the system. In addition, the inductances of connection wires may prevent filtration at high frequencies.

This thesis introduces a new hybrid LC filter that uses a natural capacitance between the turns of the foil choke based on integration of an auxiliary layer into it. The main idea of the hybrid LC filter results from the fact that both the foil choke and the film capacitors have the same roll structure. Moreover, the capacitance between the turns (“intra capacitance”) of the foil inductors is the reason for the deterioration of their properties at high frequencies. It is shown that the proposed filter has a natural cancellation of the intra capacitance. A hybrid LC filter may contain two or more foil layers isolated from each other and coiled on a core. The core material can be iron or even air as in the filter considered in this work. One of the foils, called the main foil, can be placed between the inverter and the motor cable. Other ones, called auxiliary foils, may be connected in star to create differential-mode noise paths, and then coupled to the DC link midpoint to guarantee a travelling path, especially for the common-mode currents. This way, there is a remarkable capacitance between the main foil and the auxiliary foil. Investigations showed that such a system can be described by a simple equivalent LC filter in a wide range of frequencies.

Because of its simple hybrid construction, the proposed LC filter can be a cost-effective and competitive solution for modern power drives. In the thesis, the application field of the proposed filter is considered and determined. The basics of hybrid LC filter design are developed further. High-frequency behaviour of the proposed filter is analysed by simulations. Finally, the thesis presents experimental data proving that the hybrid LC filter can be used for du/dt of PWM pulses and reduction of common-mode currents.

Keywords: power drives, du/dt filters, common-mode filters, bearing currents, filter design.

UDC 621.372: 621.314

“In our endeavour to understand reality we are somewhat like a man trying to understand the mechanism of a closed watch. He sees the face and the moving hands, even hears it ticking, but he has no way of opening the case. If he is ingenious he may form some picture of the mechanism which could be responsible for all the things he observes, but he may never be quite sure his picture is the only one which could explain his observations. He will never be able to compare his picture with the real mechanism and he cannot even imagine the possibility of the meaning of such a comparison.”

(Albert Einstein: The Evolution of Physics)

Acknowledgements

This study has mainly been carried out at the Department of Electrical Engineering of Lappeenranta University of Technology (LUT) during the years 2006–2009 in close interaction with the R&D Department of The Switch High Power Converters. A large number of people in Finland and Russia, including the Control Systems Department of Saint-Petersburg State Electrotechnical University LETI, significantly contributed to the research work.

I express my deep gratitude to my supervisors, Professors Juha Pyrhönen and Pertti Silventoinen as well as to Dr. Mikko Kuisma at Lappeenranta University of Technology for their valuable guidance and new knowledge obtained during the work. I thank Professor Jero Ahola for valuable comments, Mr. Martti Lindh for his essential help in the laboratory, Mr. Harri Loisa for building the prototypes, Ms. Julia Vauterin for her sincere support in the educational processes, Dr. Hanna Niemelä for language edition and all the team of the Department of Electrical Engineering of Lappeenranta University of Technology (LUT) for their contributions to this work.

I thank my superiors at The Switch Dr. Olli Pyrhönen, Dr. Alpo Vallinmäki and Dr. Riku Pöllänen as well as the whole R&D team at The Switch High Power Converters for the time of working together in a great scientific atmosphere; I wish a bright future for all of them. I address my special thanks to Mr. Sergey Groshev for his support and valuable comments.

I acknowledge the help of Professors Viktor Putov, Viktor Vtorov and Alexander Mikerov for their support from Saint-Petersburg Electrotechnical University LETI.

I thank my pre-examiners Professor Tapani Jokinen and Professor Valery Vodovozov for their valuable comments and corrections.

Finally, this work is dedicated to my parents Viktor and Tamara as well as to my sister Anna. Your love is my breath.

Valentin Dzhankhotov,
October 2009,
Lappeenranta, Finland.

CONTENTS

Abstract

Acknowledgements

Contents

Nomenclature.....11

1 Introduction17

1.1 Pulse-width modulation and its adverse effects	17
1.2 Drive as a high-frequency electrical circuit	18
1.2.1 Diode bridge and DC link	19
1.2.2 PWM inverter	19
1.2.3 Cable between the inverter and the motor.....	22
1.2.4 Motor.....	26
1.2.5 Power tool and sensors	29
1.3 Bearing currents	29
1.3.1 Electrical discharge machining	30
1.3.2 Circulating currents	30
1.3.3 Shaft earthing current	32
1.4 Mitigation of the adverse effects of pulse-width modulation.....	33
1.5 PWM inverter output filters	34
1.6 Hybrid LC filter.....	37
1.7 Objectives and scope of the thesis.....	39

2 Hybrid LC filter design.....40

2.1 Required range of common-mode attenuation	40
2.2 Selection of materials	43
2.3 Calculation technique	45
2.4 Hybrid LC filter design technique.....	52
Summary of Chapter 2	60

3 Hybrid LC filter in the frequency domain.....61

3.1 Simplified electrical representation of a hybrid LC filter at low frequencies	61
3.2 Hybrid LC filter electrical characteristics in the frequency domain	62
3.3 Current redistribution effect	68
3.4 Consideration of the main alternatives of the secondary foil earthing.....	70
3.5 Hybrid LC filter model.....	73
3.6 Hybrid LC filter simulations in the time domain	77
Summary of Chapter 3	80

4 Experimental investigations of the hybrid LC filter81

4.1 Drive setup description.....	81
4.2 Background for the analysis of the step response	85

4.3 Test results	86
4.3.1 System without a filter	86
4.3.2 Hybrid LC filter in the choke mode	87
4.3.3 Hybrid LC filter in the du/dt filter mode.....	87
4.3.4 Hybrid LC filter in the du/dt filter mode with a common-mode link	91
4.3.5 Hybrid LC filter with additional resistances	92
Summary of Chapter 4	95
5 Conclusions	96
References	98
Appendix A.....	103

NOMENCLATURE

Roman symbols

A	area between the foils
A_r	magnitude at the resonance frequency
A_{rwr}	magnitude rightward from the resonance frequency
B	field flux density
c	coupling factor
C'_i	intra capacitance with a small-capacitance additional turn
$C_{a,t}$	capacitance of the additional turn
C_b, C_{b1}	main capacitance (capacitance between the main and auxiliary foils)
C_{b2}	hidden capacitance between the main and auxiliary foils due to rolling
C_c	cable elementary component capacitance
C_f	capacitance of a filter
C_{hf}	high-frequency capacitance of the motor
C_i	intra capacitance of the winding
C_{i1}	intra capacitance of the main foil
C_{i2}	intra capacitance of the auxiliary foil
$C_{i-r.e}$	capacitance between the retainer with roller elements and the inner bearing race
C_{o-i}	capacitance between the outer and inner races
$C_{o-r.e}$	capacitance between the retainer with roller elements and the outer bearing race
C_{rf}	capacitance between the rotor and the frame inside of the motor
C_{sf}	capacitance between the stator and the frame inside of the motor
C_{sr}	capacitance between the rotor and the stator inside of the motor
d_{aux}	thickness of the auxiliary foil
d_{foil}	thickness of a foil
d_{frame}	thickness of the hybrid LC filter frame
d_{gap}	gap between each foil surface and the insulation
D_{in}	inner diameter of the hybrid LC filter
d_{ins}	thickness of the insulation layer
d_{ma}	distance between main and auxiliary foils
d_{main}	thicknesses of the main foil
D_{out}	outer diameter of the hybrid LC filter
d_{str}	infinite strip thickness
d_{tt}	distance between the nearest turns
d_w	thickness of the hybrid LC filter winding
e_s	permissible level of signal ripples
f	frequency
f_c	corner frequency of a filter (frequency at which the filter provides 3 dB attenuation)
$f_{c.od}$	cut-off frequency of a filter with an overdamping resistor in series with the capacitance
f_{cR}	cut-off frequency of a filter with a resistor in series with the capacitance
f_{hlz}	frequency at which the linear zone of the high-pass filter starts
$f_{i.stk}$	frequency at which the rise in resistance becomes slower at high frequencies
$f_{i.str}$	frequency at which the resistance of foils cannot be considered constant
f_{llz}	frequency at which the linear zone of the low-pass filter ends
f_{oC}	resonance frequency of the main capacitance and the parasitic inductance
f_{oL}	resonance frequency of the main inductance and the parasitic capacitance

f_r	resonance frequency of the main inductance and the capacitance of the hybrid LC filter
f_{rwr}	frequency rightward from the resonance frequency
G_c	cable elementary component conductance
H	height of an infinite stack and an infinite strip
h	height of the hybrid LC filter
h_D	aspect ratio of a hybrid LC filter
h_{foil}	height of a foil
h_{frame}	height of the hybrid LC filter frame
i_0	current flowing between the filter star point and the DC link midpoint
i_1	current in the main foil
i_2	current in the auxiliary foil
i_A, i_B, i_C	currents in the phases a, b, c
i_{cm}	common-mode current
I_{mfe1}, I_{mfe2}	currents flowing from the motor frame to earth
I_{PE}	protective earth current
I_{pte}	current flowing from the motor shaft to the power-tool earth
I_{sh}	current flowing through the motor shaft
i_{tw}	magnitude of the current travelling wave
k	coefficient for inductance calculation
K_a	coefficient for inductance calculation
K_{hpf}	gain of a high-pass filter
k_m	coefficient taking into account the properties of the insulation and the core
l	length of the hybrid LC filter layer
L_1, L_m	main inductance (inductance of the main foil)
L_a	auxiliary foil inductance
L_{ap}	apparent inductance
L_c	cable elementary component inductance
L_{cab}	cable lumped inductance
L_{cml}	inductance of the common-mode link conductor
l_{cr}	critical length of the cable
L_f	inductance of a filter
L_{hf}	high-frequency inductance of the motor
L_s	network power supply internal impedance
M	mutual inductance
m	mass of the hybrid LC filter column
m_{cov}	mass of the hybrid LC filter cover
M_r	magnitude at the resonance frequency in dB
M_w	mass of the whole hybrid LC filter
N	number of turns of one layer in one column of the hybrid LC filter
n_f	number of foils in one column
N_i	arbitrary turn of the hybrid LC filter winding
Q	quality factor of the filter
Q_t	volumetric heat density
R	resistance
$R_{l,ac}$	AC resistance of the main foil
R_{ac}	AC resistance of a foil
R_c	cable elementary component resistance
R_{dc}	DC resistance of a foil
R_f	resistance of a filter
r_{frame}	radius of the hybrid LC filter frame

R_{hf}	high-frequency resistance of the motor
R_{ib}	resistance of the inner bearing races
R_{in}	inner input resistance of the impedance analyzer
r_{mid}	radius of the centre of the hybrid LC filter winding
R_{ob}	resistance of the outer bearing race
$R_{\text{o-i}}$	resistance between the outer and inner races
R_{out}	inner output resistance of the impedance analyzer
$R_{\text{r.e}}$	resistance of the retainer and the roller elements of a bearing
R_{stk}	resistance of an infinite stack
R_{str}	resistance of an infinite strip
T_{hpf}	time constant of a high-pass filter
T_{lpf}	time constant of a low-pass filter
t_{m}	time instant when the maximum overshoot takes place
T_{o}	period of oscillations
t_{p}	time of signal propagation inside the cable
t_{r}	pulse rise time
$t_{\text{r.od}}$	rise time of pulse of a filter with an overdamping resistor in series with the capacitance
t_{r1}	pulse rise time measured from 10 % to 90 % of the required voltage
t_{rR}	pulse rise time of a filter with a resistor in series with the capacitance
T_{s}	transient response time
$u_{\text{A}}, u_{\text{B}}, u_{\text{C}}$	voltages in the phases a, b, c against earth
u_{CM}	common-mode voltage
$u_{\text{DC link}}$	instantaneous value of the potential difference between the DC link voltage and earth
$U_{\text{DC link}}$	amplitude of the potential difference between the DC link voltage and earth
u_{in}	input voltage
U_{in}	input voltage of the hybrid LC filter
U_{m}	peak voltage
$u_{\text{O'E}}$	voltage between the DC link midpoint and earth
u_{out}	output voltage
U_{out}	output voltage of the hybrid LC filter
u_{req}	required level of output voltage
u_{rfl}	reflected wave magnitude
U_{sh}	potential difference between the motor shaft ends
v	speed of signal propagation inside the cable
V	volume of materials used
V_{aux}	volume of the hybrid LC filter auxiliary foil
V_{frame}	volume of the hybrid LC filter frame
V_{ins}	volume of the hybrid LC filter insulation layer
V_{main}	volume of the hybrid LC filter main foil
$W''_{\text{hlc}(s)}$	hybrid LC filter transfer function with an external resistor
$W'_{\text{hlc}(s)}$	hybrid LC filter transfer function with an internal resistance
$W_{\text{hlc}(s)}$	hybrid LC filter transfer function without resistances
$W_{\text{hpf}(s)}$	transfer function of a high-pass filter
$W_i(s)$	transfer function by current
$W_{\text{lpf}(s)}$	transfer function of a low-pass filter
Z	impedance
$Z_{\text{A}}, Z_{\text{B}}, Z_{\text{C}}$	impedances in the phases a, b, c
Z_{b}	constant part of the bearing impedance
Z_{c}	inductance of the cable
Z_{cm}	common-mode impedance

Z_G	generalized distributed impedance between the motor air-gap and earth
Z_{in}	input impedance (impedance of a converter)
Z_M	motor impedance
Z_{out}	output impedance (impedance of an electrical machine)
$Z_{r-g-r.e}$	nonlinear impedance of a bearing

Greek symbols

α	relation between the hybrid LC filter column height and the middle diameter
Γ	reflection coefficient
γ	relation between the hybrid LC filter column winding thickness and height
Δ	relation between the foil thickness and the skin layer depth
ϵ_0	relative permittivity of vacuum
ϵ_{ins}	relative permittivity of the insulation material
μ	relative permeability of air
μ_0	permeability of the free space
μ_c	relative magnetic permeability of the conductor
ρ	resistivity of the foil material
ρ	relation between the hybrid LC filter column winding thickness and the middle diameter
ρ_{aux}	density of the hybrid LC filter auxiliary foil
ρ_{frame}	density of the hybrid LC filter frame
ρ_{ins}	density of the hybrid LC filter insulation
ρ_m	resistivity of the main foil material
ρ_{main}	density of the main foil
σ	overshoot
σ_m	conductivity of a foil
σ_{od}	overshoot of a filter with an overdamping resistor in series with the capacitance
σ_R	overshoot of a filter with a resistor in series with the capacitance
ω	angular frequency
ω_r	angular resonance frequency of the main inductance and the capacitance of the hybrid LC filter
ω_{rwr}	angular frequency rightward from the resonance frequency
Φ_c	common flux

Subscripts

i	arbitrary element of a circuit
m	maximum value
n	degree of a low-pass filter
n	last element of a circuit

Abbreviations

AC	alternating current
AE	gain-phase analyzer earth-connected terminal of the auxiliary foil
AP	star-point-connected terminal of the auxiliary foil of the hybrid LC filter
CSP	junction of the auxiliary foils in star at cable-connected terminals of the main foils
DC	direct current
EMC	electromagnetic compatibility
HLCF	hybrid LC filter

IEC	International Electrotechnical Commission
IGBT	insulated gate bipolar transistor
ISP	junction of the auxiliary foils in star at inverter-connected terminals of the main foils
MAI	gain-phase analyzer input-connected terminal of the main foil
MAO	gain-phase analyzer output-connected terminal of the main foil
MC	cable-connected terminal of the main foil of the hybrid LC filter
MI	inverter-connected terminal of the main foil of the hybrid LC filter
NEMA	National Electrical Manufacturers Association
PWM	pulse-width modulation

1 Introduction

1.1 Pulse-width modulation and its adverse effects

The demand for high energy efficiency and the desire for accurate process control have made frequency converters the state of the art in the industry. Modern drives (Figure 1.1) usually consist of the motor, various sensors for drive feedback control, a microcontroller for data processing, an insulated-gate-bipolar-transistor-based (IGBT) pulse-width-modulated (PWM) inverter for amplifying the microcontroller signals and a load that is mechanically (and often galvanically) connected to the shaft either directly or through a gear. Such a control is characterized for instance by very good performance, low price, small dimensions and a low mass. At the same time, the PWM pulse patterns contain high-frequency harmonics that can flow through the cable and motor stray capacitances producing differential- and common-mode noises, which are described, for instance, in (Kuisma et al. 2009). The differential-mode noise flows from one phase to other phases as it is predicted for a normal signal. Common-mode noise is an in-phase signal, which flows in the same direction through all phases. Part of the common-mode current flows through the bearings of the motor or driven machinery and results in their premature failure. This is essential, in particular, for high-power drives (Palma et al. 2000, Gambica 2002, Hoppler and Errath 2007). As a rule of thumb, it is often stated that when driven by a PWM inverter, problems are expected to arise at motor frame sizes of 280 mm and larger.

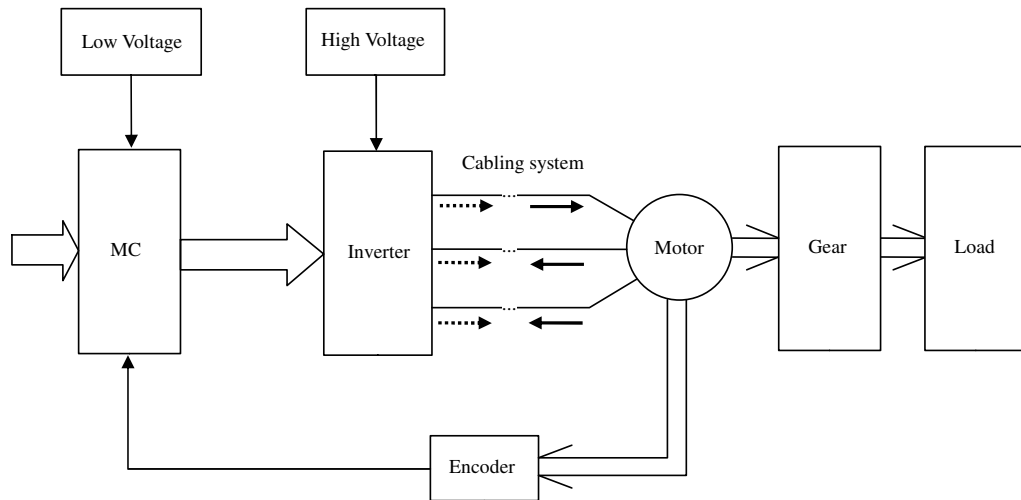


Figure 1.1. Typical industrial AC drive (solid arrows indicate a differential-mode signal and dashed arrows a common-mode signal).

Harmful effects of pulse-width modulation represent a difficult phenomenon. Let us next consider an AC drive as an electrical circuit in detail.

1.2 Drive as a high-frequency electrical circuit

A typical power part of a drive is shown in Figure 1.2. It consists of a sinusoidal three-phase network power supply, a diode bridge (rectifier) for voltage rectification, a DC link for smoothing the rectified voltage, a PWM inverter that amplifies digital control signals, a cabling system and the motor.

Utility network power supply is characterized by its internal inductive impedance shown in Figure 1.2 as the inductance L_s . Network AC voltages pass to a diode bridge consisting of six rectifying diodes D_1 – D_6 . DC voltage rectified by the diode bridge has a ripple, which is usually smoothed with inductors and capacitors. Often a DC link consists of a set of two or three capacitors in series, while chokes L_{dc+} and L_{dc-} are optional elements. When the DC link contains two capacitors C_{dc+} and C_{dc-} the system has a midpoint O' . If voltages are smoothed well, the potential in this point approaches zero. In other words, the midpoint may be considered a natural neutral point of the drive (which, however, may float against, for example, the earth potential). It is shown in section 1.5 and subsection 4.3.4 that this midpoint may be used for the purposes of filtration.

A three-phase PWM inverter contains two bridges connected in parallel: a transistor bridge with transistors T_{A+} , T_{B+} , T_{C+} , T_{A-} , T_{B-} , T_{C-} and a diode bridge in reverse to the transistor one with the diodes D_{A+} , D_{B+} , D_{C+} , D_{A-} , D_{B-} , D_{C-} . The diode bridge protects inverter transistors from overvoltages when they are switched off by letting reactive currents run. The transistor switches are controlled according to the electric machine control algorithms. In practice, the voltage control is realized with the help of the pulse-width modulation method.

Along with the useful first (fundamental) harmonic of voltage, a PWM inverter generates a set of high harmonics, which are the reason of differential and common-mode noises (Mohan et al. 2003, Arrillaga and Watson 2003). The inverter and the motor have galvanic connections via cabling which, for simplicity, are shown in Figure 1.2 by the inductances L_{cab} in each phase. This way, the voltages u_A , u_B , u_C are transmitted to the motor terminals. These voltages cause motor shaft and load to move in accordance with assignment of the drive.

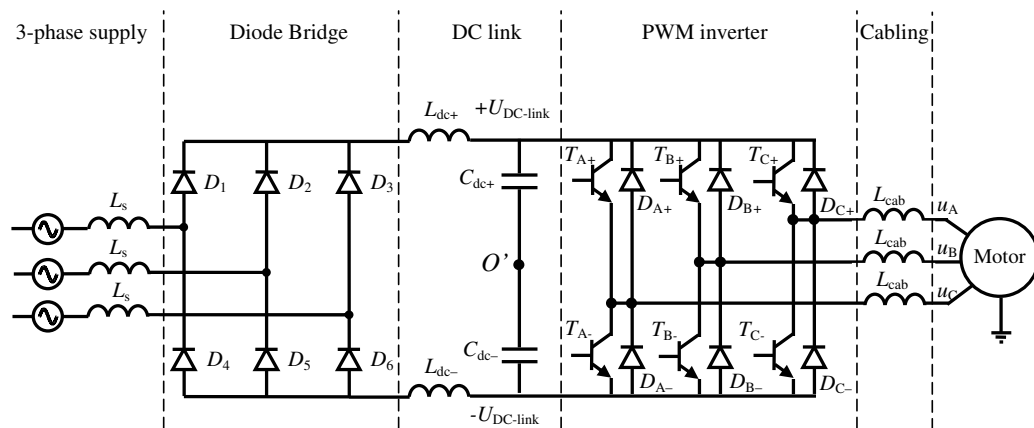


Figure 1.2. Main circuit of a voltage source electric drive. The diode bridge consists of positive and negative commutating groups. The DC link contains DC chokes and a large capacitor. The PWM inverter contains six IGBT transistors with diodes. Each of the inverter output voltages (u_A , u_B , u_C) can be connected either to the upper or lower potential of the DC link.

1.2.1 Diode bridge and DC link

The function of a diode bridge (also called a rectifier) is to rectify alternating voltage from a three-phase supply (Figure 1.3). Evidently, the voltage after the diode bridge has a considerable ripple that should be smoothed to obtain more constant values of voltage for the PWM power amplifier. That is why a DC link is required. However, the most important function of the capacitor is to provide a low-impedance voltage source for the inverter bridge. The DC link chokes are optional. The midpoint O' can be used in filtering of the PWM inverter output signals (such schemes are shown in subsection 1.5). Adequate smoothing is possible only at high values of DC link inductances and capacitances. Such values, however, are not always possible in practice. Therefore, the DC link only damps the ripple, and the potential at point O' is not equal to zero (theoretically, the earth potential) at every instant; it changes with a triple frequency of the main supply phase voltage (Figure 1.4) (Rendusara and Enjeti 1998). Because the standard main phase voltage frequency is equal to 50/60 Hz, the frequency of the DC link midpoint voltage is usually equal to 150/180 Hz.

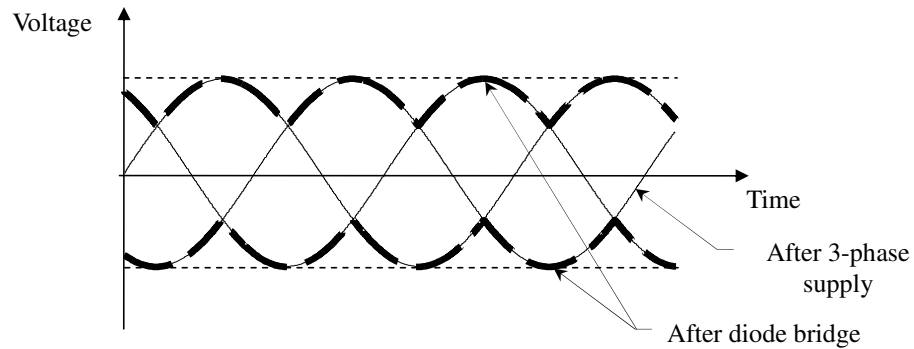


Figure 1.3. Input and output of the diode bridge signals.

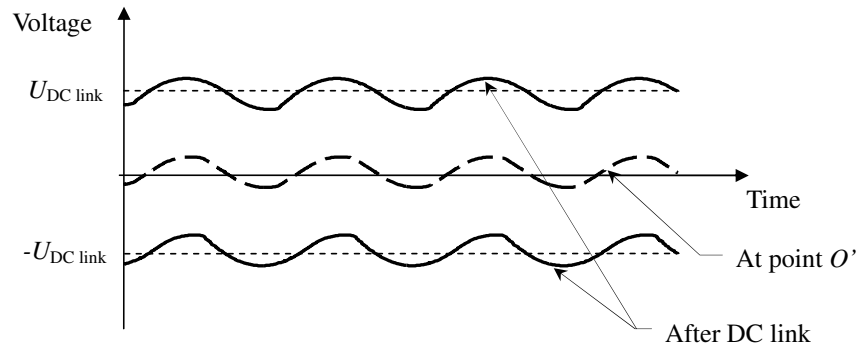


Figure 1.4. Output voltage of the DC link. As the output consists of positive and negative commutating group voltages, the midpoint of the DC voltage is not zero but varies on both sides of the earth potential.

1.2.2 PWM inverter

PWM technology provides a means to generate motor phase currents of the required shape permitting digital control usage in modern drives. The idea of PWM is based on the fact that the cabling system and the motor phases together can roughly be interpreted as an aperiodic link of the

first order. The voltage pulse injected into such a system produces a current that cannot change instantly. Thus, it is possible to change the current waveform by the width of the voltage pulse. This is convenient with the digital logic “either zero or one” used in microcontrollers. To generate the pulse of the required width, a microcontroller has only to compare the desired (modulating) signal with the reference signal and to set zero or one on its output pins (Kazmierkowski et al. 2002, Mohan et al. 2003). The reference signal often works with a constant frequency, called carrier frequency, and it is equal to the switching frequency. The signals of the microcontroller outputs switch the transistors of the inverter. The inverter is the unit that transforms the digital signals from the control unit to power voltages that are necessary for motor rotation. It is desirable to provide as high a switching frequency as possible (16 kHz as a typical maximum for modern IGBT transistors in hard switching) at the inverter design stage to prevent audible noise and additional motor losses caused by the nonsinusoidal motor input. In practice, the switching frequency of present-day industrial inverters varies in the range of 1–6 kHz.

A typical signal of a PWM inverter in all three phases is illustrated in Figure 1.5. Let us suppose that the phases are star coupled and connected to a PWM inverter without a cable (it is quite similar to the case when the effects of the cable are compensated). Figure 1.5 shows possible phase connections to the DC link during one PWM cycle. The connection can be changed seven times per one PWM period. In practice, the impedances Z of the phases a , b , c are almost equal so that we can assume that $Z_a = Z_b = Z_c = Z$.

Let us consider the possible schemes for phase connections to the DC link for each PWM period. It is evident from Figure 1.5 that the schemes for the time ranges 1 and 7, 2 and 6, 3 and 5 will be the same. Thus, we can find four equivalent schemes for the ranges 1–7 presented in Figure 1.6. Within 2, 6 and 3, 5 the system can be considered as a simple voltage divider, and the voltage at the motor winding star point N is $-u_{DC \text{ link}}/3$ and $+u_{DC \text{ link}}/3$, respectively. In the time ranges 1, 4, 7, all the phases are connected in parallel and the potential at point N can be assumed equal to the full potential of the connected DC link terminal. Therefore, the potential of the star point is nonzero and variable. In the literature, this potential in relation to earth is called common-mode voltage.

Now we can obtain the shape of the common-mode voltage for Figure 1.5, which is presented in Figure 1.7 (a).

Since usually the aim of the motor control is to obtain sine currents in the motor phases, the width of the pulses is not constant in each PWM period. Therefore, the common-mode voltage fundamental also changes with triple frequency of the modulated sinusoidal signal as it can be seen from Figure 1.7 (b), and its instantaneous value can be calculated by the well-known equation (Gambica, 2002):

$$u_{CM} = \frac{u_A + u_B + u_C}{3}. \quad (1.1)$$

Now we can state that PWM is characterized by a varying potential at the star point of the motor with an amplitude equal to half of the DC link voltage $U_{DC \text{ link}}$. Being a nonsinusoidal signal, this potential produces high-frequency harmonics. Thus, high-frequency currents between the neutral point and earth are possible. Therefore, stray capacitances inside the motor have to be taken into account.

A star connection is used here just as an example that helps us to determine the common-mode voltage. Practice shows that the described problem does not depend on the connection of phases or the number of motor phases.

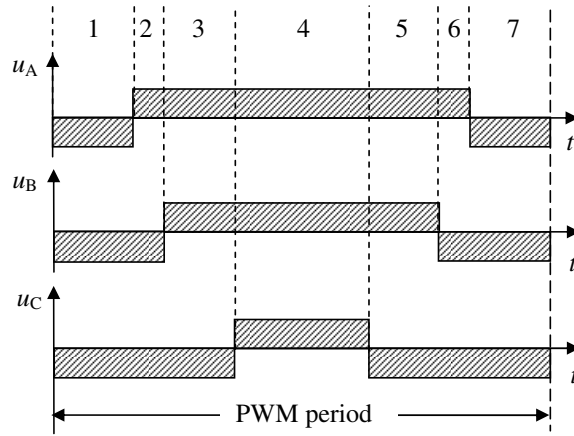


Figure 1.5. Typical PWM period in the inverter output of a voltage source.

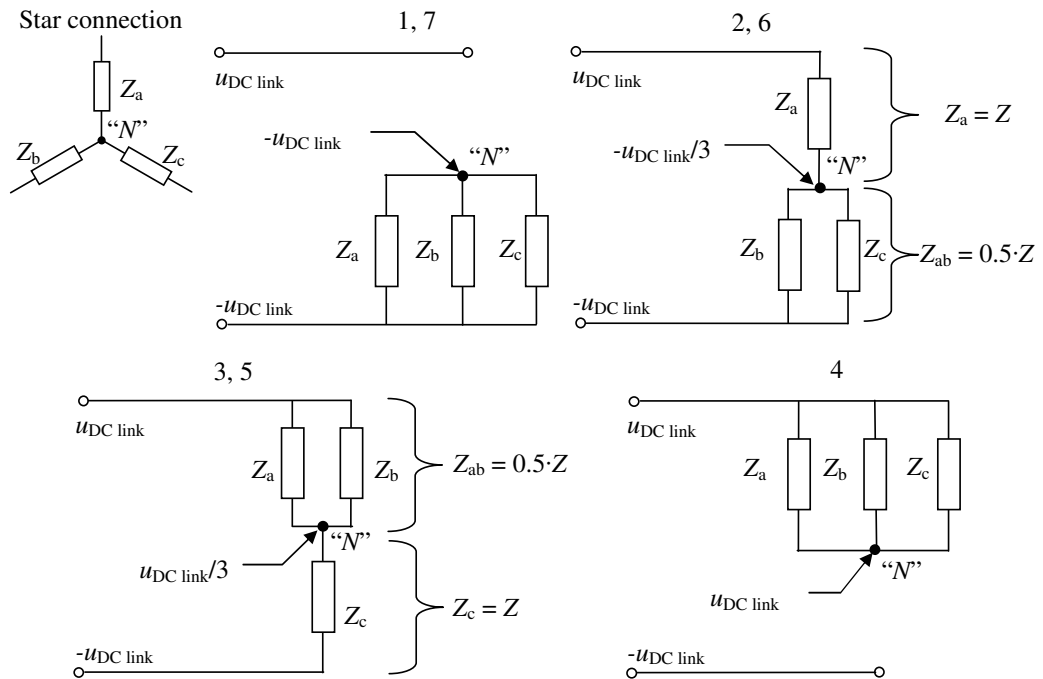


Figure 1.6. Equivalent electrical circuits of the phase connections to the DC link for the time ranges from 1 to 7 of the PWM period presented in Figure 1.5.

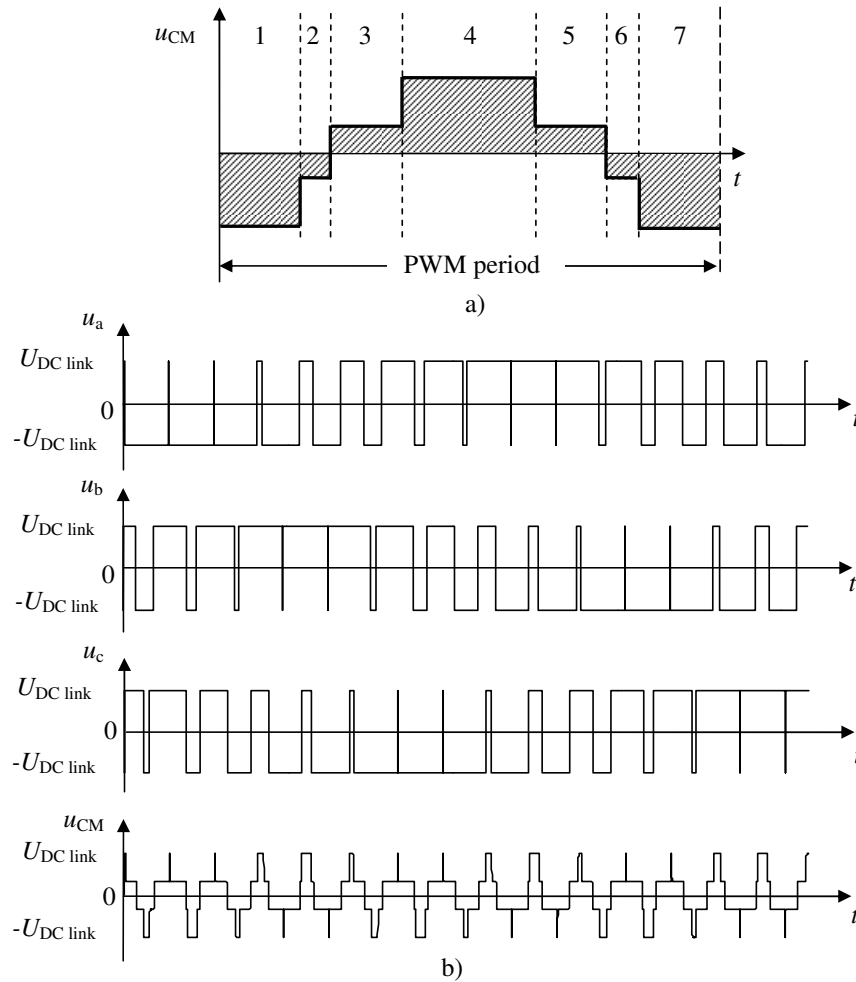


Figure 1.7. (a) Common-mode voltage for the PWM period presented in Figure 1.5. (b) PWM patterns in the phases and the common-mode voltage per one period of the modulated signal.

Along with common-mode voltages there are differential-mode signals that can be explained by reflections in the power cable. Such signals do not propagate into the motor but return to the converter protective earth via the cabling system.

1.2.3 Cable between the inverter and the motor

It is optimal for many high-power applications to use the electromechanical part of the drive remotely from the control part. It is evident that increasing the cabling system length is the only way to achieve an essential distance between the motor and the control unit.

At low frequencies, a cable can be described by an RL model. But since the rise time of pulses in modern inverters is typically nanoseconds, the spectrum of pulses injected to the cable has essential high-frequency components of large enough magnitude, and thus the capacitive couplings between the power cores of the cable and earth should also be taken into account. Therefore, a motor connection cable conductor can be represented as a set of RLC circuits (Figure 1.8) with an elementary component resistance R_{ci} , an inductance L_{ci} , a capacitance C_{ci} and a conductance G_{ci} (where i changes from 1 to n). Such a circuit is a representation of a transmission line (Gambica 2006). In multi-phase systems, mutual inductances between the lines are also under consideration (Arrillaga and Watson 2003, Weens et al. 2005).

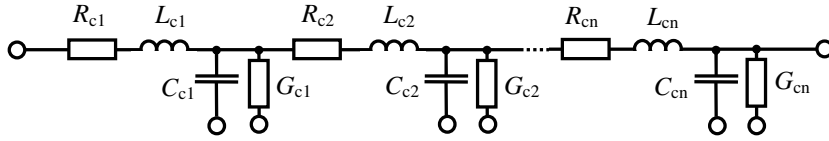


Figure 1.8. Motor cable representation with distributed parameters.

Let us analyse the theory of transmission lines in more detail by using simplified terminology and Figure 1.9 (a): a square-wave voltage u_{in} is generated by a voltage source (with a negligible internal impedance Z_{in}) connected to a load with an infinite impedance Z_{out} by two long cables. A special feature of the transmission lines theory is that it takes into account the time of signal propagation through the line and reflections of signals at winding terminals resulting from a characteristic impedance mismatch (von Jouanne and Enjeti 1997, Lee and Nam 2003). Roughly, the system presented in Figure 1.9 (a) can be characterized by a travelling current wave i_{tw} . When this wave travels to terminal T1 (red line), it charges the capacitors between the cables C_{ci} to the source voltage $u_{in}=u_{req}$. This travelling requires some propagation time t_p . Then, because of a load and cable impedance mismatch, the wave reflects from terminal T1 (green line). Now, the reversed current cancels the incident current and charges the capacitors C_{ci} to the value of $2u_{req}$. Because the impedance of the voltage source Z_{in} is equal to zero, the current wave continues to flow towards terminal T2 and now discharges the capacitors C_{ci} to the value of u_{req} (blue line). Then, the wave reflected from terminal T2 discharges the capacitors C_{ci} to a zero value (magenta line). This continues in cycles until some other required voltage source level is applied. Travelling of the current waves between terminals T1 and T2 takes a double propagation time $2t_p$ (because of a double distance).

In actual drives, resistances are always present, so that values $2u_{req}$ and the zero reachable in the LC circuit shown in Figure 1.9 (a) are only theoretical extremes. Therefore, attenuation of reflections and oscillations takes place in the resulting voltage. Nevertheless, according to Persson (1992), Kerkman et al. (1997), Finlayson (1998), Skibinski et al. (1998, 2006) and Lee and Nam (2003), reflections result in motor insulation damages.

Figure 1.9 (b) shows how reflection waves cause voltage overshoots at the motor end. In this case, we have chosen the pulse rise time t_r to be equal to the propagation time t_p . According to (Finlayson 1998), if $t_p < 0.5t_r$, the transmission line effects in a cable are negligible.

Similarly, current oscillations around 0 A at the converter terminals with maximum values close to $[i_{tw}; -i_{tw}]$ can be found.

Velocity v of pulse propagation in a cable can be defined by equation (Popović 2000):

$$v = \frac{1}{\sqrt{L_{ci} C_{ci}}} \quad (1.2)$$

Some aspects of cable selection are considered in (Mecker 1992, Bentley 1997, Basavaraja and Sarma 2008). According to Mecker and Bentley, there is a critical cable length at which the winding insulation may be damaged by overvoltages if special measures are not undertaken. The critical cable length is roughly evaluated by equation

$$l_{cr} = \frac{t_r}{2} v, \quad (1.3)$$

where t_r is the pulse rise time (in μs), which for IGBT inverters is in the range of 0.05–5 μs (Bentley 1997, Leggate et al. 1999, von Jouanne and Enjeti 1997).

Neglecting the elementary component resistance R_{ci} and the conductance G_{ci} of the cable, the characteristic (surge) impedance can be determined by equation (Popović 2000):

$$Z_c = \sqrt{\frac{L_{ci}}{C_{ci}}}. \quad (1.4)$$

A sum impedance of the main, the DC link and the inverter electronics represent the input impedance Z_{in} of the cable. In practice, this impedance is negligibly low compared with the surge impedance Z_c of the cable. The output impedance Z_{out} of the cable is the impedance of the motor. This impedance is considerably higher compared with the surge impedance (von Jouanne and Enjeti 1997, Schlegel et al. 1999).

If the voltage source generates voltages from $-u_{req}$ to $+u_{req}$, the value of the travelling current wave can be found with equation

$$i_{tw} = \frac{u_{req} - (-u_{req})}{Z_c} = \frac{2u_{req}}{Z_c} \quad (1.5)$$

The output impedance has essential value for some high-frequency harmonics of PWM signal so that they reflect from this impedance back to the inverter with a reflection coefficient

$$\Gamma = \frac{Z_{out} - Z_c}{Z_{out} + Z_c}. \quad (1.6)$$

Thus, reflections in the cable require special mitigation actions to protect the phase insulation of electrical machines.

As shown in Eq. (1.6), the value of the reflection coefficient in the case with motors ($Z_{out} \geq Z_{in}$) varies between $0 \leq \Gamma \leq 1$. A common magnitude for the reflection coefficient in high power drives is between 0.6 and 0.9 (von Jouanne and Enjeti 1997). The reflected voltage u_r can be expressed with the incoming voltage u_{in} and the reflection coefficient Γ

$$u_{refl} = \Gamma u_{in}. \quad (1.7)$$

The voltage affecting the motor terminals is

$$u_{\text{out.m}} = u_{\text{in}} + u_{\text{rfl}} = (1 + \Gamma)u_{\text{in}}. \quad (1.8)$$

The higher the reflection coefficient, the higher will also be the voltage stress at the motor terminals.

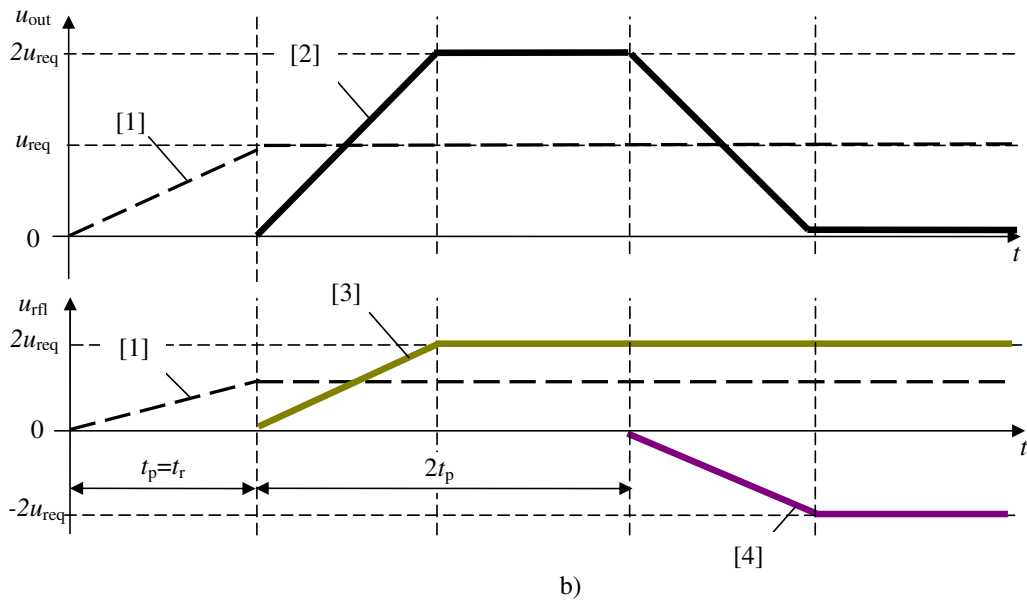
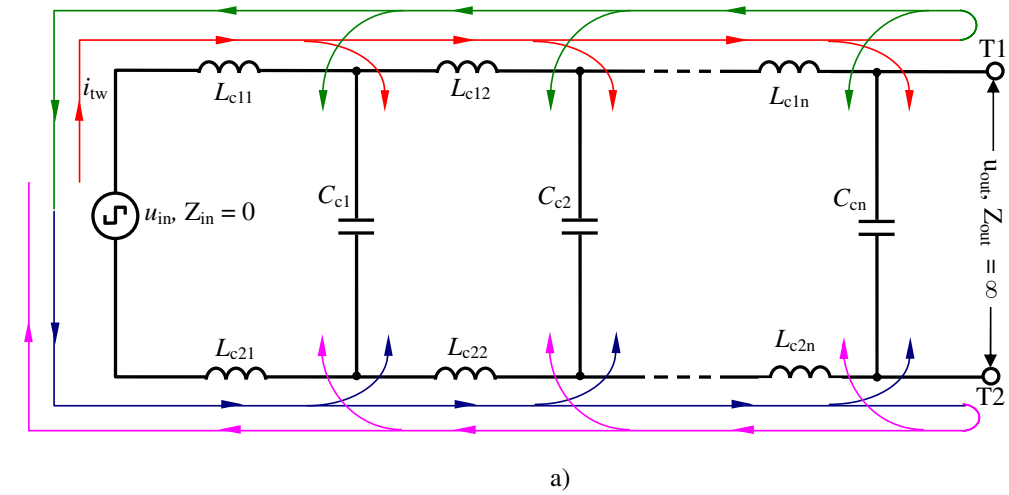


Figure 1.9. Reflections in a cable. (a) Simplified representation of a transmission line. (b) Voltage shape at the cable terminals changing as a result of reflections: [1] required voltage, [2] resultant voltage, [3] the first voltage reflection, [4] the second voltage reflection.

1.2.4 Motor

Motors are usually the highest-cost part of electrical drives. This may be explained mainly by complexity of manufacturing. Maintenance works are also quite expensive. Any electrical and mechanical failures are highly undesirable, because recovery may take a long time and be very costly.

Kaufold et al. (2000) show that the first turns of the motor winding are most vulnerable to overvoltages. Special IEC¹ and NEMA² standards define the overvoltage withstand capability of motors (Finlayson 1998, Gambica 2002).

However, problems caused by the reflections in the cable are not the only reason of failures in electrical motors. Attention should be paid to bearing currents, which are a consequence of the common-mode noise generated by the power converter.

There are probably bearing currents in almost all inverter-fed motors. Possible motor asymmetry may also, to some extent, cause bearing currents. According to Gambica (2002) and Muetze and Binder (2003), the shaft height can indicate the probability of the occurrence of a harmful bearing current. Three main groups of motors can be mentioned here:

1. Industrial motors with shaft heights below 280 mm are generally out of risk. With a proper drive electrical installation, the risk of failures should be low.
2. With shaft heights above 280 mm, a high probability of bearing failures is present if correct preventive actions are neglected. Along with a proper electrical installation, changing the PWM spectrum is needed. Additional di/dt filters are a recommended solution.
3. With shaft heights above 400 mm, the probability of bearing failures is very high. Changing the PWM spectrum may not be helpful, and thus, provision of a high-impedance path through bearings is required (an insulated or even ceramic bearing implementation).

The dependence of the bearing currents from the motor height can be explained by the fact that at high frequencies the motor can be represented as a set of stray capacitances (Figure 1.10) (Busse et al. 1995). The most important capacitances inside the motor are:

- Capacitance between the stator winding and the stator core, which is galvanically coupled with the frame C_{sf} .
- Capacitance between the stator winding and the rotor C_{sr} .
- Capacitance between the stator (galvanically coupled with the frame) and the rotor cores C_{rf} .

Figure 1.10 shows that at high frequencies there are at least three paths into which the current produced by the high harmonics of the PWM pulses can stray from the stator winding. Since the capacitance is a function of area between the isolated surfaces, the stray capacitances will generally increase with motor dimensions. This is the reason to classify the motors by their shaft heights.

¹ International Electrotechnical Commission

² National Electrical Manufacturers Association

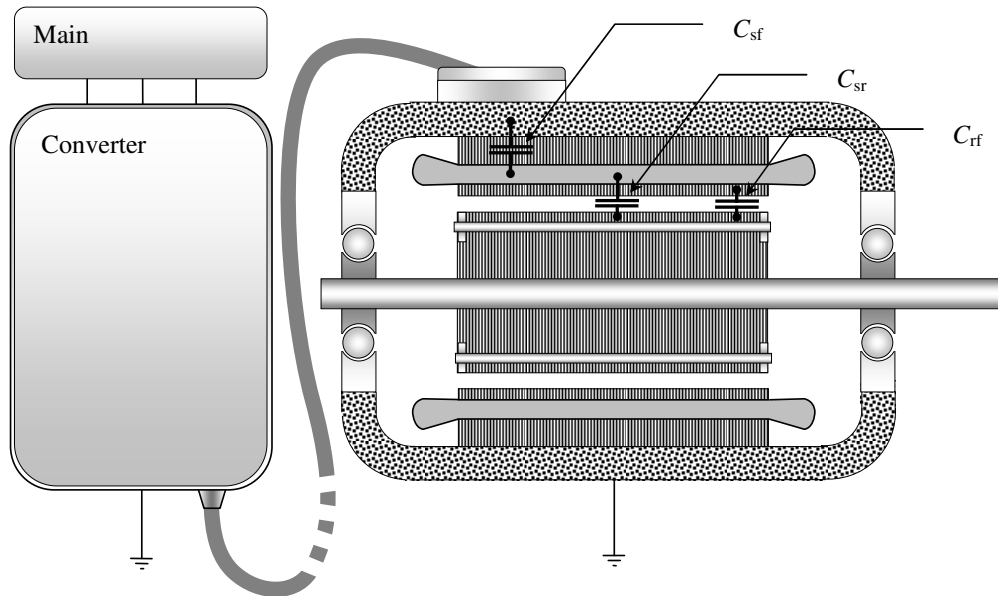


Figure 1.10. Inverter-supplied motor drive and the main motor stray capacitances illustrated as lumped capacitors: C_{sf} (stator–frame), C_{sr} (stator–rotor) and C_{rf} (rotor–frame).

Thus, there are a number of electrical circuits inside the motor that are closed through the bearings.

The impedance of the path stator winding–air-gap–rotor–bearing–frame–earth (or “common-mode impedance of the motor”) is high enough at low frequencies, where the first harmonics of the motor phase voltages usually occur. However, at the PWM switching frequency and higher frequencies, the impedance of this path is dramatically decreasing (Rendusara and Enjeti 1998, Ahola 2003).

All of the stray capacitances considered are present not only in AC motors but also in DC motors, and thus constitute a problem in DC motors also. In practice, the service life of a high-power AC motor can reach 30 years or more, and this should not be endangered by failures caused by bearing currents.

The function of bearings in an electrical machine is to support the rotor for free rotation. Typically, motors have two bearings (Hoppler and Errath 2007). In electrical machines, ball and roll bearings are the most common bearing types. A typical ball bearing (Figure 1.11) contains inner and outer races that both have grooves for balls. The balls are usually fixed with a ball cage retainer that separates the balls from each other. The free space inside the bearings is filled with grease that decreases the friction between the balls and the cages as well as between the balls and the races. In an electrical machine, the outer race is usually fixed to the stator while the inner race is fixed to the rotor. The roll bearing construction is similar to a ball bearing but rollers are used instead of balls. The service life of rolling-element bearings lubricated with modern greases in power applications varies from three to six years (Gambica 2002).

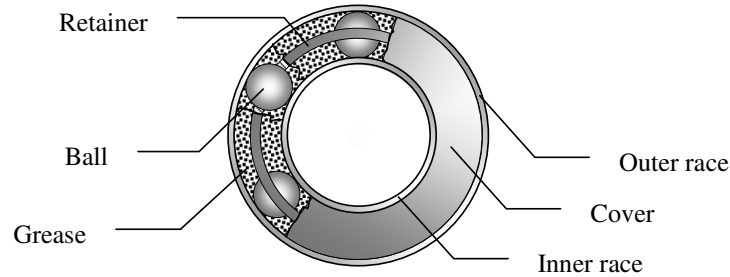


Figure 1.11. Ball bearing construction. The bearing consists of outer and inner races made of steel, ceramic or steel balls and a ball retainer that may be manufactured of brass, some composite material or plastic. A ball bearing must also contain some lubricant that provides a weak insulation between the races and the balls. With ceramic bearings, the bearing currents can be minimized. Ceramic balls are, however, mechanically weaker than steel balls. In some cases, the outer surface of the outer race is equipped with an insulation to prevent bearing currents from entering the bearing.

Electrically, a rolling-element bearing can be represented by the scheme in Figure 1.12 (Erdman et al. 1996), where R_{ob} and R_{ib} are the resistances of the outer and inner races, respectively, $R_{r,e}$ is the resistance of the retainer and the roller elements, $C_{o-r,e}$ and $C_{i-r,e}$ are the capacitances between the retainer with roller elements and the outer and inner races, respectively, C_{o-i} is the capacitance between the outer and the inner races and $Z_{r-g,r,e}$ is the nonlinear impedance that takes into account the nonlinearity of the electrical properties of the bearing at different motor speeds; this nonlinearity is caused by the lubrication grease that separates the rolling elements and the races as the motor speed increases (Palma et al. 2000).

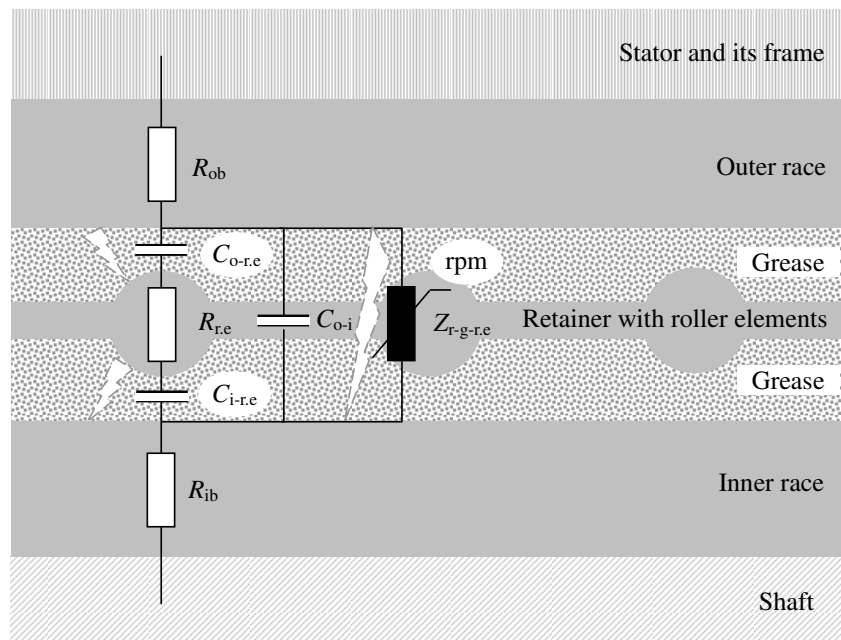


Figure 1.12. Equivalent electrical circuit of a rolling-element bearing.

Now it is easy to see the path through which the high-frequency currents between the shaft and the stator (stator frame) flow via bearings. The grease has a role of an electrical insulator in the capacitances $C_{o-r.e}$, $C_{i-r.e}$ and C_{o-i} . The grease can be classified as a liquid dielectric during motor rotation. It is a well-known fact that dielectrics of this kind are characterized by the ability to recover after spark breakdowns that can take place in bearings during motor rotation.

According to the statistics presented in (Hoppler and Errath 2007), electrical failures account for 9 % of all bearing failures. The most frequently occurring failures (22 %) are due to poor lubricant. This problem is also connected with the bearing currents, because they lead to accelerated grease ageing. Typical electromechanical failures originate from fluting (Figure 1.13(a)) and pitting of the races (Figure 1.13(b)).

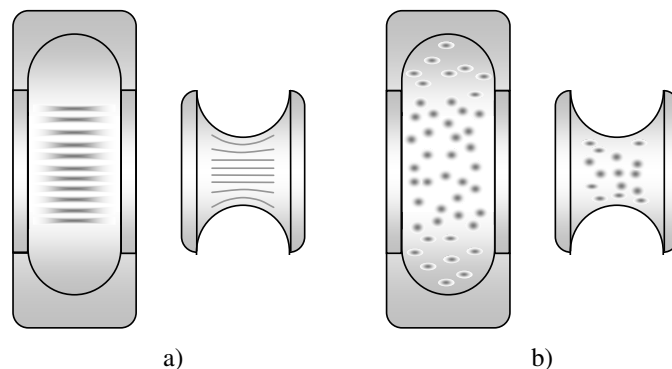


Figure 1.13. Bearing current may result in fluting (a) and pitting (b) of bearing races.

1.2.5 Power tool and sensors

Motor power tools (driven machinery) and sensors are mechanically and in many cases galvanically connected to the rotor shaft creating paths for a high-frequency current. The problem may occur, for instance, in mill drives. Theoretically, shaft currents can pass through the sensors on the shaft such as speed sensors, encoders, and the like. However, to our knowledge there are no reports available in the literature addressing these problems, and a detailed analysis of the issue is outside the scope of this study.

1.3 Bearing currents

According to Gambica (2002), Muetze and Binder (2003), Akagi and Tamura (2005), bearing currents can be roughly divided into the next different categories:

1. Capacitive discharge currents (or electrical discharge machining).
2. Circulating currents.
3. Shaft earthing currents.

Let us consider the main causes and effects of the bearing currents.

1.3.1 Electrical discharge machining

Electrical discharge is a phenomenon that is utilized in removing material in noncontact electrical machining processes (Shahruz 2003). This phenomenon is harmful for the bearings of electrical machines (Busse et al. 1995). Roughly, at high rotational speeds, a common-mode current charges the capacitance C_{rf} and the bearing capacitance C_{o-i} until a breakdown of the grease oil film inside the bearing takes place. As a result, an electrical discharge removing metal from the surfaces of the races and balls takes place. Figure 1.14 shows the simplified equivalent electrical circuit of a motor defined from Figures 1.10 and 1.12. The switch S describes the occurrence of an electrical contact between the balls and the races. The discharge current depends not only on the rise time of the common-mode voltage (Busse et al. 1995) but also on the moment when the switch S is closed (Mäki-Ontto 2006).

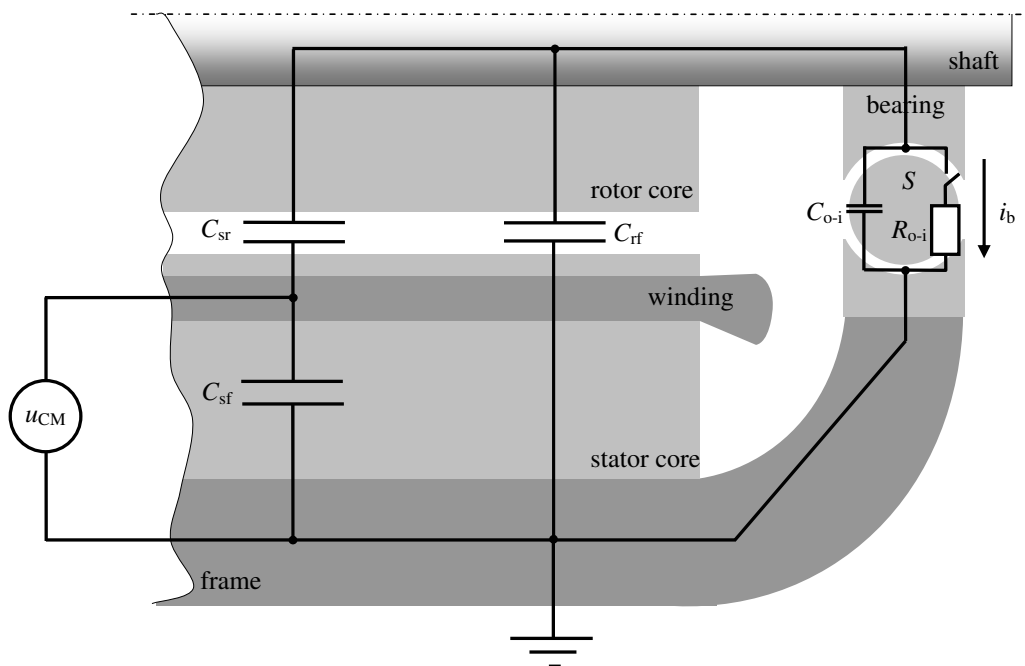


Figure 1.14. Simplified common-mode equivalent circuit of the motor.

Generally, $C_{sf} > C_{rf} > C_{sr}$ and the shaft potential is typically not sufficient to cause the oil film breakdown (Gambica 2002).

1.3.2 Circulating currents

Circulating current is created by stray currents flowing through the capacitances C_{sf} and C_{sr} (Figure 1.15). In fact, such capacitances are distributed along the winding and change the shape of the PWM pulses. Let us consider the motor with an unearthed frame as presented in Figure 1.15.

It is well known that a motor winding at low frequencies can be described by an RL circuit. At high frequencies, the model should include some kind of a generalized distributed impedance between the air-gap and earth Z_G , which includes the stray capacitances C_{sf} and C_{sr} as well as the bearing

capacitances. Thus, there are a variety of RLC links inside the motor, and energy predominantly tends to flow through the first coils of the winding (Mecker 1992, Kaufold et al. 2000).

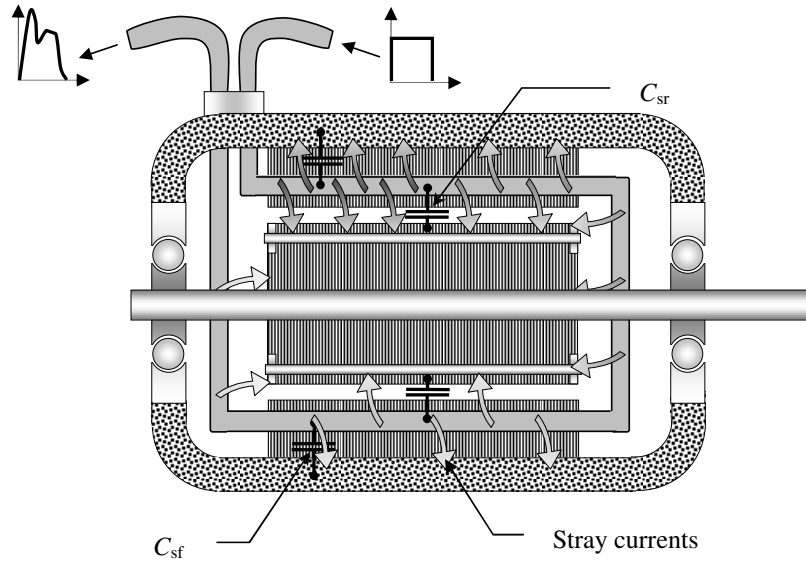


Figure 1.15. Winding current in one loop of one phase.

Propagating currents combine on the shaft forming the current I_{sh} circulating across the bearings and the frame, Figure 1.16. In the literature, such a current is referred to as ‘rotor circulating current’ (Ollila et al. 1997, Chen et al. 1998).

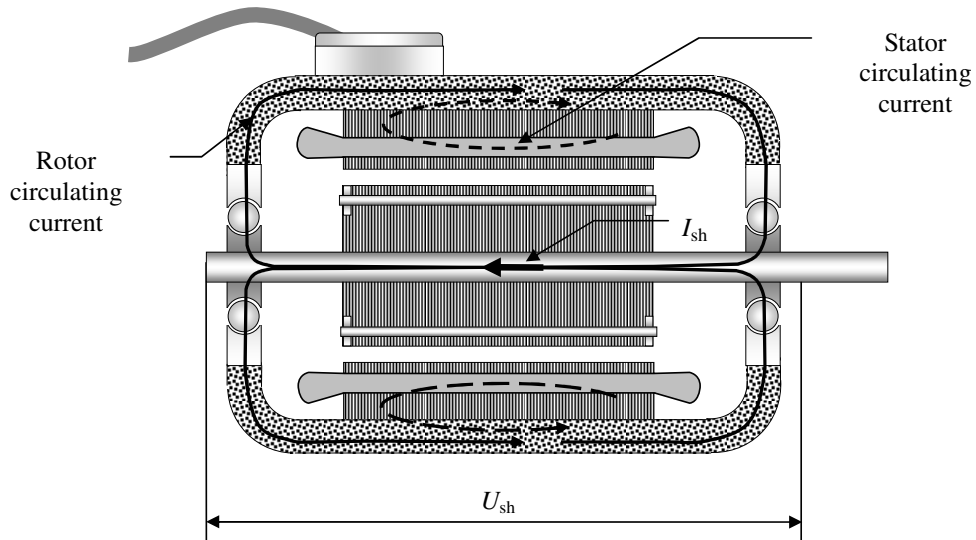


Figure 1.16. Circulating currents.

This current flows through the distributed capacitance C_{sr} . Since the shaft has an electrical impedance, the current I_{sh} creates a shaft voltage U_{sh} . According to Palma et al. (2000) shaft voltages exceeding 300 mV may be harmful to the bearings. Similarly, a stator circulating current is produced by the currents flowing through the stray capacitance C_{sf} . This current is not flowing through the bearings.

In practice, circulating currents may occur even if the motor is well earthed, because in most cases it is not possible to uniformly earth the frame. Circulating currents can be a reason for bearing failures in motors with shaft heights from 280 mm upwards. This can be explained by an increase in the capacitance C_{sr} resulting from a larger area between the stator and the rotor.

1.3.3 Shaft earthing current

Even if a system is properly earthed, harmful currents may pass through the bearings. There are a number of possible circuits inside the drive where current may flow to earth (Figure 1.17): the protective earth (PE) wire of the connection cable (current I_{PE}), earthed parts of the frame (currents I_{mfe1} and I_{mfe2}) and even the power tool earth (current I_{pte}).

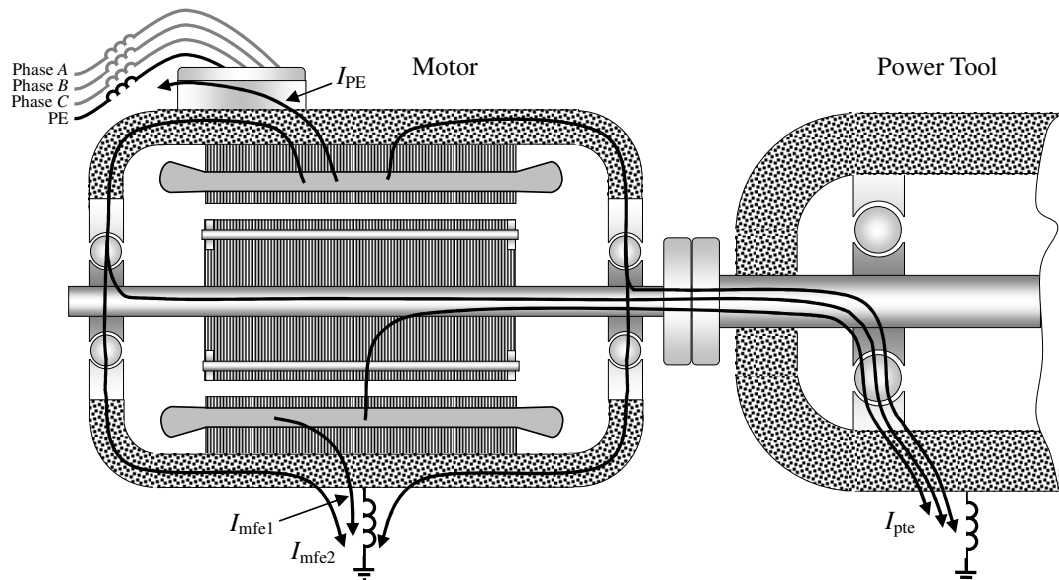


Figure 1.17. Earthing currents.

The relation between the shaft earthing currents depends on the impedances of the paths at different frequencies. It is emphasized that at the frequencies the inductances of the earthing wires may play an important role. If the path of the power tool earth has small enough impedance, the current may flow via the motor and the power tool bearings thereby causing failures.

If the circuit rotor–bearing–frame–earth impedance is relatively low, high-frequency currents may pass through motor bearings.

The currents I_{mfe1} and I_{PE} presented in Figure 1.17 are harmless to bearings, but they can cause EMC problems.

1.4 Mitigation of the adverse effects of pulse-width modulation

There is a number of ways to mitigate the adverse effects in drives with pulse-width modulation (Gambica 2002). These mitigation methods can be divided into three main branches:

1. Provision of appropriate earthing solutions inside the drive in order to bypass harmful currents from the bearings.
 - 1.1. Proper electrical installation of the drive.
 - 1.2. Installation of a shaft earthing system.
2. Provision of high-impedance paths inside the motor for bearing currents.
 - 2.1. Usage of insulated or ceramic bearings.
 - 2.2. Installation of a Faraday shield into the motor air gap.
3. Decreasing of the PWM voltage high-frequency harmonic amplitudes with special filters.

The first two items represent a set of solutions for bearing protection, whereas the third item may provide a universal solution which also includes motor winding protection.

A proper electrical installation allows making the impedance of earthing paths as small as possible. This permits to somehow decrease the stray currents inside of an electrical machine.

A shaft earthing system usually includes a contact by a carbon brush that is electrically connected between the shaft and the protective earth (Mei et al. 2003). The price of such an additional contact is low, but the fast wearing out of the carbon brush decreases the reliability of the drive and adds to the need for frequent maintenance.

Application of special kinds of bearings is recommended for large motors (Binder and Muetze 2007). Circulating currents and shaft earthing currents may be effectively prevented with insulated bearings, which have an insulating coat (50 μm –300 μm) on the outer race preformed from aluminium oxide. If an essential electrical discharge phenomenon is expected, expensive ceramic bearings can be used. However, bearings of this kind have poor mechanical withstanding to external forces.

A Faraday shield is an earthed conductive foil placed into the air-gap of an electrical machine. This shield helps to prevent rotor circulating currents, but it is quite expensive (it is difficult to avoid electrical contact when inserting the foil into a thin motor air-gap).

A universal solution for differential- and common-mode problems is to change the shape of the inverter output voltage waveform by electrical filters, such as output inductors, du/dt filters and sinusoidal filters (Finlayson 1998, Salomäki 2007). Output inductors are the most simple, reliable and inexpensive solution, but their influence on the shaft voltages is not significant enough (von Jouanne et al. 1998). The cut-off frequency of du/dt filters is higher than the inverter switching frequency, in other words, they deal with the shape of PWM pulses decreasing the voltage change rate. The cut-off frequency of sinusoidal filters is lower than the inverter switching frequency, that is, they filter the whole inverter waveform making the output signal almost sinusoidal.

Inverter waveform filters can also utilize resistors. However, a resistor is an undesirable element in a drive power circuit because of its heating caused by power losses within it. On the other hand,

filters based on reactive components only are characterized by oscillations of the output signal. Such oscillations are undesirable in many cases. A number of practical applications employ RLC filters to avoid large voltage overshoots. All existing solutions are based on separate components, which decrease the filter reliability.

Electrical filters can also be helpful in decreasing speed and torque pulsations and solving EMC problems. The main disadvantage of such filters is their high cost.

The analysis presented in this study shows that an output filter provides an effective way to decrease bearing currents. Therefore, developing a cost-efficient and reliable electrical filter to reduce the rise rates of PWM voltages and bearing currents in inverter-fed power drives is a highly relevant issue. This work concentrates on novel du/dt filters; the topic is discussed in greater detail in the following sections.

1.5 PWM inverter output filters

The existing solutions can include either only passive (von Jouanne and Enjeti 1997, Rendusara and Enjeti 1998, Hongfei et al. 2004, Akagi and Tamura 2005, Esmaeli 2006) or passive and active components (Hanigovszki et al. 2003, Esmaeli et al. 2006). Filters including only passive components have better reliability and cost, while filters containing active components have enhanced controllability. This study is related to filters based on passive components. However, the solution proposed later in this work may be used along with active components.

A conventional inverter output filter is presented in (von Jouanne and Enjeti 1997). The filter consists of inductances with series capacitances and resistances in parallel (without connection between points O and O') as shown in Figure 1.18, and it is very effective in suppressing voltage reflections in the cable (Lee and Nam 2003). A drawback of such a filter is that it cannot efficiently filter common-mode signals.

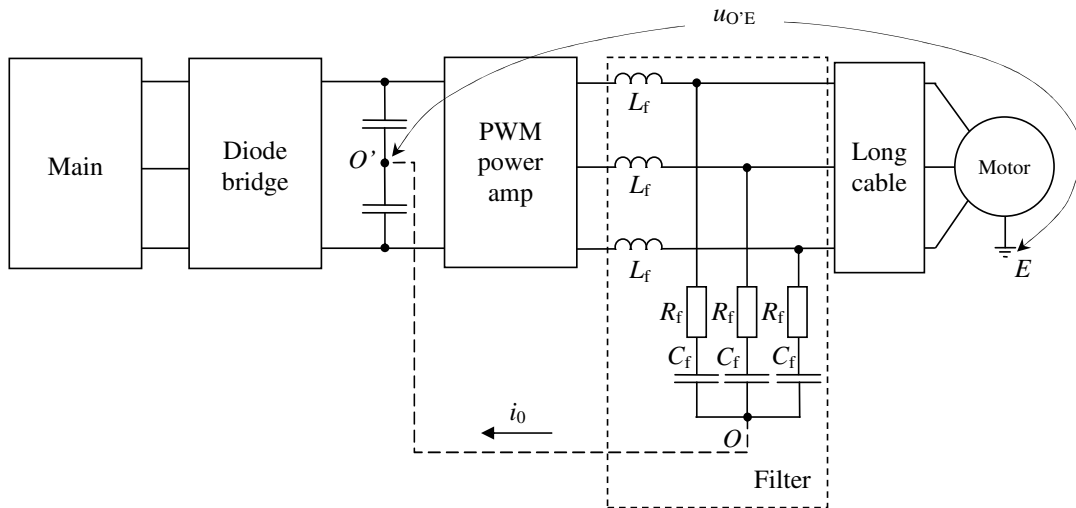


Figure 1.18. Common-mode filter schematics according to (Rendusara and Enjeti 1998).

Rendusara and Enjeti (1998) improved the construction by a common-mode connection between points O and O' . Supposing that the improved filter (that has the same electrical circuit as the conventional one) completely eliminates reflections in the cable, the common-mode voltages at the motor terminals can be described as:

$$u_{\text{CM}} = \frac{1}{3} \left(R_f i_0 + \frac{1}{C_f} \int i_0 dt \right) + u_{O'E}. \quad (1.9)$$

An analysis of this equation shows that the common-mode voltage at the motor terminals is a function of filter resistance R_f , inverse of the capacitance C_f and voltage $u_{O'E}$ between points O' and E in Figure 1.18. If $C_f \rightarrow \infty$ and $R_f \rightarrow 0$, then $u_{\text{CM}} \approx u_{O'E}$.

Now, the common-mode potential is close to the potential of the DC link midpoint with less amplitude and with much less frequency. The shape of the common-mode voltage becomes considerably smoother without harmful high-frequency harmonics (see subsection 1.2.1).

Hongfei et al. (2004) demonstrated the effectiveness of the configuration presented in Figure 1.18 for the case of sinusoidal filters.

The drawback of the method is that the midpoint may not be accessible and, moreover, some drive modifications do not have a midpoint at all. For example, if the capacitor is built of three capacitors in series, there is no midpoint available.

In such cases, other filter configurations may be considered, for example, a solution proposed by Palma et al. (2002) that helps to avoid direct connection to the midpoint with a RC bridge connected to points D and F as shown in Figure 1.19.

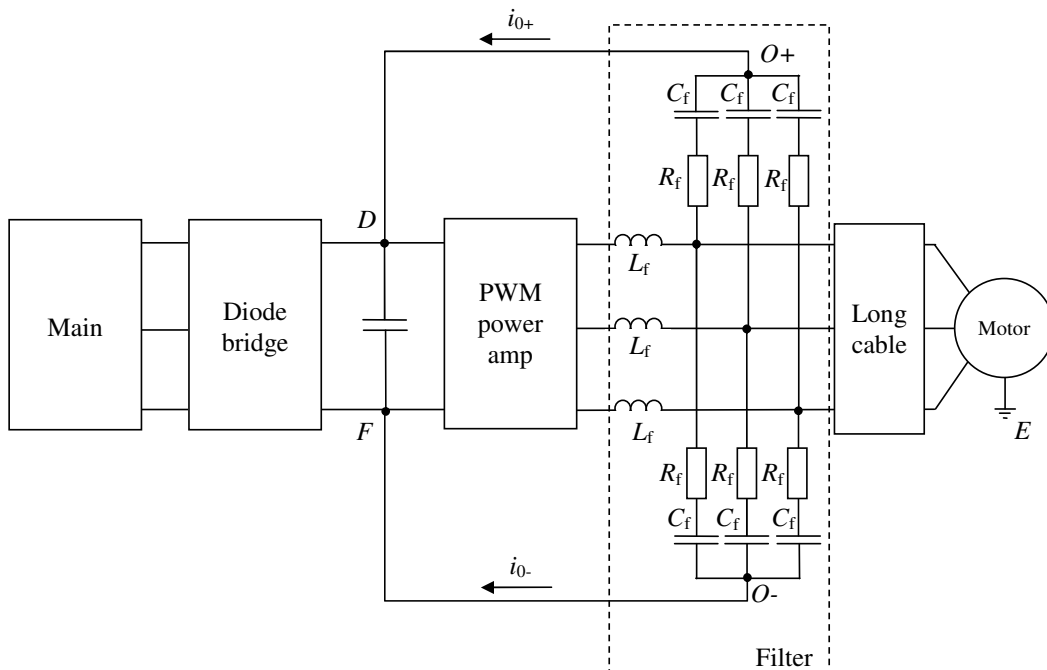


Figure 1.19. Common-mode filter according to (Palma et al. 2002).

For such a configuration, the common-mode voltage can be approximately expressed as:

$$u_{\text{CM}} = \frac{2}{3} \left(R_f i_0 + \frac{1}{C_f} \int i_0 dt \right) + u_{\text{OE}}. \quad (1.10)$$

Again, if $C_f = \infty$ and $R_f = 0$, then $u_{\text{CM}} \approx u_{\text{OE}}$ and the common-mode can theoretically be close to the potential at the DC link midpoint.

In (Hanigovski et al. 2004) an additional diode clamp is used as shown in Figure 1.20. If the instantaneous voltage at point O is not equal to $(U_D + U_F)/2$, the corresponding diode provides a path to the DC link.

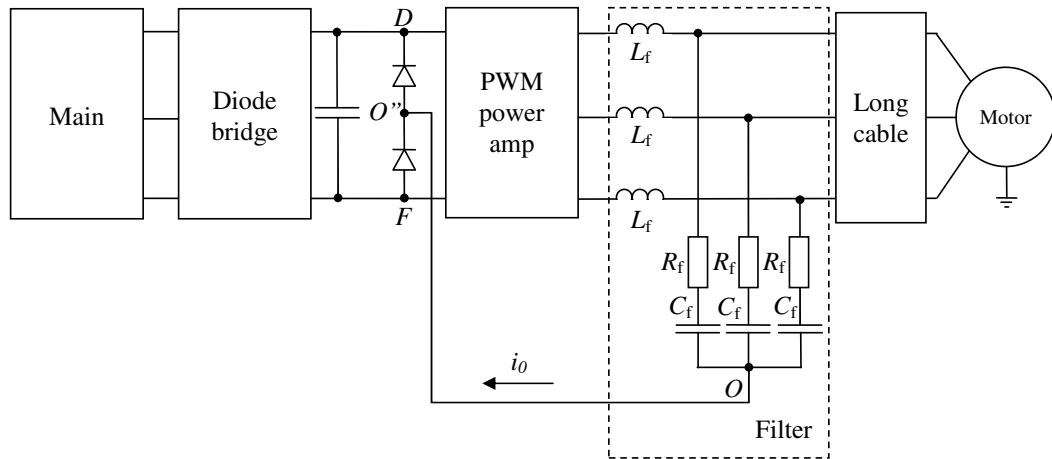


Figure 1.20. Common-mode filter according to (Hanigovski et al. 2004).

Cost-effective and compact alternatives to inverter output filters are motor terminal filters (von Jouanne and Enjeti 1997). The topology is presented in Figure 1.21, and it uses natural cable inductance instead of predesigned reactors. The solution is characterized by lower overshoots but higher voltage rise rates than a solution having a filter at the inverter output. However, Moreira et al. (2005) showed that a motor terminal filter cannot cancel reflections inside of the motor winding itself, while an inverter output filter decreases reflections in the motor winding to very low levels. As a result, spikes in the common-mode current are much lower when an inverter output filter is implemented. If a filter at motor terminals is used, a common-mode conductor between the filter star point and the DC link midpoint becomes quite useless because of the distance between the motor and the DC link. Now, the long conductor with an essential inductance L_{cm1} has a large impedance preventing the high-frequency noise currents from flowing.

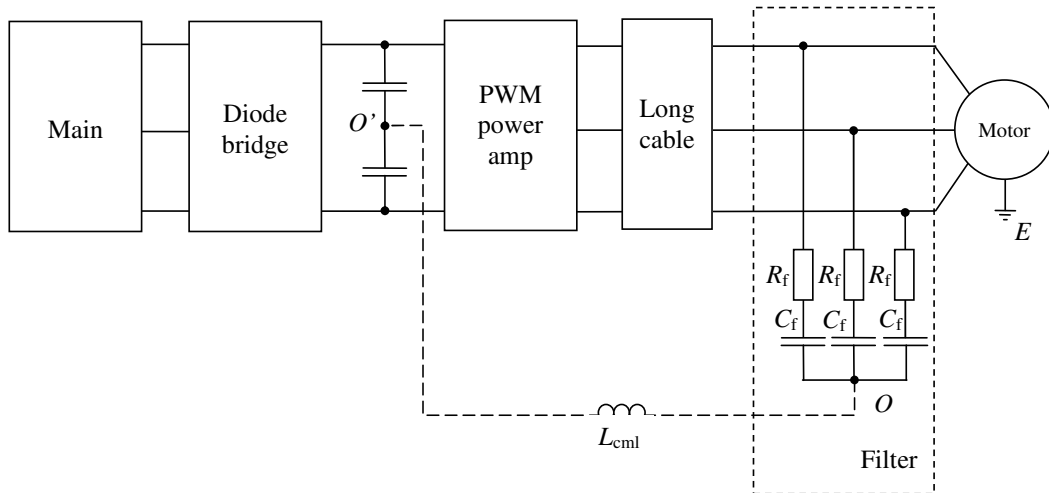


Figure 1.21. Topology of the filter at motor terminals (von Jouanne and Enjeti 1997) utilizes the cable natural inductance but has a long, high-impedance return path to the DC link midpoint.

Some solutions contain more than one filter (Akagi and Tamura 2005, Esmaeli 2006, Esmaeli et al. 2006). For example, in (Esmaeli et al. 2006), two filters work together in order to achieve acceptable EMC characteristics as well as to decrease differential- and common-mode noise.

One property is common for most filter designs: they are based on separate components distributed throughout the system. This fact complicates the arrangement of the cabinet and decreases the reliability of the system. In addition, the inductances of connection wires may prevent filtration at high frequencies. This gives a motivation to search for new kinds of designs.

1.6 Hybrid LC filter

There are three ways to wind a choke. The lowest-cost alternative, a round wire, is characterized by an essentially high AC resistance at relatively low frequencies, and, therefore, by significant losses. To decrease the losses, the conductor cross-sectional area can be divided into small isolated subconductors. Compared with a round wire, such a solution, called 'Litz wire', has a lower AC resistance. However, its DC resistance is higher and depends on the fill factor.

With a foil-wound choke, low DC and AC resistances are achieved thanks to the uniform, thin and large conductor cross-section. In order to avoid short-circuits, essential surfaces between coil turns have to be separated by insulation. This leads to a relatively high capacitance between the turns forming the self-capacitance of the choke, also called 'intra capacitance' (Bossche and Valchev 2005), and letting the high-frequency components travel through the coil without damping. On the other hand, insulation layers weaken the heat transfer.

Based on the previous description, a new hybrid LC filter (HLCF) presented in Figure 1.22 may be proposed (Pyrhönen et al. 2009). One phase of the hybrid LC filter comprises two or more foil layers isolated from each other and coiled on an air core. In this study, the first layer is called a main foil while the second one is an auxiliary foil. The main foil can be placed between the inverter and the cable or the cable and the motor. The auxiliary foils are just combined in star. In such an arrangement, there is a significant capacitance between the main and auxiliary foils. As the

auxiliary foil is coiled together with the main foil on a tube, the auxiliary foil will be located between every main foil turn. This way, the auxiliary foil minimizes the intra capacitance of the main foil. Placed to the PWM inverter output or cable output, the hybrid LC filter provides a low-impedance path for high-frequency harmonics of PWM voltages. Thus, differential- and common-mode noises may be suppressed to a required degree. The hybrid LC filter auxiliary foils star point can be connected to the DC link as it is shown in Figures 1.18–1.20 so that common-mode energy is effectively supplied back to the frequency converter. To further simplify the considerations, let us call the effective inductance of the main foil a main inductance and the effective capacitance between the foils a main capacitance. The main capacitance can be increased with an additional auxiliary foil.

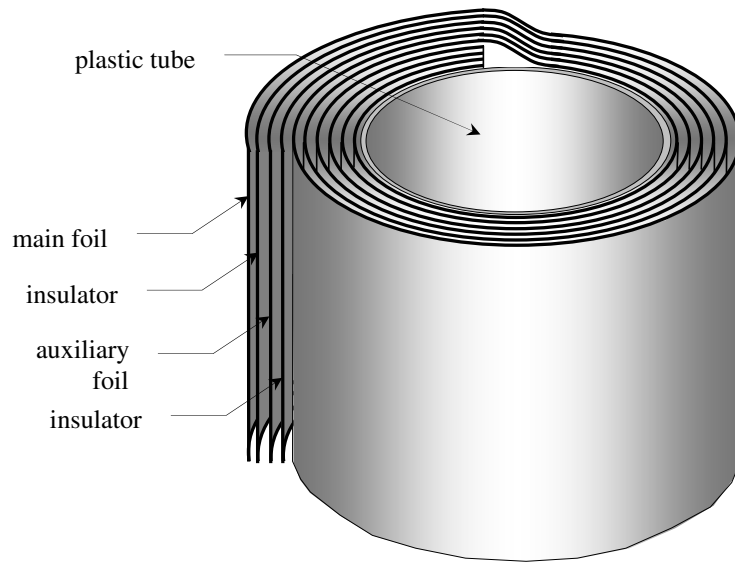


Figure 1.22. Principal configuration of a single phase of the novel air-core hybrid LC filter.

A hybrid LC filter is characterized by a better reliability compared with separate-component approaches. The price is expected to be low.

The main disadvantage of the HLCF is the difficulty of the design and modelling. With that, high voltage stresses between main and auxiliary foils can be a reason of partial discharges in the insulation layers. In addition, to the author's knowledge, there is no practical data (except the current study) proving that auxiliary foil can be useful in pulse rise rates lowering. Hence, questions of material selection, calculation, simulation, manufacturing and practical implementation of the hybrid LC filter require careful analysis.

1.7 Objectives and scope of the thesis

The main objective of this study is to propose a general concept for hybrid LC filters for design purposes but also to promote comprehensive understanding of the topic. The results of the study have to be feasible in the development of power electronic drives.

To this end, the following tasks should be considered:

- Investigation of a set of drives in which PWM filtering is needed.
- Obtaining a calculation technique for a hybrid LC filter.
- Development of a design method for a hybrid LC filter.
- Modelling of a hybrid LC filter.
- Investigations of a hybrid LC filter electrical properties in frequency and time domains.
- Investigations of a hybrid LC filter influence on the performance of the real power drive.

The thesis is divided into five chapters. The theoretical background, the topicality and the objectives of the work are introduced in Chapter 1. In Chapter 2, questions of material selection, calculation and design of a hybrid LC filter are considered. In Chapter 3, the properties of prototypes of a hybrid LC filter in the frequency domains are considered, electrical representation of a hybrid LC filter is proposed, and simulations in the frequency and time domains are carried out. In Chapter 4, experimental results are provided in the frequency and time domains in AC drives. In conclusions, the main results of the work are discussed and suggestions for future work are made. Appendix A contains comparison tables of calculated and measured data for three different prototypes as well as provides a design example of the hybrid LC filter of the test setup discussed in Chapter 4 in accordance with the design method developed in Chapter 2 and applying the model proposed in Chapter 3.

2 Hybrid LC filter design

2.1 Required range of common-mode attenuation

Leakage impedances degrade attenuation properties of filters at high frequencies. These parameters should be taken into account in filter design in order to provide good performance in the required frequency range. Ringing due to cable distributed parameters is known to occur in the range of 50 kHz–2 MHz (Finlayson 1998). Thus, the focus of this section is on the analysis of common-mode signals of a hybrid LC filter (HLCF) by simulations. It should be pointed out that the required frequency attenuation range depends, for instance, on the motor and inverter properties and the PWM frequency. Therefore, simulations provided in this section can be carried out for any drive where bearing currents are expected. It is also quite difficult to predict what part of common-mode current will flow through the bearings. Nevertheless, common-mode current suppression by filtering is advantageous for EMC reasons. Consequently, the aim of this section is to find a method for common-mode current evaluation in order to achieve an appropriate hybrid LC filter for an actual experimental motor drive.

Nowadays, various technical software applications provide a number of tools for scientific purposes. For our investigations, MATLAB Simulink is a very convenient simulation environment. An alternative is to use the free program Scilab with the Scicos tool, which is analogous to Simulink. Scilab may be even more convenient than MATLAB, as the program provides expressions representation in the s -domain. However, current releases of Scilab are quite unstable. Simulations may also be performed, for example, with the help of free circuit simulator LTspice IV or other suitable software.

Let us suppose that the simulated system has ideal switching transistors, and it is equipped with a filter that suppresses all the reflections caused by the cable length. Hence, we can neglect the cable.

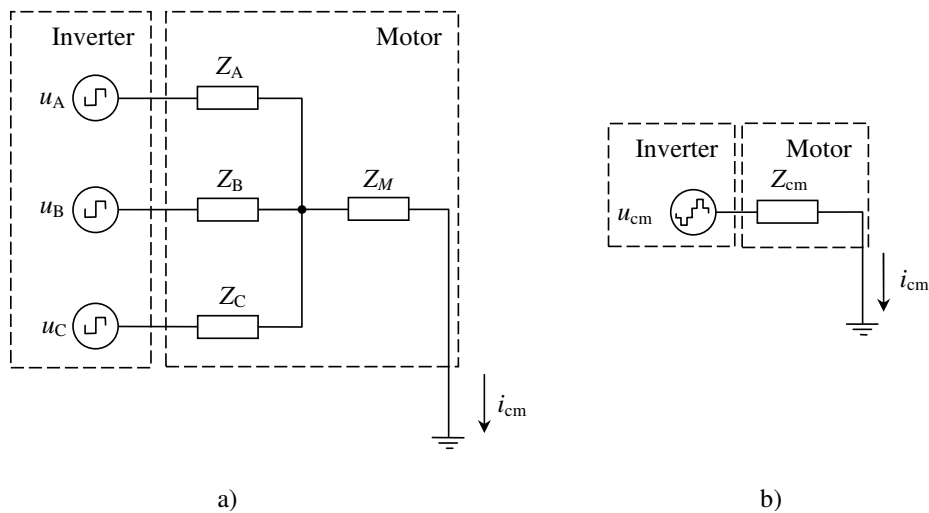


Figure 2.1. Common-mode circuit (a) and its equivalent circuit after the transformation in accordance with Thévenin's theorem (b).

A common-mode circuit can be represented by an electrical circuit as shown in Figure 2.1 (a) where u_A , u_B , u_C and Z_A , Z_B , Z_C are the sources of PWM signals and the impedances of the phases A, B, C,

respectively; Z_M is an impedance that includes all the impedances of the electric motor except Z_A , Z_B and Z_C . According to Thévenin's theorem, such a circuit can be replaced by an equivalent scheme of Figure 2.1 (b) (Horowitz and Winfield 1989), where u_{cm} is an equivalent voltage source and Z_{cm} is the common-mode impedance discussed in subsection 1.2.4 and, for instance, by Rendusara and Enjeti (1998).

Ahola (2003) gives the following equation for motor common-mode impedance at high frequencies in the Laplace domain:

$$Z_{cm}(s) = \frac{s^2 C_{hf} L_{hf} + s C_{hf} R_{hf} + 1}{s C_{hf}}, \quad (2.1)$$

where C_{hf} , L_{hf} and R_{hf} are the high-frequency capacitance, the inductance and the resistance of the motor, respectively.

Thus, it is possible to construct a model in Simulink with the help of the structure presented in Figure 2.2.

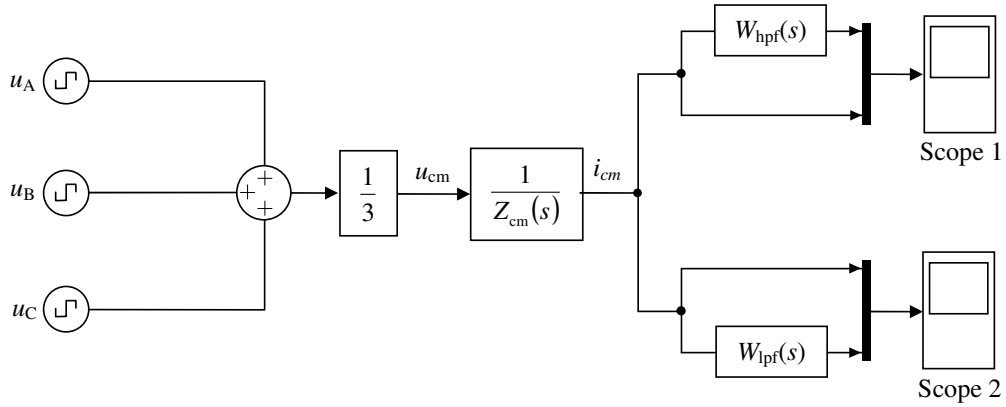


Figure 2.2. Structure of the model for definition of the common-mode attenuation range.

The model functions according to the following principle: first, it compares the sine values and the triangle reference signal and then transforms the obtained unipolar signals into complimentary ones in order to simulate three-phase PWM pulses at the inverter outputs, shown by the voltage sources u_A , u_B , u_C . Next, the model calculates the common-mode voltage u_{cm} by (1.1) and the current i_{cm} using Eq. (2.1).

At first thought, the most rational way to determine the attenuation range would seem to be to obtain the spectrum of the common-mode current. However, more obvious results may be obtained in time domain by placing high- and low-pass filters into the model and to find the attenuation range by changing the filter cut-off frequencies.

The transfer function of a high-pass filter is:

$$W_{hpf}(s) = \frac{K_{hpf} s^n}{(T_{hpf} s + 1)^n} \quad (2.2)$$

where T_{hpf} is the high-pass filter time constant, $K_{\text{hpf}} = \left(\frac{1}{T_{\text{hpf}}}\right)^{-n}$ is the high-pass filter gain and n is the filter order.

The transfer function of a low-pass filter is:

$$W_{\text{lpf}}(s) = \frac{1}{(T_{\text{lpf}}s + 1)^n}, \quad (2.3)$$

where T_{lpf} is the low-pass filter time constant.

Bode plots for the transfer functions in Eqs. (2.2) and (2.3) are given in Figure 2.3. When all signal harmonics are in the linear zones of the filters, the shapes and phases of the filtered and unfiltered common-mode currents are the same, in other words, the filters do not affect the current. By changing T_{lpf} and T_{hpf} , it is possible to find the corner frequency at which the influence of the filters is negligibly low. It is evident from Figure 2.3 that the linear zone is generally determined by the phase curves of the Bode plots, and for the high-pass filter the linear zone is $[f_{\text{hlz}}; \infty]$, while for the low-pass filter it is $[0; f_{\text{llz}}]$. Thus, the attenuation range can be interpreted now as the range of frequencies between f_{hlz} and f_{llz} .

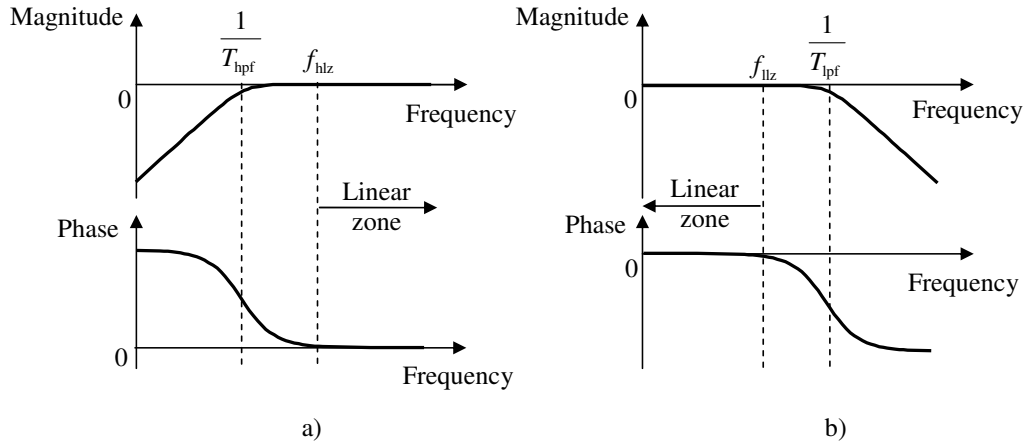


Figure 2.3. Bode diagrams of (a) the high-pass and (b) the low-pass filters.

The presented calculation method takes into account both the electrical discharge machining and the circulating current phenomena, which were described in subsections 1.3.1 and 1.3.2, respectively. If the common-mode impedance of the load is known, it may also be placed into the model to take into account the shaft earthing currents considered in subsection 1.3.3.

Using the proposed method for the test motor which is described in detail in Chapter 4 ($L_{\text{hf}} = 145$ nH, $C_{\text{hf}} = 4.9$ nF and $R_{\text{hf}} = 2$ (Ahola 2003)) the attenuation range of the common mode currents is between 250 kHz and 6 MHz. This attenuation range is sufficient to minimize the problems caused by the common-mode currents.

2.2 Selection of materials

The LC filter studied here consists of the main and auxiliary foils, insulation layers and an external frame as described in section 1.6. Furthermore, it has connection outputs, a bandage layer and an outer cover needed to prevent magnetic flux components generated in the inductors from penetrating into other parts of the equipment. Let us now consider the questions of choosing suitable materials for the filter.

Table 2.1 shows the main features of some commonly used metals (Lide 2003). The main and auxiliary foils of the hybrid LC filter should have good electrical and thermal conductivities and a low mass, and they should also be inexpensive. According to Table 2.1, copper and aluminium foils can be used. Silver and gold foils have appropriate parameters, but their use in the HLCF is economically unjustified for most of the cases. Iron cannot be used as a foil because of its ferromagnetism.

Table 2.1. Properties of some metals

Metal (pure)	Resistivity constant at 23 °C, $\mu\Omega\cdot\text{m}$	Density at 25 °C, kg/m^3	Thermal conductivity at 27 °C, $\text{W}/(\text{m}\cdot^\circ\text{C})$
Aluminium	0.024	2700	237
Copper	0.015	8960	401
Gold	0.021	19300	317
Iron	0.086	7870	80
Silver	0.015	10500	429

Aluminium foil can be quite useful in HLCF production. Its resistivity, density, thermal conductivity and price are relatively low. Resistivity of aluminium is not seriously affected by moderate amounts of impurities, and the foil is, hence, inexpensive. For instance iron mentioned in Table 2.1 is very sensitive to additives, and the resistivity of moderately alloyed steel is in the range of 0.2–0.3 $\mu\Omega\cdot\text{m}$. In the past, the problem in using aluminium foil was the difficulty of achieving reliable contacts. The problem has now been solved, and aluminium is largely used in the production of different coils. If the foil has to be thin, handling of the aluminium foil in the production may be difficult. An alternative is to increase the thickness of the foils, which, however, would result in increasing dimensions and cost.

An alternative to aluminium is copper foil; the material is much more firm than aluminium. The resistivity of copper is considerably lower than the resistivity of aluminium, its density and thermal conductivity are higher, and the price is moderate.

Hybrid LC filters based on aluminium foils are recommended as low-cost solutions (except in cases where the foils are very thin). A compromise between a low price and compactness is to produce the main foil from copper and the auxiliary foil from aluminium.

To provide a required capacitance between the main and auxiliary foils, the insulation material used in between should have a high relative permittivity and a very good dielectric strength in a wide range of temperatures and frequencies, where the filter should provide attenuation at required

humidities and vibrations. Some applications may require some specific properties, for example, ability to withstand different kinds of micro-organisms in a tropical environment.

Insulation materials can be gaseous (air, oxygen), liquid (dielectric oil) or solid (organic fibres such as wood cellulose; inorganic such as mica, fibre glass and mineral wool; synthetic materials such as films and gums; porcelain enamels, lacquers etc.). Lacquers and special compounds can be used as impregnants to improve the thermal, mechanical and electrical properties of an insulation.

The use of gaseous and liquid dielectrics in HLCFs may be problematic, because the filter should be compact, but direct electrical contacts between the main and auxiliary foils are not allowed. At the same time, liquid dielectrics can make the system more massive, which is also undesirable. Nevertheless, air should be taken into account as an additional insulation layer because in most cases, ideally tight combination of foils and insulations is not possible (Popović 2000). A good solution could be to impregnate the filter columns with dielectric oil, which, however, may increase the price of the final product.

The temperature inside the choke should remain sufficiently low. The lifetimes of insulation materials decrease dramatically when the temperature rises (Boldea et al. 2002). Therefore, the thermal classes 105, 130, 155 and 180 can be recommended. Other factors affecting the aging of an insulation are mechanical vibrations and certain chemical changes.

Table 2.2 presents the main properties of some popular insulation materials: Calmica, Mylar and Nomex (Isovolta 2004, Isovolta 2007, Du Pont 2000A, Du Pont 2000B, Du Pont 2003, Pyrhönen et al. 2008).

Table 2.2. Properties of some insulation materials.

Insulation	Relative permittivity at 25°C		Relative permittivity at max. allowable temperature	Allowable temperatures, °C	Dielectric strength, kV/mm
	60 Hz	3.3			
Mylar (polyester)	60 Hz	3.3	3.7	25 – 180	≥ 85
	1 GHz	2.8			
Calmica (mica)	4.5		5.3	23 – 150	≥ 50
Nomex Type 418 (aramid + mica)	2.9 – 4.1 ³		3.4 – 4.8 ⁴	25 – 250	≥ 59

Calmica is mica paper produced from sheet silicate minerals. Such materials are characterized by excellent insulation properties as well as high temperature resistance.

Nomex, similarly as Kevlar and Teijin Aramid (previously known as Twaron), belongs to the group of aramid fibres (Shwartz, 2002). Such insulations are stable, tough and stiff even above 150 °C. The advantages of the materials considered are explained in Table 2.2. Nomex Type 418 has improved stability and better overall properties at high temperatures, because it contains 50 % of inorganic mica.

³ Depends on thickness

⁴ Depends on thickness

Mylar is a polyester film. Such materials typically have a high dielectric strength, and they combine good electrical and thermal properties.

Table 2.2 shows that Calmica has the best relative permittivity, Mylar has a better dielectric strength, while Nomex has the widest range of allowable temperatures.

A hybrid LC filter can be built by using any of the materials presented. However, if high temperatures inside the filter are expected, aramid foils are a recommended solution. In high-voltage applications, polyester films can be used. In applications where the physical dimensions are the most important factor, mica papers can be an appropriate choice. Mica may also be needed in some cases because of its good resistance to partial discharges.

The column frame can be produced from an inexpensive and firm insulation material, for instance glass fibre tube. The cover should be manufactured of perforated steel to keep the stray flux level outside the choke low.

2.3 Calculation technique

In this work, the calculations of the HLCF aim to define the geometry of the LC filter with a desired resonance frequency. Because all the HLCF columns are identical and the mutual couplings between them can be neglected in the design, a single column is considered. The calculation technique of a two-foil air-core HLCF is provided as a basis of calculations of the other possible configurations.

For the majority of real cases, as small dimensions as possible are desired. The dimensions of a hybrid LC filter depend on the requirements set for the actual power electronic drive, and they can be described by an aspect ratio h_D of the LC filter's axial cross-section:

$$h_D = \frac{h}{D_{\text{out}}}, \quad (2.4)$$

where h is the LC filter height and D_{out} is its outer diameter.

Our calculations are based on standards that permit a double overshoot. In other cases, we can use, for instance, the papers of von Jouanne and Enjeti (1997) as well as Lee and Nam (2003), which discuss a design with a resistor damping the resonance. On the other hand, the resistor causes additional losses and heat, which are undesirable for many applications.

The resonance frequency of a du/dt filter is set higher than the PWM switching frequency. The desired pulse rise-time t_r can be defined from the standards and be used to determine the filter resonance frequency

$$f_r \approx \frac{1}{4t_r}, \quad (2.5)$$

The aspect ratio of the LC filter's axial cross-section h_D and the filter resonance frequency f_r are the initial data for the hybrid LC filter calculations. The other initial data are the thicknesses of the main foil d_{main} and the auxiliary foil d_{aux} as well as the thickness d_{ins} and the relative permittivity ϵ_{ins} of the insulation material. In addition, the gaps between the foils and the insulation d_{air} can be taken into account. Additional reference data are: the permeability of free space $\mu_0 = 4\pi \cdot 10^{-7}$ H/m, the relative permeability of air $\mu = 1$ and the relative permittivity of vacuum $\epsilon_0 = 8.854 \cdot 10^{-12}$ F/m.

It is assumed that modern computer tools allowing programming, such as MATLAB, Octave or Scilab are used for calculations. The calculation flow chart is presented in Figure 2.4.

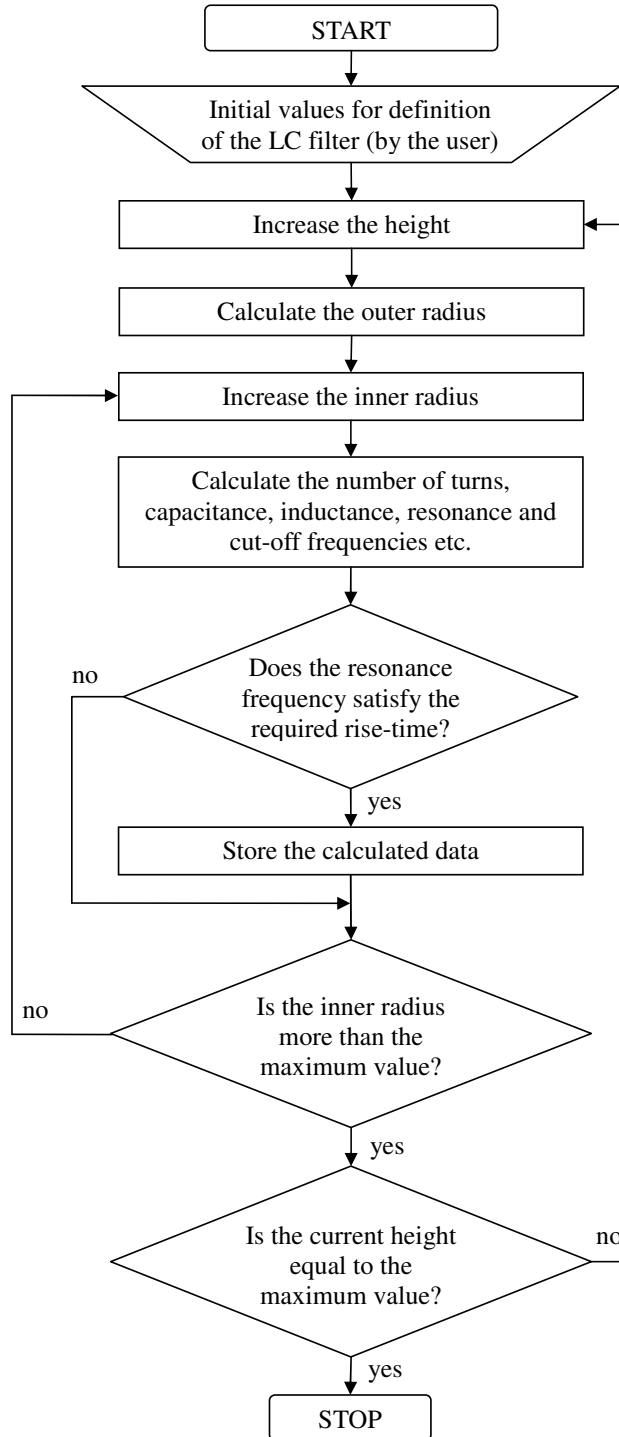


Figure 2.4. Flow chart of the calculation program.

The calculation program comprises two main loops. The first (outer) loop gradually increases the LC filter height. The second (inner) loop calculates the LC filter parameters at different inner radii. The limits for height and variation in the inner radius are defined by the user.

The number of turns in a column for two foil filter may be calculated by equation

$$N = \frac{r_{\text{out}} - r_{\text{inn}}}{d_{\text{main}} + d_{\text{aux}} + 2d_{\text{ins}} + 4d_{\text{gap}}}, \quad (2.6)$$

d_{main} , d_{aux} , d_{ins} , d_{gap} , respectively, are the thicknesses of the main and auxiliary foils, the insulation and the technological gap.

The mass of the hybrid LC filter column neglecting the column bandage:

$$m = \rho_{\text{main}} \cdot V_{\text{main}} + \rho_{\text{aux}} \cdot V_{\text{aux}} + \rho_{\text{ins}} \cdot V_{\text{ins}} + \rho_{\text{frame}} \cdot V_{\text{frame}}, \quad (2.7)$$

where ρ_{main} , ρ_{aux} , ρ_{ins} , ρ_{frame} are the densities of the main foil, auxiliary foils, insulation and frame materials that can be found in the reference literature (Lide 2003); $V_{\text{main}} = A \cdot d_{\text{main}}$, $V_{\text{aux}} = A \cdot d_{\text{aux}}$, $V_{\text{ins}} = A \cdot d_{\text{ins}}$, $V_{\text{frame}} = 2 \cdot \pi \cdot r_{\text{frame}} \cdot h_{\text{frame}} \cdot d_{\text{frame}}$ are the volumes of the main and auxiliary foils, insulation and frame, respectively; $A = l \cdot h$ is the area producing the capacitance; $l = 2\pi \cdot r_{\text{mid}} \cdot N$ is the length of each layer; r_{mid} is the radius of the centre of the hybrid LC filter winding (see Figure 2.5), and r_{frame} , h_{frame} , d_{frame} are the radius, height and thickness of the frame, respectively.

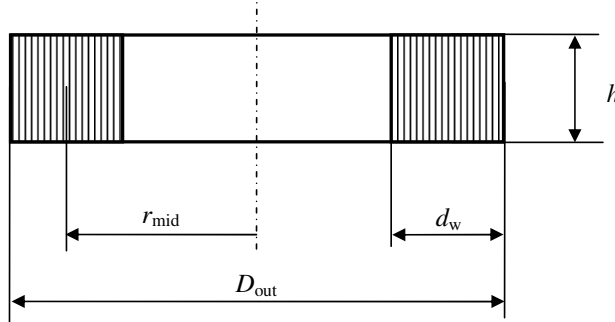


Figure 2.5. Dimensions of the hybrid LC filter needed in the inductance calculation.

The mass of the three-phase hybrid LC filter

$$M_w = 3 \cdot m + m_{\text{cov}}, \quad (2.8)$$

where m_{cov} is the mass of the cover.

The capacitance C_b between the main and auxiliary foils with an acceptable practical accuracy can be considered as the capacitance between two rectangular plates (Pohl 1960):

$$C_b = \varepsilon \cdot \varepsilon_0 \cdot \frac{A}{d_{\text{ins}}}, \quad (2.9)$$

where ε is the relative permittivity of the insulation material, ε_0 is the permittivity of the vacuum and A is the surface of the main foil.

Inductance calculation is more complex than the capacitance calculation. This is described for instance in (Kalantarov and Tseitlin 1986). For a solenoid with a rectangular shape of the winding cross-section (Figure 2.5), the following expression can be given:

$$L_1 = \frac{\pi}{4} \cdot \mu \cdot \mu_0 \cdot N^2 \cdot \frac{2 \cdot r_{\text{mid}}}{\alpha} \cdot (K_a - k), \quad (2.10)$$

where μ is the relative permeability of the core material ($\mu \approx 1$ for air). For the LC filter in question, K_a and k are values that can be found from the tables presented in (Kalantarov and Tseitlin 1986); these values are based on the geometric relations of the filter $\alpha = \frac{h}{2 \cdot r_{\text{mid}}}$, $\rho = \frac{d_w}{2 \cdot r_{\text{mid}}}$ and $\gamma = \frac{\rho}{\alpha} = \frac{d_w}{h}$, where d_w is the thickness of the LC filter winding. For manual calculations, Figures 2.6–2.7 can be used.

According to (Kalantarov and Tseitlin 1986), despite the complexity of the calculations, the errors are very small in the inductance values obtained this way.

At the resonance frequency, inductive and capacitive impedances are equal ($L_1 \omega_r = \frac{1}{C_b \omega_r}$).

Therefore, the angular resonance frequency is

$$\omega_r = \frac{1}{\sqrt{L_1 C_b}}. \quad (2.11)$$

Resonance frequency is

$$f_r = \frac{\omega_r}{2\pi}. \quad (2.12)$$

If we represent the HLCF as a simple voltage divider (Pavlic 2008), the following transfer function can be obtained:

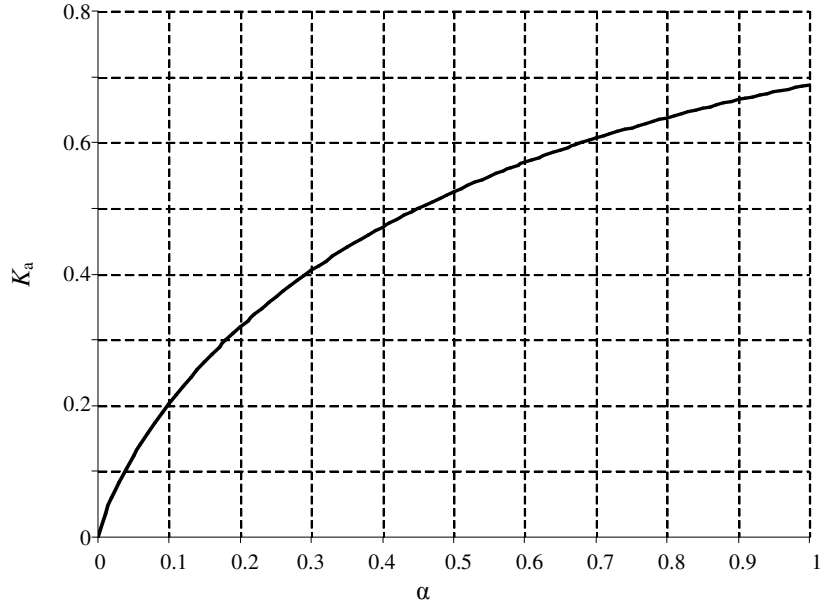
$$W_{\text{HLCF}}(s) = \frac{1}{L_1 C_b s^2 + 1}. \quad (2.13)$$

The Bode diagram for the transfer function (2.13) is shown in Figure 2.8.

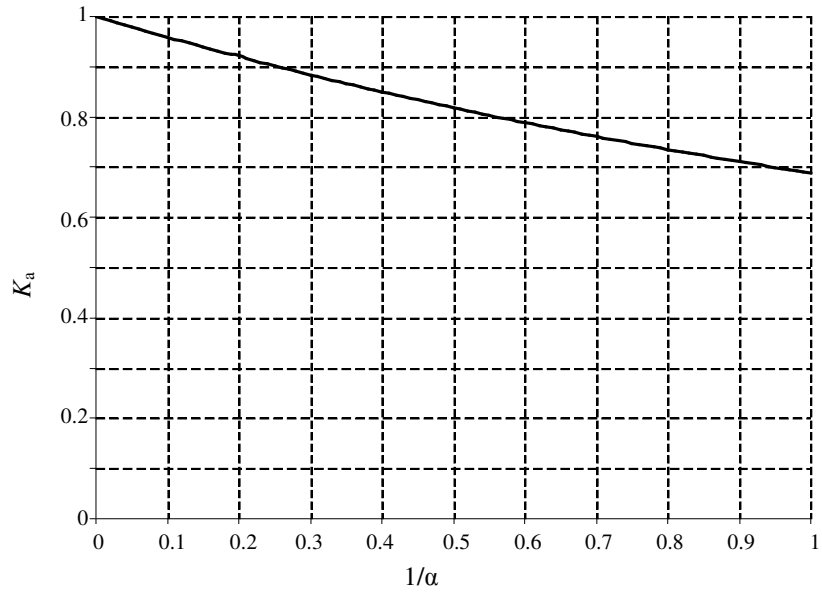
If we take into account the series resistance of foils, Eq. (2.13) transforms to

$$W'_{\text{HLCF}}(s) = \frac{1}{L_1 C_b s^2 + R_{1,\text{ac}} C_b s + 1}, \quad (2.14)$$

where $R_{1,\text{ac}}$ is the alternating current resistance of the main foil. Thus, the resistance of the main foil determines the damping factor.



a)



b)

Figure 2.6. Curves for the K_a value to be used in Eq. (2.10). (a) For $\alpha \leq 1$. (b) For $\alpha \geq 1$.

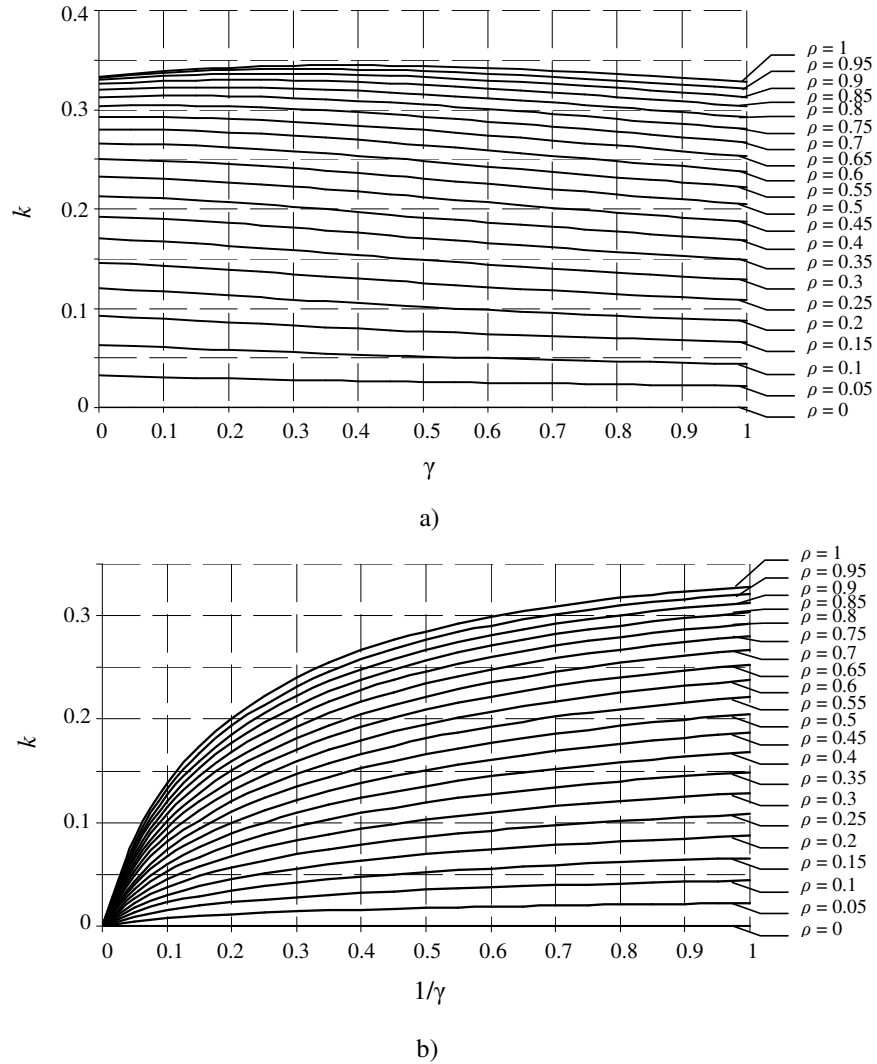


Figure 2.7 Curves for the k value in Eq. (2.10) at different values of ρ . (a) For $\gamma \leq 1$. (b) For $\gamma \geq 1$.

It is well known that designers developing high-frequency applications have to take into account the non-uniform current distribution inside a conductor cross-section. This is a result of magnetic fields produced by the interaction between the turns (Ha and Harbrough 1976). This effect is regarded as an AC resistance increasing with frequency and, therefore, contributing to filter resonance attenuation.

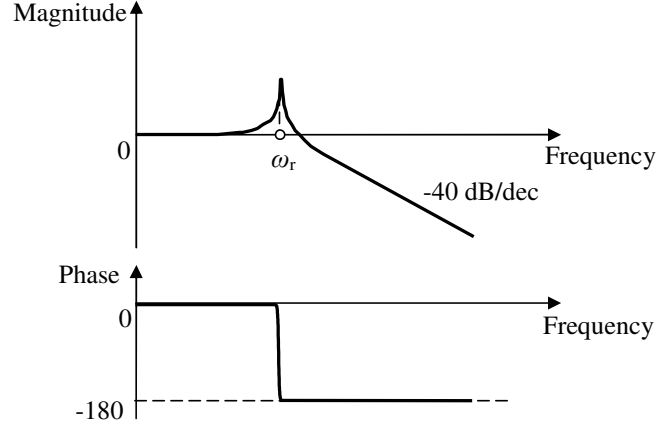


Figure 2.8. Bode diagram of the simplified HLCF transfer function (2.13).

For a round wire in free space, the following equation can be used for the calculation of the skin depth layer (Mohan et al. 2003, Bossche and Valchev 2005):

$$\delta = \sqrt{\frac{2\rho}{\omega\mu_0\mu_c}} \quad (2.15)$$

where ρ is the resistivity of the round wire material presented in Table 2.1 for some metals, ω is the angular frequency at which the skin depth is calculated and μ_c is the relative magnetic permeability of the conductor, which is close to 1 for aluminium and copper. Equation (2.15) can be useful in the evaluation of skin depth thickness.

The resistance at the frequency f can be calculated by equation (Robert et al. 2001):

$$R_{ac} = R_{dc} \cdot \left(\Delta \cdot \frac{\sinh 2\Delta + \sin 2\Delta}{\cosh 2\Delta - \cos 2\Delta} + 2\Delta \cdot \frac{n_f^2 - 1}{3} \cdot \frac{\sinh \Delta - \sin \Delta}{\cosh \Delta + \cos \Delta} \right), \quad (2.16)$$

where $R_{dc} = \rho_m \frac{l}{h_{foil} d_{foil}}$ is the resistance of the foil at direct current, ρ_m is the resistivity of the foil

material, h_{foil} and d_{foil} are the height and the thickness of the foil, respectively and $\Delta = \frac{d_{foil}}{\delta}$ is the relation of the foil thickness d_{foil} to the skin depth δ , n_f is the number of foils in one column.

To rewrite Eq. (2.14) in a complex form (the Laplace operator s should be replaced with $j\omega$), the magnitude at the resonance frequency in dB can be calculated with good accuracy using Eq. (2.11)

$$M_r = 20 \lg \left(\sqrt{\frac{L_1}{C_b R_{1,ac}^2}} \right) = 20 \lg(Q), \quad (2.17)$$

where Q is the quality factor of the system. Theoretically at $R_{1,ac} = 0$, $M_r = \infty$.

At frequencies higher than the resonance frequency, the input and output signals of the HLCF are in opposite phases. The next polynomial equation can be found:

$$-L_1 C_b \omega_{rwr}^2 + jR_{1.ac} C_b \omega_{rwr} + 1 + \frac{U_{out}(j\omega)}{U_{in}(j\omega)} = 0, \quad (2.18)$$

The next equation can be derived from (2.21):

$$\omega_{rwr} = \frac{\sqrt{4L_1 C_b (1 + A_{rwr}) - R_{1.ac}^2 C_b^2}}{2L_1 C_b}, \quad (2.19)$$

where $A_{rwr} = \frac{U_{out}(j\omega_{a,r})}{U_{in}(j\omega_{a,r})}$ is attenuation at the angular frequency ω_{rwr} .

The corresponding frequency is

$$f_{rwr} = \frac{\omega_{rwr}}{2\pi} \quad (2.20)$$

Thus, the cut-off frequency ($A_{rwr} = \sqrt{2}$) of filter at $R_{1.ac} = 0$ is

$$f_c \approx \frac{0.25}{\sqrt{L_1 C_b}} = 0.25\omega_r \quad (2.21)$$

2.4 Hybrid LC filter design technique

The specificity of the new hybrid LC filter described in section 1.6 requires a new design procedure, which can be based partly on existing procedures. The design technique should take into account the fact that electrical and geometric properties of the HLCF are inseparably interconnected. Such an approach is not applied to conventional LC filters. On the other hand, the design technique should include a complex of other factors that are usually taken into account in conventional LC filter and inductor design. Some of these questions were already addressed in this work, and they will be combined into a complete method in this section. The accent of the proposed design is mostly on du/dt filters.

In the literature we can find few references on the electrical design of conventional passive filters. Although Salomäki (2007) has mentioned the usage of LC filters without resistors, the authors prefer to consider RLC filters with overdamping resistors in series with the filter capacitances. However, such an approach leads to electrical and dimensional oversizing of the filter components. This results in extra expenses.

A quite simple practical approach is presented by von Jouanne and Enjeti (1997). Inherently, the desired filter parameters are calculated from cable parameters, the desired overshoot and the reflection coefficient. The drawbacks of this method are that the reflection coefficient and the cable parameters, for example length, are not always known and the relation between the filter inductance and capacitance is only vaguely defined. Lee and Nam (2004) criticize this uncertainty and propose separate equations for calculation of the filter inductance and capacitance using, however, the reflection coefficient and cable parameters again. Both methods do not take into account stray

impedances, even though Rendusara and Enjeti (1998) showed that the filter high-frequency performance may be still acceptable for a medium-power drive.

The proposed design method is based on the calculation technique presented in section 2.3. Equations from this section may also be used as a basis for HLCF calculations with other considered methods of electrical design.

Most of the existing design procedures are intended for inductors with magnetic cores and cannot be applied as such to the hybrid LC filter design, in particular, because selection of the magnetic core is a central part of these designs. In fact, magnetic materials could be successfully used in hybrid LC filters, but the subject is outside the scope of the current work. Mohan et al. (2003) and McLyman (2004) discuss magnetic core inductor design procedures with thermal considerations. However, these methods do not pay attention to stray impedances of the inductor, assuming that the high-frequency behaviour of the inductor is determined advantageously by the properties of the core material. Terman (1943), when considering air-core coils, takes into account the parasitic distributed capacitance as an element in parallel with the inductance of the coil. Inductance equations for different structures are also presented in the book. However, none of them is appropriate for the case under consideration. Kalantarov and Tseitlin (1986) give a large number of equations for inductors of different configurations. The equations are presented in a general form making them flexible for a wide range of applications. This fact allows to use Eq. (2.10) for a solenoid with a rectangular winding cross-section in the calculation of an air-core hybrid LC filter. The use of foils for inductor winding is considered by Van der Bossche and Valchev (2005). The authors pay special attention to insulators between the foils as well as to stray capacitances between the turns.

The flow chart of the proposed technique presented in Figure 2.9 for hybrid LC filter design includes determination of the attenuation range, evaluation of the required resonance frequency, selection of materials, HLCF calculation, choosing the electrical topology, electrical and thermal simulations, cooling system design (if it is required and acceptable), column arrangement and cover design.

Resonance frequency can be determined with Eq. (2.5). Some definite pulse rise time is usually required by a customer and can be determined from the corresponding standards. The filter common-mode attenuation range can be evaluated using the procedure presented in section 2.1.

Before the calculations, the main and auxiliary foils as well as the insulation layer materials should be chosen according to the recommendations in section 2.2.

The main proportions of the HLCF should also be defined before the calculations. Let us consider this aspect in more detail.

Because a hybrid LC filter is part of the drive, it should satisfy the specific requirements of an actual application. Low cost, small dimensions and a low mass are among the most important requirements in the majority of the cases. Such characteristics are interrelated and depend on material consumption and (to a less degree) on technology costs.

The capacitance and the inductance of the HLCF determine its attenuation properties. Equation (2.9) for capacitance shows that there are three ways to reach the desired attenuation by capacitance: using an insulation material with as high permittivity as possible, decreasing the thickness of the insulation and increasing the area between the foils. In practice, the permittivities of insulators are limited. Reduction of the insulation thickness is restricted by mechanical properties and the dielectric strength of the insulation material. Increasing of the area between the foils leads

to an increase in the volume of the insulation layers and, therefore, to a higher cost. On the other hand, implementing connection between the filter star point and the DC link midpoint (Figure 1.18) having potential close to zero (section 1.2), a high value of filter capacitance can cause earth fault detector triggering in the frequency converter (situation is rather similar with a failure caused by straight electrical connection of the cable conductor to ground).

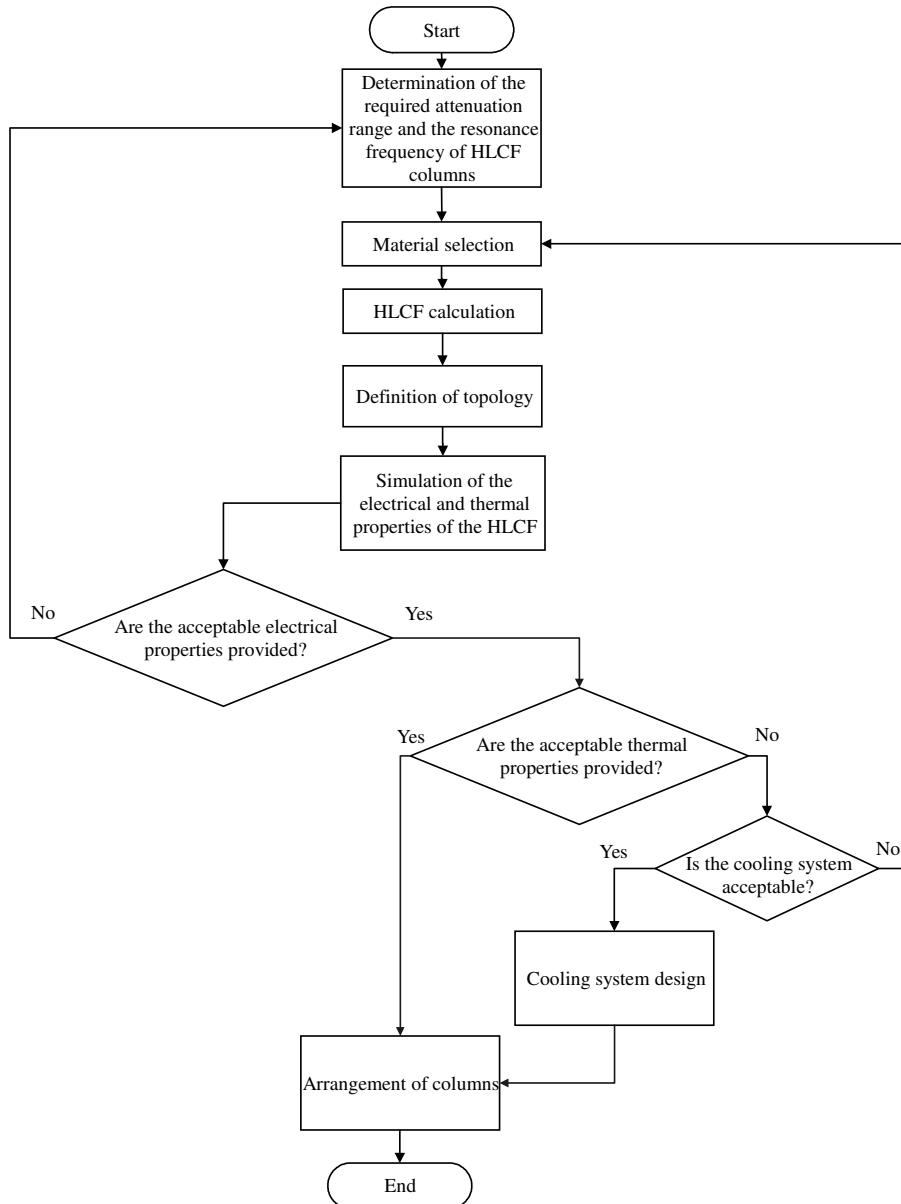


Figure 2.9. Flow chart for hybrid LC filter design.

The analysis of Eq. (2.10) for the inductance shows that there are at least the following alternatives for increasing the inductance: selection of a core with a high permeability μ , increasing the number of turns N , decreasing the middle radius r_{mid} and the height h of the coil and increasing the coil winding thickness d_w . The drawback of an excessive inductance can be an undesirable increase in the amplitudes at frequencies close to resonance, which is expressed by Eq. (2.17). The restriction of inductance increasing is the voltage drop across the inductor which shouldn't be too large.

Now it is evident that the filter capacitance requires significant heights of the HLCF, while the inductance demands a larger diameter. In other words, the aspect ratio h_D determined by Eq. (2.4) for a choke with a high capacitance approaches infinity, and with a high inductance it approaches zero. An analysis shows that the dependencies of the inductance and the capacitance versus the material volumes have the shapes presented in Figure 2.10.

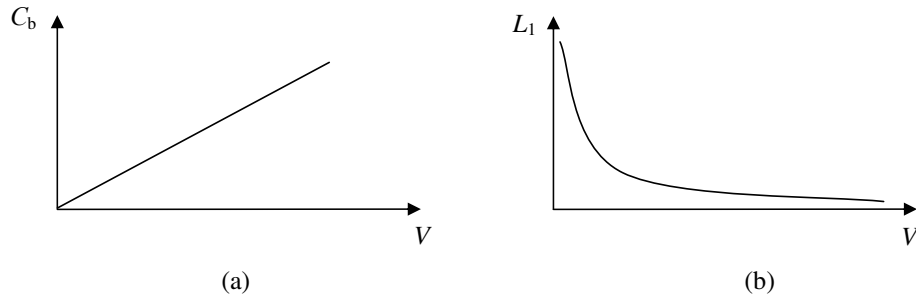


Figure 2.10. Main capacitance (a) and main inductance (b) versus the volume of the required materials at a constant resonance frequency.

The required volume of materials taking part in the electrical processes can be expressed by the equation

$$V = A \cdot (d_{\text{main}} + d_{\text{aux}} + d_{\text{ins}}). \quad (2.22)$$

The area of the layers can be found by substituting Eqs. (2.9) and (2.10) into Eq. (2.11):

$$A = \frac{d_{\text{ins}} h}{k_m \omega_r^2 N^2 r_{\text{mid}}^2 (K_a - k)}, \quad (2.23)$$

where $k_m = \varepsilon \varepsilon_0 \pi \mu$ is a coefficient that takes into account the properties of the insulation and the core.

By substituting Eq. (2.23) into Eq. (2.22), we may write

$$V = \frac{h d_{\text{ins}} (d_{\text{main}} + d_{\text{aux}} + d_{\text{ins}})}{k_m \omega_r^2 N^2 r_{\text{mid}}^2 (K_a - k)}. \quad (2.24)$$

It is evident from Eq. (2.24) that the volume of materials used can be effectively reduced by increasing the number of turns N and by increasing the radius of the centre of the winding r_{mid} as well as by decreasing the column height h . This fact also implies that the filters with a low aspect ratio h_D defined by Eq. (2.4) are the most profitable ones. It was mentioned that the inductance

domination permits to decrease the aspect ratio; therefore, the most cost-effective solutions can be reached this way.

In (El-Husseini et al. 2002), the thermal properties of film capacitors that have a similar construction with the HLCF are considered. This work allows us to assume that high aspect ratios of the HLCF will also lead to essential heating of the columns.

On the other hand, increasing the number of turns is advisable because of the intra capacitance of main foil. This capacitance is a set of capacitances between the turns of each foil connected in series; this is the reason why its value is much lower than the value of the capacitance between the foils C_{b1} . Capacitance between the middle turns of winding is equal to $\frac{C_{b1}}{N-1} \cdot \frac{d_{ma}}{d_{tt}}$, where d_{ma} and d_{tt} , respectively, are the distances between the main and auxiliary foils and between the nearest turns of the same layer. Capacitances between other turns differ from the capacitance between the middle turns proportionally to their radii. Thus, for the case when the insulation between all the layers has the same thickness, the intra capacitance of the foil can be estimated with the help of the main capacitance and geometric relations

$$C_i = \frac{1}{\sum_{N_i=1}^{N-1} \frac{N-1}{C_{b1}} \cdot \frac{d_{tt}}{d_{ma}} \cdot \frac{r_{mid}}{\left[r_{in} + \frac{d_w}{N-1} \cdot (N_i - 0.5) \right]}}. \quad (2.25)$$

Intra capacitances of the foils are not taken into account in the analysis by simplified transfer functions (2.13) and (2.14), but have to be considered in a full model. As it is shown in Chapter 3 of this work, the intra capacitance of the main foil is the reason for the decrease in attenuation at high frequencies.

Equation (2.25) shows that the intra capacitance can be effectively decreased with a large number of turns. On the other hand, a small number of turns is more convenient with respect to manufacturing considerations. However, in this case, the attenuation needed will be provided by the capacitance that requires more area between the main and the auxiliary layers. Further, the height has to be increased, which is not allowable in many applications. Yet another drawback is the increase in the volume of materials required, as determined by Eq. (2.24).

After the determination of the geometric dimensions, the HLCF can be calculated using the algorithm and equations presented in section 2.3 or procedures of overdamping circuit calculation from corresponding papers (von Jouanne and Enjeti 1997, Lee and Nam 2004).

If a resistance R_f is added in series with the capacitance, the next transfer function can be written (von Jouanne and Enjeti 1997):

$$W_{\text{HLCF}}^*(s) = \frac{R_f C_b s + 1}{L_1 C_b s^2 + (R_{l.ac} + R_f) C_b s + 1}. \quad (2.26)$$

Equation (2.26) and Figure 2.11 (a) show that an additional resistance R_f can effectively attenuate the resonance but the numerator of Eq. (2.26) now contains a differentiator, and therefore the high-frequency attenuation of such a system will be much worse than that provided by a system without an additional resistance R_f . For example, the cut-off frequency of a filter with a resistor f_{cR} is shifted rightwards compared with the cut-off frequency of the LC filter f_c . Thus the pulse rise time t_{rR} and

the voltage overshoot σ_R in time domain will be less compared with a signal without an additional resistor, which is characterized by the rise time t_r and the overshoot σ (Figure 2.11 (b)).

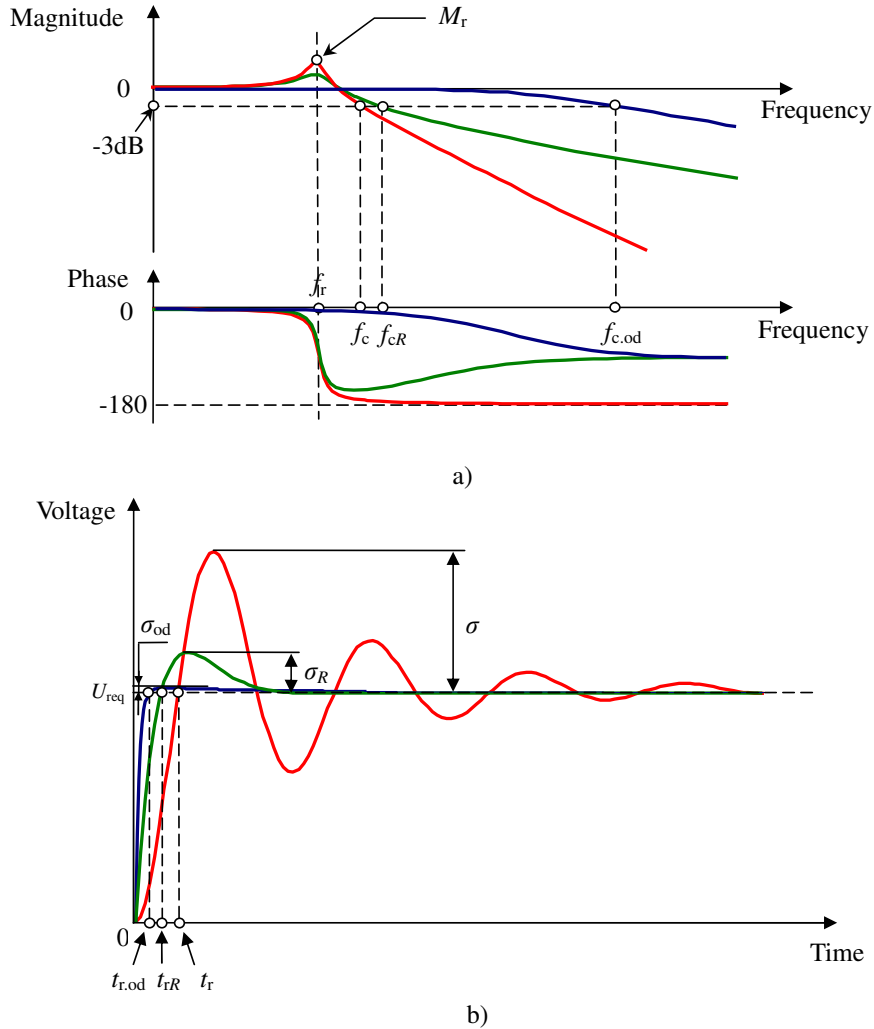


Figure 2.11. Bode diagrams (a) and step responses (b) of the transfer functions Eq. (2.14) (red line), Eq. (2.26), when the system is not overdamped (green line) and Eq. (2.26) when the system is overdamped with an excessive resistance R_f (blue line).

If the resistance R_f has an excessive value, the system is overdamped. In this case amplification at resonance frequency is low, but the cut-off frequency $f_{c.od}$ is quite high so that the effectiveness of the filter is lower and the rise time of the pulse $t_{r.od}$ is short. However, resonance attenuation of this kind is recommended in the literature (von Jouanne and Enjeti 1997, Lee and Nam 2004). This may be explained by a compromise between the resistor R_f value and the dissipated losses (the larger the resistance is, the lower its power factor) and by low overshoots σ_{od} (Figure 2.11 (b)).

The value of an additional resistance in non-overdamped system ($A_r > \sqrt{2}$) can be calculated with a good accuracy from Eq. (2.26) using Eq. (2.11):

$$R_f = \left(\sqrt{\frac{L_1}{C_b (A_r - 1)^2}} - R_{l,ac} \right). \quad (2.27)$$

In the case of a completely attenuated resonance $A_r = \frac{U_{out}(j\omega_r)}{U_{in}(j\omega_r)} = 1$, the additional resistance $R_f = \infty$ which is the same as an inductor L_1 without a branch with a capacitance C_b . At $A_r < 1$, R_f has an imaginary representation, which is an impractical case.

If the high-frequency current redistribution is neglected, Eq. (2.27) becomes:

$$R_f = \left(\sqrt{\frac{L_1}{C_b (A_r - 1)^2}} \right). \quad (2.28)$$

Another drawback of the resistors implementation is the deterioration of the common-mode noise attenuation as it follows from Eqs. (1.9) and (1.10).

Next, the electrical connection of the filter columns should be chosen. Some possible schemes for connection are presented in section 1.5. If there is an access to the DC link midpoint, the scheme presented in Figure 1.18 is possible. If the access to the midpoint of the inverter is complicated for one reason or another, the scheme presented in Figure 1.20 can be used. The price of the solution presented in Figure 1.19 is expected to be higher than in other cases. Moreover, insulators with increased voltage stress capability have to be implemented because of the large voltage levels applied. However, if a third foil layer is integrated to the HLCF, the presence of a DC link midpoint in the system becomes insignificant. Another alternative is to earth the auxiliary foils, but in a general case it may be recommended to use the DC link potentials. For example, if a substantial external common-mode voltage is applied to the DC link, the potentials of the phases versus earth are increased. Therefore, stress on the HLCF insulation becomes notably higher.

The next steps are the simulations of the calculated system with the electrical and thermal models. Such models can help in choosing the scheme for the connection of columns as well as the configuration of the cooling system and columns.

An electrical model of the HLCF can take into account the complex phenomena inside the HLCF such as the proximity effect, the inductance of auxiliary foils, the mutual inductance between the foils, the intra capacitances of the foils and the change in capacitances as a function of frequency. Modelling also allows to investigate the filter in time and frequency domains so that it offers better alternatives for the HLCF properties compared with the simplified transfer functions (2.13), (2.14) and (2.26). The model of the HLCF placed into the drive model can help in the evaluation of the effectiveness of the HLCF. Possible solutions for hybrid LC filter simulations are presented in Chapter 3 of this work.

If the thermal model indicates high temperatures inside the HLCF, there are many alternatives to improve the situation; for instance, the insulation layer can incorporate cooling channels with flowing water or some other cooling liquid, the coolers can be mounted inside a box or even inside the columns, and liquid dielectrics flowing through the system can be used instead of solid dielectrics. The main disadvantage of the cooling system is the additional expenses. However, high temperatures can be expected only in drives with shaft heights more than 400 mm, which are not the primary application target of du/dt filters (Gambica 2002). Nevertheless, the temperature of the HLCF winding should not exceed the maximum allowable temperature of the insulation (see Table 2.2 for some insulators).

If acceptable electrical and thermal properties are not provided, the HLCF should be recalculated with new input data based on the results obtained.

Finally, composition of the columns and the cover design should be made. The columns are wound tightly around a suitable core, for example a glass fibre tube. The columns must be vacuum impregnated to remove all air from the insulation, because the electric field strength is high between the main and auxiliary foils. If air bubbles are left in the impregnation, partial discharges are to be expected, and a premature failure of the filter will take place. To make the filter more resistant to partial discharges, the insulation material should contain mica. However, mica has a high permittivity, which makes the capacitance between the foils large thereby affecting the aspect ratio.

The terminals of the HLCF should have low impedances. The inductance of the terminals decreases HLCF attenuation at high frequencies. Any additional turns and bends are strongly undesirable. This is the reason to produce as short and straight terminals as possible in the actual application. It is recommended, of course, to use the materials with low resistivity constants.

The filter cover should be lightweight and EMC tight. It may have ventilation holes, but it must prevent any magnetic radiations from the HLCF to the environment; it should be earthed and have no electrical contact with the HLCF columns. For example, a metal grid cage alloyed with a high-temperature plastic with holes for cooling can be used. In some applications, the HLCF can be mounted into the same casing with power electronics.

The presented new design technique was used for the design of hybrid LC filter prototypes. Appendix A provides an example of the test setup hybrid LC filter design as well as comparison tables of the calculated and measured values for other prototypes.

Summary of Chapter 2

- The required attenuation range can be determined by simulations with the help of low- and high-pass filters in the frequency ranges where these filters have no effect on the simulated common-mode current.
- The most appropriate materials for the electrical part of the hybrid LC filters are copper or aluminium for foils, and solid insulators for the insulation layers.
- Proposed calculation technique is based on the desired pulse rise time, the results of the attenuation range simulation and information about the selected materials and dimensions, which can be defined by the user for an actual application. Because the calculations, especially the inductance calculation, are quite laborious, the use of computing tools is recommended.
- A hybrid LC filter is an oscillating link. If the requirements for overshoots in the target application are not strict, the filter may be calculated by the desired rise time criteria. If low values of voltage overshoots are required in the target application, an additional resistance should be used or additional losses in the circuit should be generated, for instance, by using lossy core material for the filter. A drawback of the additional resistance is a decrease in common-mode attenuation and power losses.
- The hybrid LC filter design technique includes new items compared with the existing common inductor design procedures such as determination of the attenuation range and calculation of the columns of the hybrid LC filter. New electrical models for the design technique are presented in Chapter 3. The design algorithm structure is renewed compared with the existing algorithms and includes evaluation of the required material selection, choosing a scheme for the electrical connection, calculation of the additional damping resistances, simulation of the electrical and thermal models, cooling system calculation (if it is required and acceptable), arrangement of columns and cover design.
- The volume of the materials used in a hybrid LC filter taking part in the electromagnetic processes depends on the height of the columns and (indirectly) on the column diameter. Thus, in order to provide cost-effective solutions, the aspect ratio of a hybrid LC filter's cross-section, described by Eq. (2.4), should be low. The volume of materials is also inversely proportional to the number of turns squared; this makes it possible to save on materials.

3 Hybrid LC filter in the frequency domain

3.1 Simplified electrical representation of a hybrid LC filter at low frequencies

Let us consider two electrodes a and b separated by an earthed electrode c as shown in Figure 3.1 (a). The electrode a is connected to an AC voltage source U_{in} , the electrode b to earth via an impedance Z and the plate c directly to earth. Three capacitances can be measured: C_{b1} , C_{b2} and C_{i1} . If the impedance between the electrode c and earth equals zero, all the current will flow via C_{b1} , cancelling the effectiveness of the capacitance C_{i1} .

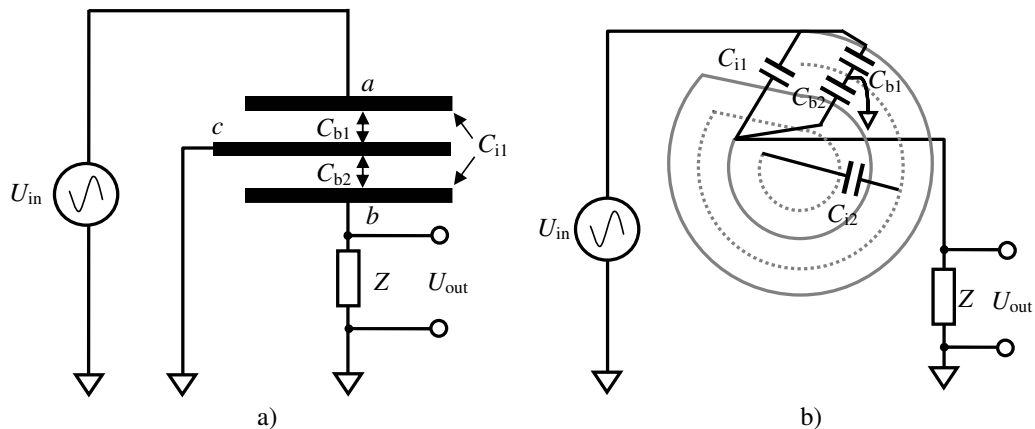


Figure 3.1. Capacitances between foils. (a) Cancellation of the intra capacitance at low frequencies. (b) Internal capacitances of the HLCF.

Fig. 3.1 (a) describes a plate capacitor with an extra foil c . Such a capacitor resembles a hybrid LC filter cross-section so that the electrodes a and b belong to the main foil while the electrode c belongs to the auxiliary foil (Figure 3.1 (b)). The intra capacitance of an inductor is formed between overlapping turns but in Fig. 3.1 (b) the capacitance C_{i1} is drawn between the inductor terminals as, according to circuit theory, the intra capacitance C_{i1} is connected in parallel with the inductor. At low frequencies the capacitance between the two foils C_{b1} effectively cancels the intra capacitance C_{i1} . Besides the capacitances presented in Figure 3.1 (a), there is also an intra capacitance between the terminals of the auxiliary winding C_{i2} , which at low frequencies is connected between the same potentials and, therefore, is negligible. Figure 3.1 shows that the capacitance C_{b2} due to the rolling nature of the hybrid LC filter is not effective.

To our understanding, the hybrid LC filter may be described by a set of inductances, resistances and capacitances. Schematically it may be represented as in Figure 3.2. The simplified circuit shows that the system has a transfer function of at least 8th order.

At low frequencies the main foil provides a low-impedance path for a signal. As it was shown above, the capacitance C_{b1} is the dominating capacitance in the system. In practice, only one of the auxiliary foil ends may be earthed. If both ends are earthed, the system is characterized as a transformer in a secondary-short-circuited mode; this mode may be considered as a test-mode only because of the high possibility of insulation injury (Langsdorf 1955). Therefore, almost no current will flow in the auxiliary foil at low frequencies and the mutual inductance has no influence since the coupling through C_{b1} is not dominating in the system. Thus, it is possible to suggest the

representation of the hybrid LC filter for low frequencies shown in Figure 3.3, which is a model of an ideal LC filter.

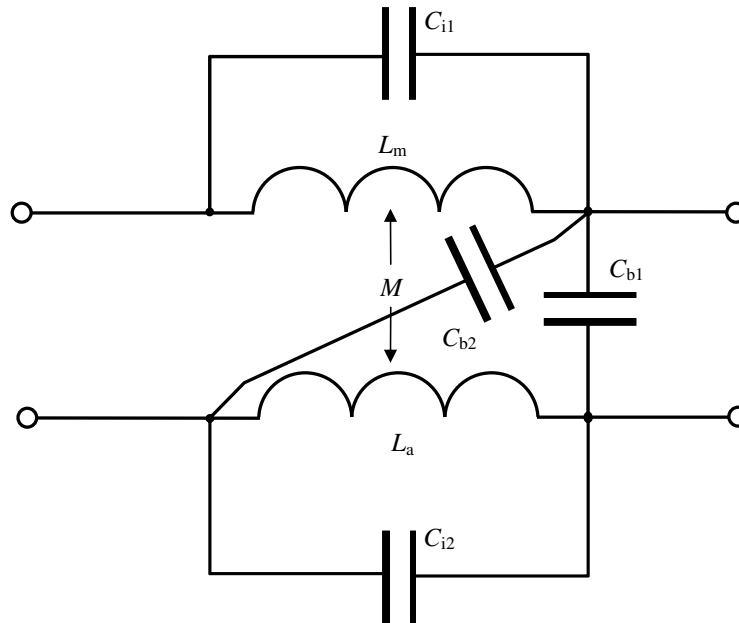


Figure 3.2. Simplified representation of the hybrid LC filter.

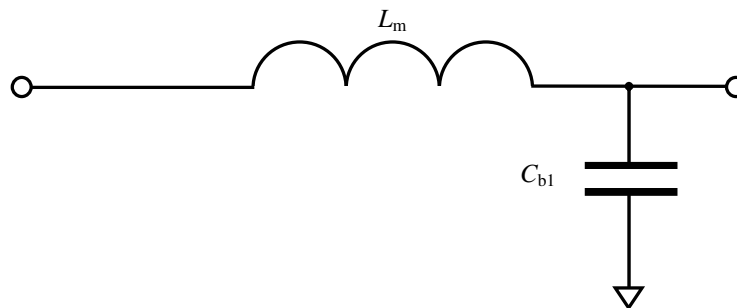


Figure 3.3. Simplified representation of the hybrid LC filter at low frequencies.

3.2. Hybrid LC filter electrical characteristics in the frequency domain

Let us consider a practical example with the low-frequency inductance $L_m = 50 \mu\text{H}$ and the low-frequency capacitance $C_b = 215 \text{ nF}$. The foil outputs and inputs are indicated by 1-1, 1-2, 2-1 and 2-2 (Figure 3.4).

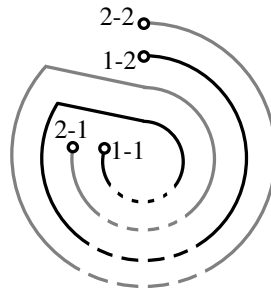


Figure 3.4. Terminals of the investigated filter.

The filter prototypes were analysed as separate units with an HP 4194A impedance and a gain-phase analyzer (HP 4194A 1996), which allows impedance measurement in the frequency range 100 Hz–40 MHz and gain-phase measurement in the range 10 Hz–100 MHz. For gain-phase measurements the analyzer comprises two precision resistances, a selectable R_{in} and a fixed $R_{out} = 50 \Omega$, as shown in Figure 3.5. For our investigations we used the minimum allowable input resistance $R_{in} = 50 \Omega$.

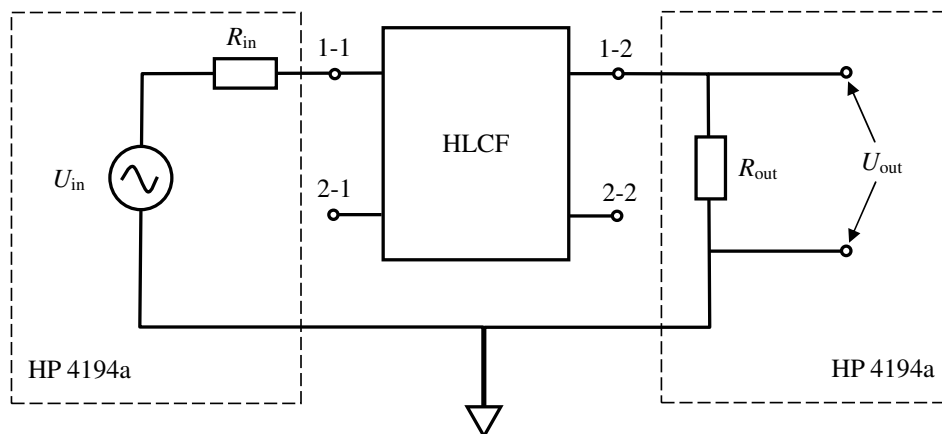


Figure 3.5. Obtaining the Bode plots with an HP 4194a frequency analyzer.

In order to further simplify the presentation of results, let us apply the following terminology:

- MAI for the gain-phase analyzer input-connected terminal of the main foil,
- MAO for the gain-phase analyzer output-connected terminal of the main foil,
- AE for the gain-phase analyzer earth-connected terminal of the auxiliary foil.

Figures 3.6 and 3.7 show the measurement results for the inductances of the foils and the capacitance between foils. The plots were captured assuming that the foil resistances are negligible. In both cases there are some resonances. This phenomenon was explained by Terman (1943) by apparent inductance. According to Young (1964), the “apparent inductance is the effective inductance value of an inductor due to the effects of its distributed capacity”, while “distributed capacity is self-capacity of the inductor due to method of winding”. In the current study, distributed capacitance is also called ‘intra capacitance’. The apparent inductance is described by equation:

$$L_{\text{ap}} = \frac{L_m}{\left(1 - \frac{f^2}{f_{oL}^2}\right)}, \quad (3.1)$$

where L_m is the coil inductance at low frequencies, f is the current frequency, f_{oL} is the frequency at which oscillation between the inductance L_m and the intra capacitance takes place.

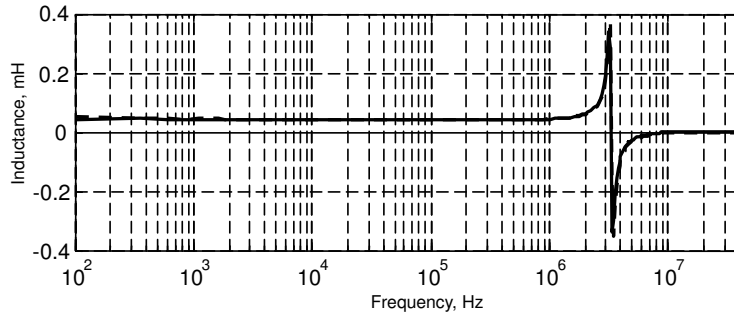


Figure 3.6. Apparent inductances of the main (solid line) and auxiliary (dashed line) foils of the prototype.

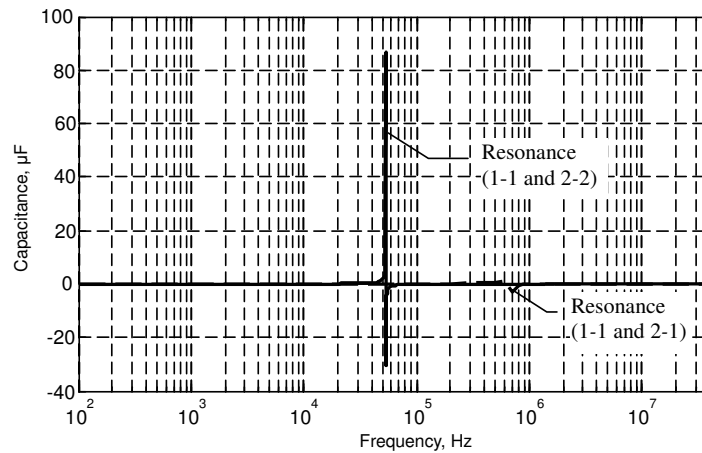


Figure 3.7. Apparent capacitance between terminals 1-1 and 2-1 (dashed line), 1-1 and 2-2 (solid line).

In a capacitance plot between terminals 1-1 and 2-1 there is a resonance that can be explained by the inserted inductances of the connection wires needed to connect the coil to the impedance analyzer. In the capacitance plot between the points 1-1 and 2-2 there is a large resonance caused by the capacitance between the foils and the self-inductance of the auxiliary foil.

Figures 3.8 and 3.9 show the impedances of the foils and also between the foils.

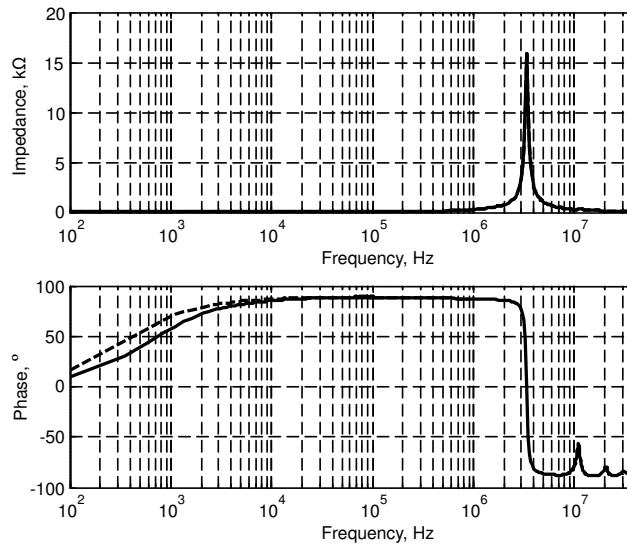


Figure 3.8. Impedances between terminals 1-1 and 1-2 (solid line) and terminals 2-1 and 2-2 (dashed line).

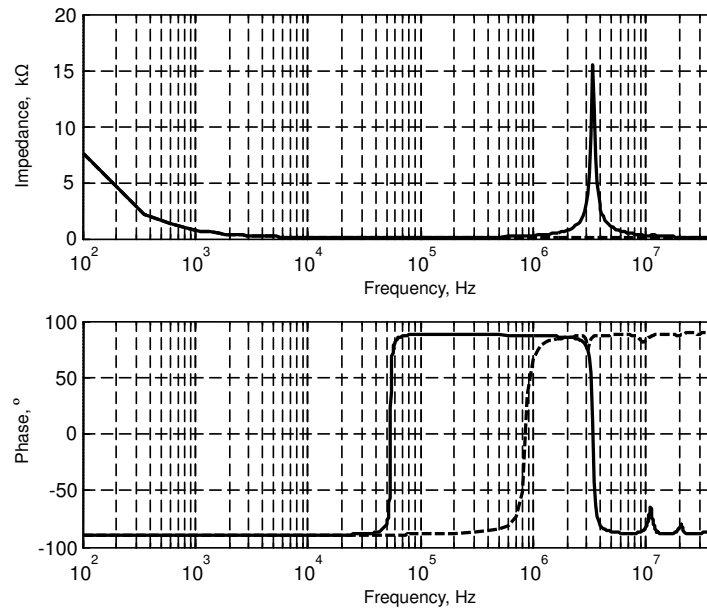


Figure 3.9. Impedance between terminals 1-1 and 2-1 (dashed line) and terminals 1-1 and 2-2 (solid line).

In Figure 3.8, the phase behaviour shows that at low frequencies up to 10 kHz the main impedance element is the resistance of the foil. After that the inductance of the foil is dominant, and after 2 MHz the distributed capacitance in the foil dominates. The resonance at ~ 3 MHz describes the resonance between the inductance and the intra capacitance of the main foil.

Figure 3.9 shows that at low frequencies the coupling between the foils is capacitive. The impedance between points 1-1 and 2-1 remains capacitive up to 800 kHz where the coupling changes to inductive. This phenomenon represents the inductance of the connection wires. Between points 1-1 and 2-2, the coupling becomes inductive already at 53 kHz (because of the inductance of the auxiliary foil). From 3 MHz onwards a capacitive coupling dominates again because of the intra capacitances of both the main and auxiliary foils.

Let us consider the gain-phase frequency responses. Figure 3.10 shows a Bode plot for single foils only (i.e. between terminals 1-1 and 1-2, 2-1 and 2-2) at different connections to the input/output channels of the HP 4194a analyzer.

All four curves have the same shape, and at about 3.5 MHz there are resonances between the main inductances and the intra capacitances of foils. Soft phase changing at this resonance frequency can be explained by current redistribution in the foils at high frequencies leading to rising values of the self-resistances of the foils.

The red and blue curves in Figure 3.11 show the Bode plots for two configurations: MAI 1-1 MAO 1-2 AE 2-1 and MAI 2-1 MAO 2-2 AE 1-2. Up to approximately 750 kHz, the hybrid LC filter behaviour can be described by an LC filter transfer function. Now, the resonance between the main inductance and the capacitance is completely suppressed by the resistance R_{in} , which also decreases the attenuation (about -25 dB/dec instead of -40 dB/dec, which characterizes the system presented in Figure 3.3). After 750–800 kHz, the attenuation starts to be constant (about -32 dB) up to approximately 10 MHz, and then falls with a slope equal to about $+20$ dB/dec in the frequency range from 10 MHz to 100 MHz. The green and turquoise curves in Figure 3.11 were obtained at an inversed connection of the foils to the analyzer. Their shape is similar with the shape at the original connection. However, maximum attenuation is higher (about -37 dB).

Similar outcomes can be produced for Figure 3.12, which shows the results of earthing the external turns of the filter. However, now two resonances occur and the phase shape is different in the range from 600 kHz to 8 MHz, which indicates modification of the internal electrical scheme compared with the scheme of Figure 3.11.

It is shown in section 3.6 and subsections 4.3.3–4.3.5 that a key factor determining HLCF performance is: next to which terminal (signal input or signal output) of the main foil the auxiliary foil is earthed? If the auxiliary foil is earthed next to the signal input terminal of the main foil, HLCF is used most effectively.

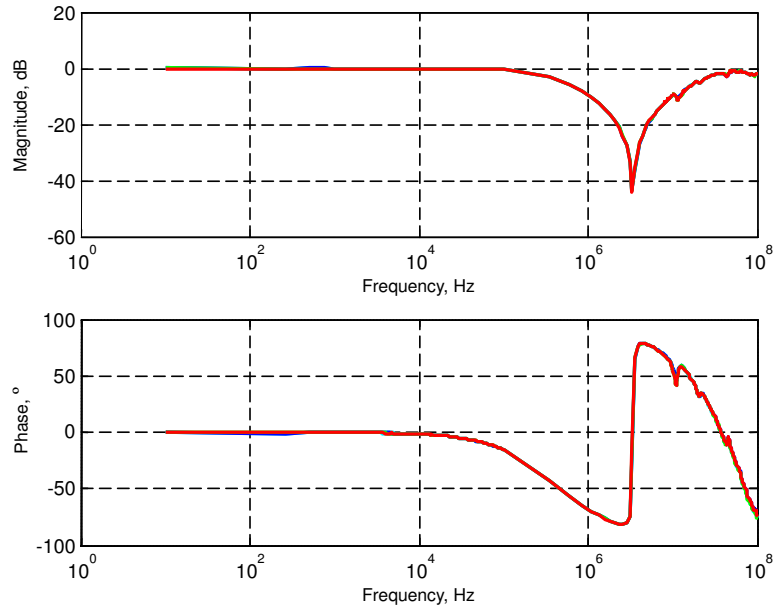


Figure 3.10. Bode plots of the main or auxiliary foil when the other one is not grounded ($L_m = 47 \mu\text{H}$, $C_{b1} = 210 \text{ nF}$). All the curves have the same shapes: MAI 1-1 MAO 1-2 (red); MAI 1-2 MAO 1-1 (green); MAI 2-1 MAO 2-2 (blue); MAI 2-2 MAO 2-1 (turquoise). All four curves have the same shape so that only the red curve is seen.

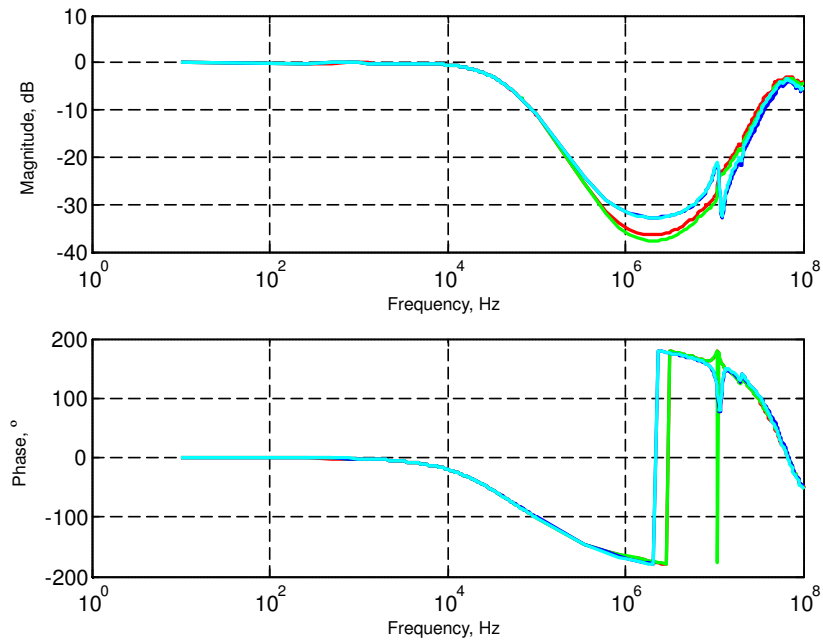


Figure 3.11. Bode plots with earthed auxiliary foil ($L_m = 50 \mu\text{H}$, $C_{b1} = 215 \text{ nF}$). MAI 1-1 MAO 1-2 AE 2-1 (red curve); MAI 1-2 MAO 1-1 AE 2-1 (green curve); MAI 2-1 MAO 2-2 AE 1-2 (blue curve); MAI 2-2 MAO 2-1 AE 1-2 (turquoise curve).

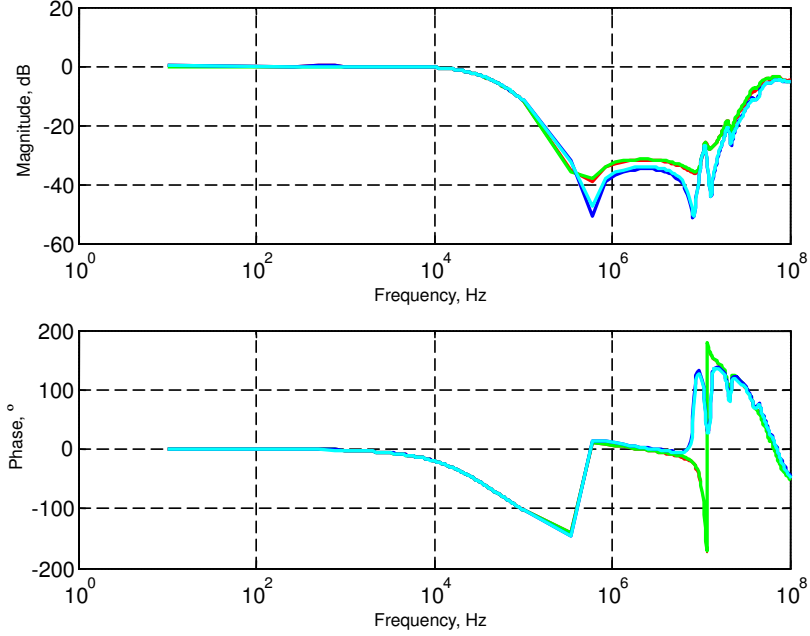


Figure 3.12. Bode plots with earthed auxiliary foil ($L_m = 50 \mu\text{H}$, $C_{b1} = 215 \text{ nF}$). MAI 1-1 MAO 1-2 AE 2-2 (red curve); MAI 1-2 MAO 1-1 AE 2-2 (green curve); MAI 2-1 MAO 2-2 AE 1-1 (blue curve); MAI 2-2 MAO 2-1 AE 1-1 (turquoise curve).

The presented curves and the analysis show the complexity of the processes taking place in the hybrid LC filter at high frequencies regardless of its simple construction. That is the reason why analytical consideration of processes that may take place in HLCF is necessary.

3.3 Current redistribution effect

In (Ha and Harbrough 1976), a comprehensive analysis of the electrical behaviour of conducting metal strips is provided. Quite simple theoretical evaluations are supported by a good experimental background. Two theoretical cases, which describe the limits of the AC resistance increasing at low and high frequencies, are considered (Figure 3.13). At low to intermediate frequencies, the resistance of a spiralled strip can be described similarly as the resistance of a straight strip of infinite length (Figure 3.14 (a)), in other words, current is distributed evenly across the cross-section. At high frequencies, a spiralled strip can be replaced by an infinite stack of parallel strips that produce a common magnetic field around the whole stack. This common magnetic field causes the current to flow closer to the edges of the strips as it is illustrated in Figure 3.14 (b). At intermediate frequencies, the AC resistance lies between these two cases. The lower frequency limit of the intermediate range can be determined based on the classical depth of penetration by equation:

$$f_{i,\text{str}} = \frac{4}{\pi \mu_0 \sigma_m d_{\text{str}}^2}, \quad (3.2)$$

where d_{str} is the strip thickness and $\sigma_m = 1/\rho$ is the conductivity of the strip material.

The resistance of an infinite strip can be described by

$$R_{\text{str}} = R_{\text{dc}} \frac{\sqrt{\pi\mu_0\sigma_m f}}{2} d_{\text{str}}. \quad (3.3)$$

The resistance of an infinite stack of strips can be described by

$$R_{\text{stk}} = R_{\text{dc}} \frac{\sqrt{\pi\mu_0\sigma_m f}}{2} H. \quad (3.4)$$

where H is the thickness of the stack (equal to the height of the spiralled strip spool).

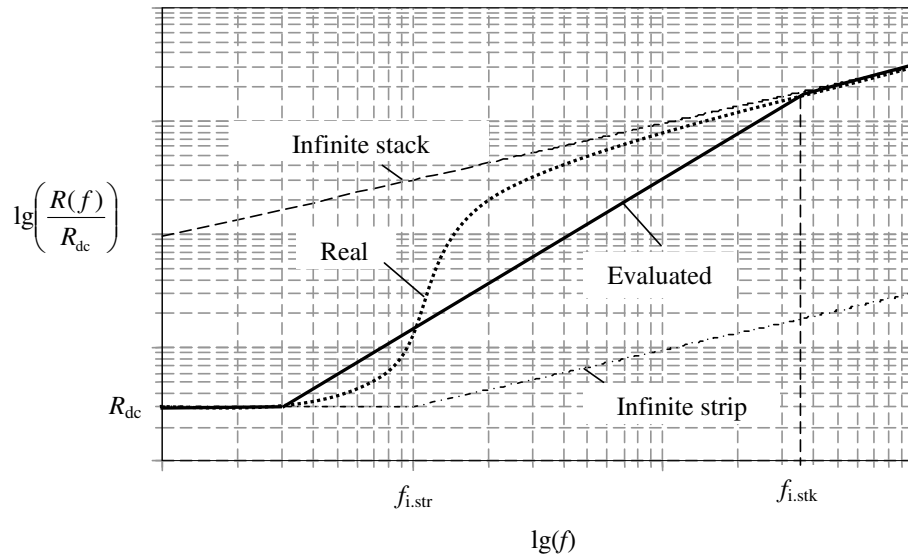


Figure 3.13. Resistance as a function of frequency according to (Ha and Harbrough 1976).

Thus, the resistance behaviour of the wound strip at intermediate frequencies can be considered as “transformation” of the resistance of an infinite strip to the resistance of an infinite stack. The resistance at high frequencies can be evaluated by Eq. (2.16).

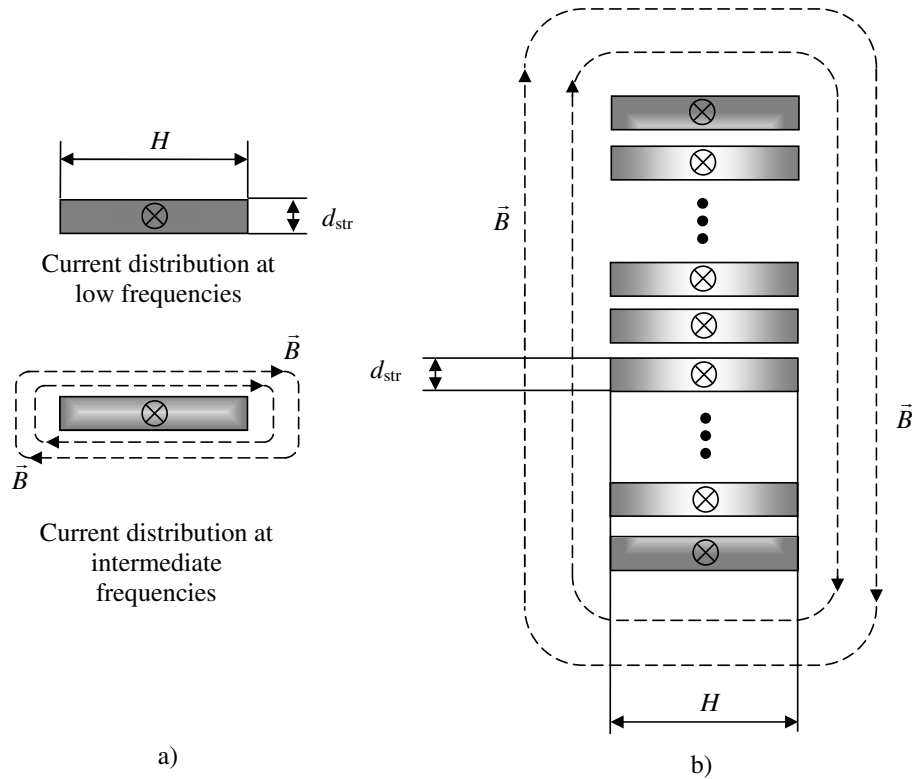


Figure 3.14. Infinite strip (a) and infinite stack (b) according to (Ha and Harbrough 1976).

3.4 Consideration of the main alternatives of the secondary foil earthing

The decrease in attenuation at high frequencies can be explained by the stray and inserted inductances and capacitances: the mutual inductance between the foils, the intra capacitance of the main foil, the inductance of connection wires, and so on. The assumptions made in section 3.1 are relevant if the current penetrates instantaneously through the hybrid LC filter. But the fact that the intra capacitance of the main foil is effective shows that at high frequencies the current penetration via the hybrid LC filter winding is nonuniform and depends on the method of auxiliary foil earthing.

There is a variety of possible hybrid LC filter earthing combinations. Here we concentrate on the system with two continuous foils coiled on an air-core with the following alternatives (the denotations remain the same as in Figure 3.4):

1. The earthed terminal of the auxiliary foil is 2-1 (Figure 3.15 (a)).
2. The earthed terminal of the auxiliary foil is 2-2 (Figure 3.15 (b)).
3. The auxiliary foil is earthed at both terminals 2-1 and 2-2 (Figure 3.15 (c)).
4. The auxiliary foil is earthed at the middle (Figure 3.15 (d)).

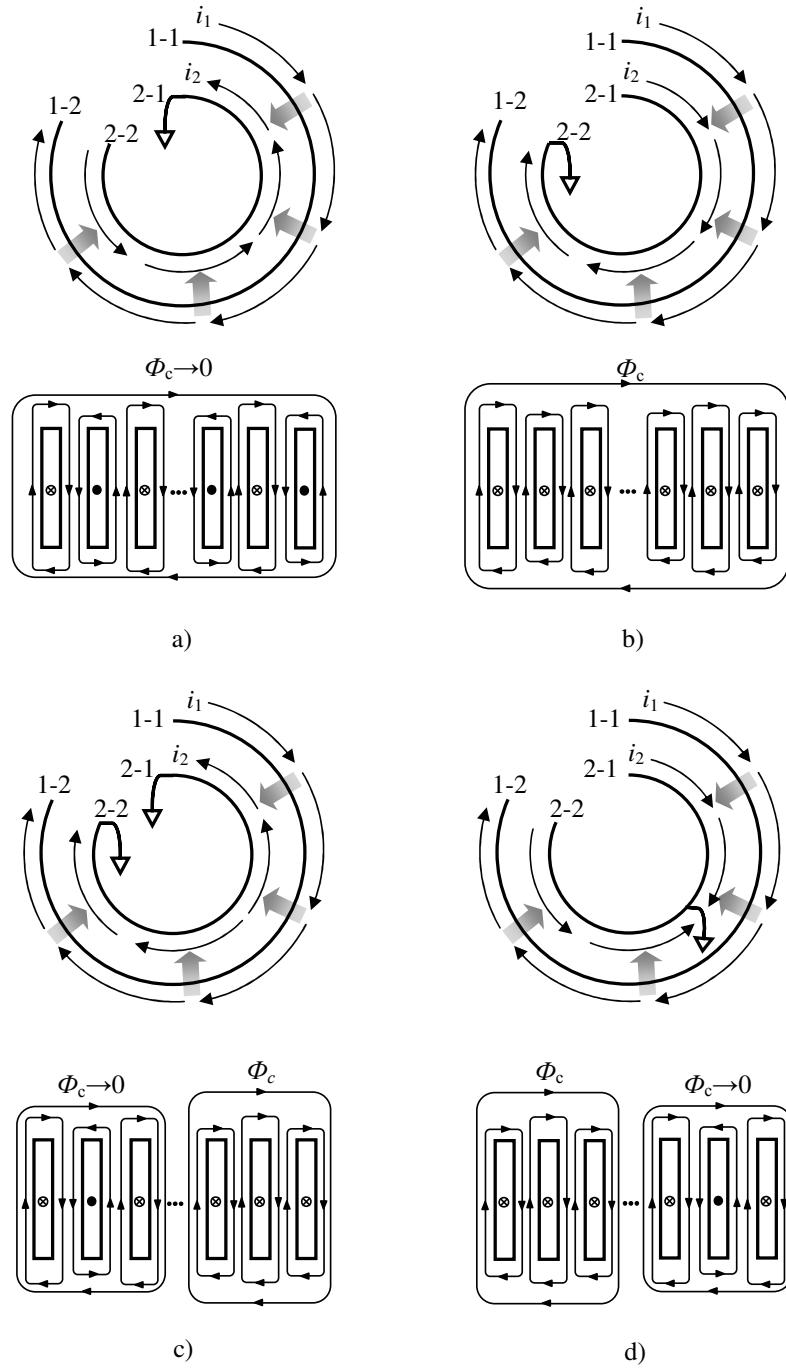


Figure 3.15. Different alternatives for auxiliary foil earthing at high frequencies. (a) The earthed terminal of the auxiliary foil is 2-1. (b) The earthed terminal of the auxiliary foil is 2-2. (c) The auxiliary foil is earthed at both terminals 2-1 and 2-2. (d) The auxiliary foil is earthed at the middle.

The case presented in Figure 3.15 (a) is characterized by different directions of currents flowing in the turns of the main and auxiliary foils. Therefore, the magnetic fluxes produced by the turns cancel each other preventing fast current redistribution with a rising frequency. In this case, the foils connected via the capacitance represent a back connection of magnetically coupled inductances. Thus, the inductance between terminals 1-1 and 2-2 tends to zero (Terman 1943) and the coupling is predominantly capacitive. Because the magnetic coupling factor between the foils is less than 1, there is some common flux that nevertheless produces current redistribution.

The case presented in Figure 3.15 (b) is characterized by the same current directions in the turns of both foils. Thus, there is a common flux Φ_c that forces the current redistribution. Now, the system may be considered as an accordant connection of two inductors with magnetic coupling. Therefore, mutual inductance has an important influence in this case.

The cases presented in Figure 3.15 (c) and (d) are characterized by a nonuniform magnetic flux distribution. The current redistribution in these cases basically correlates with Figure 3.13.

Figure 3.16 shows the difference in the resistance change for the considered alternatives. The test results for the prototype with $5.3 \mu\text{H}$ inductances of the foils and 38 nF capacitance between the foils with different earthing points are presented in Figure 3.17.

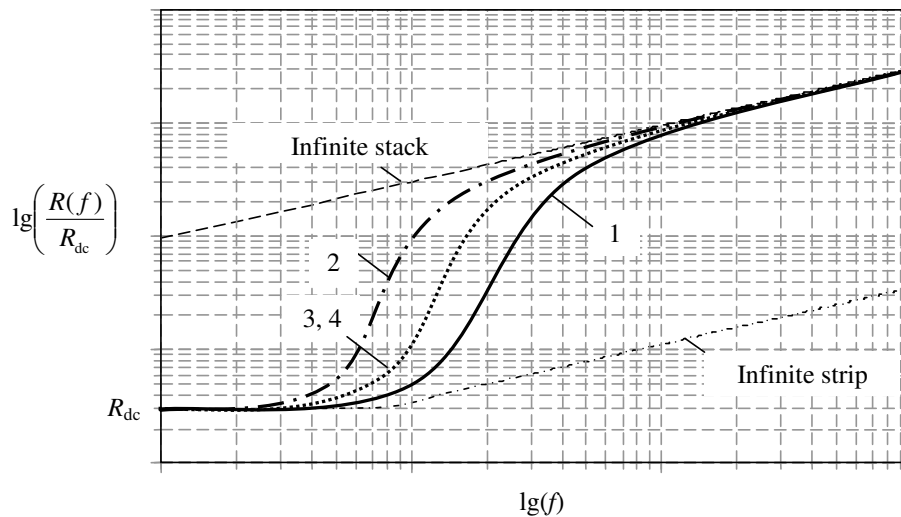


Figure 3.16. Resistance change as a function of frequency for different earthing points of the auxiliary foils: (1) according to Figure 3.15 (a); (2) according to Figure 3.15 (b); (3), (4) according to Figure 3.15 (c) and Figure 3.15 (d).

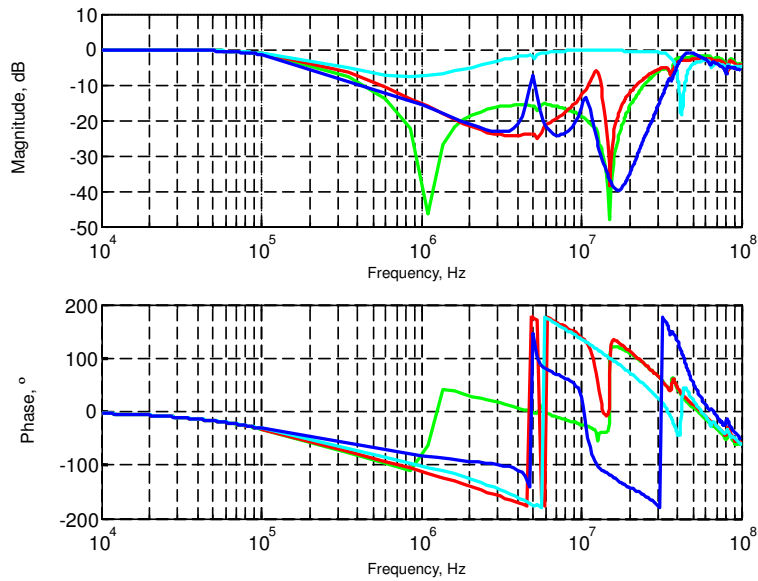


Figure 3.17. Frequency responses with different earthing points for the prototype ($L_m = 5.3 \mu\text{H}$, $C_{b1} = 38 \text{ nF}$). Red curve: according to Figure 3.15 (a); green curve: according to Figure 3.15 (b); blue curve: according to Figure 3.15 (c) (shorted aux foil); turquoise curve: Figure 3.15 (d).

Figure 3.17 shows that when the auxiliary foil is earthed at the middle, the system has the worst attenuation. The shorted auxiliary foil is not feasible in practice because it would cause large losses at low frequencies. It, however, would have the best attenuation between 100 kHz and 500 kHz.

The best attenuation can be reached when the auxiliary foil is earthed at either one of its ends. This is the reason to consider and compare these two cases in further investigations.

3.5 Hybrid LC filter model

The data presented in the previous sections show that the hybrid LC filter has a complex representation. An accurate model would consume a lot of system resources and could require a long calculation time. With such a model, the inserted impedances remain unaccounted for. For most of the cases, it suffices to have an electrical representation that is as simple and fast as possible, especially when the hybrid LC filter is only a part of a large drive model. Modern simulation tools, such as MATLAB or LTspice, permit to make an appropriate analysis in the time and frequency domains.

The results presented in Chapter 4 showed that the effective use of HLCF is possible if the auxiliary foils are connected together at the output terminal of the main foil. With that, the shape of the measured Bode plot does not have a significant importance. Thus, based on the investigations made, we may propose the model shown in Figure 3.18. The model takes into account the inductances of the main L_m and auxiliary L_a foils, the mutual inductance between the foils M , the AC resistance of the foils R_{ac} , the main capacitance C_b and the intra capacitances of the main C_{i1} and auxiliary C_{i2} foils.

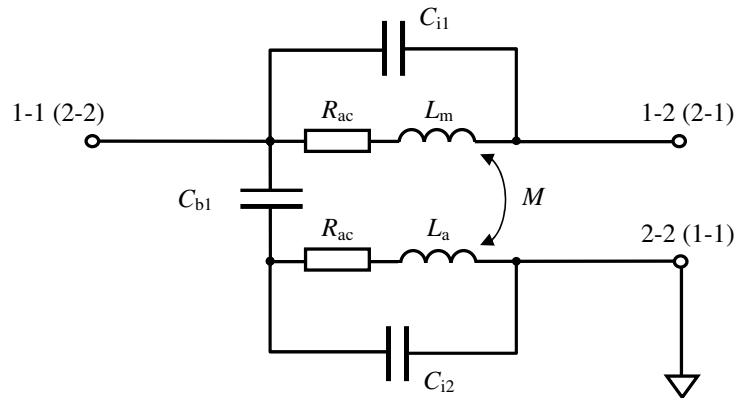


Figure 3.18. Model representing the main behaviour of the hybrid LC filter with two auxiliary foil earthing alternatives.

The intra capacitance C_{i1} separated by the auxiliary foil cannot be considered only as a simple function of dimensions and properties of the materials used. At low frequencies, this makes it possible to neglect the intra capacitance. At higher frequencies, the system can be represented by a number of capacitive and inductive elements as it is shown in Figure 3.19 (a). Now the whole intra capacitance C_{i1} is determined by the potential differences between the turns. This means that the intra capacitance of the main foil is difficult to predict and requires special attention in the future studies. In this work, the intra capacitances are assumed constant in order to investigate the hybrid LC filter properties at external impedances close to those of real drives, and to evaluate the hybrid LC filter properties in the time domain with simulations. An example presented in Figures 3.19 (b) and (c), respectively, shows how the main capacitances of the foils C_{b1} and C_{b2} correlate with the intra capacitances that produce two different ways for a high-frequency signal: to the load (C_{i1}) and to the earth (C_{i2}).

Our studies showed that earthing of the auxiliary foil reduces the intra capacitance C_{i1} approximately to 1/15, whereas the intra capacitance C_{i2} may be assumed unchanged, and the magnetic coupling factor between the main and the auxiliary foils even with nonprofessional winding rolling obtains values in the range $c = 0.9-0.98$.

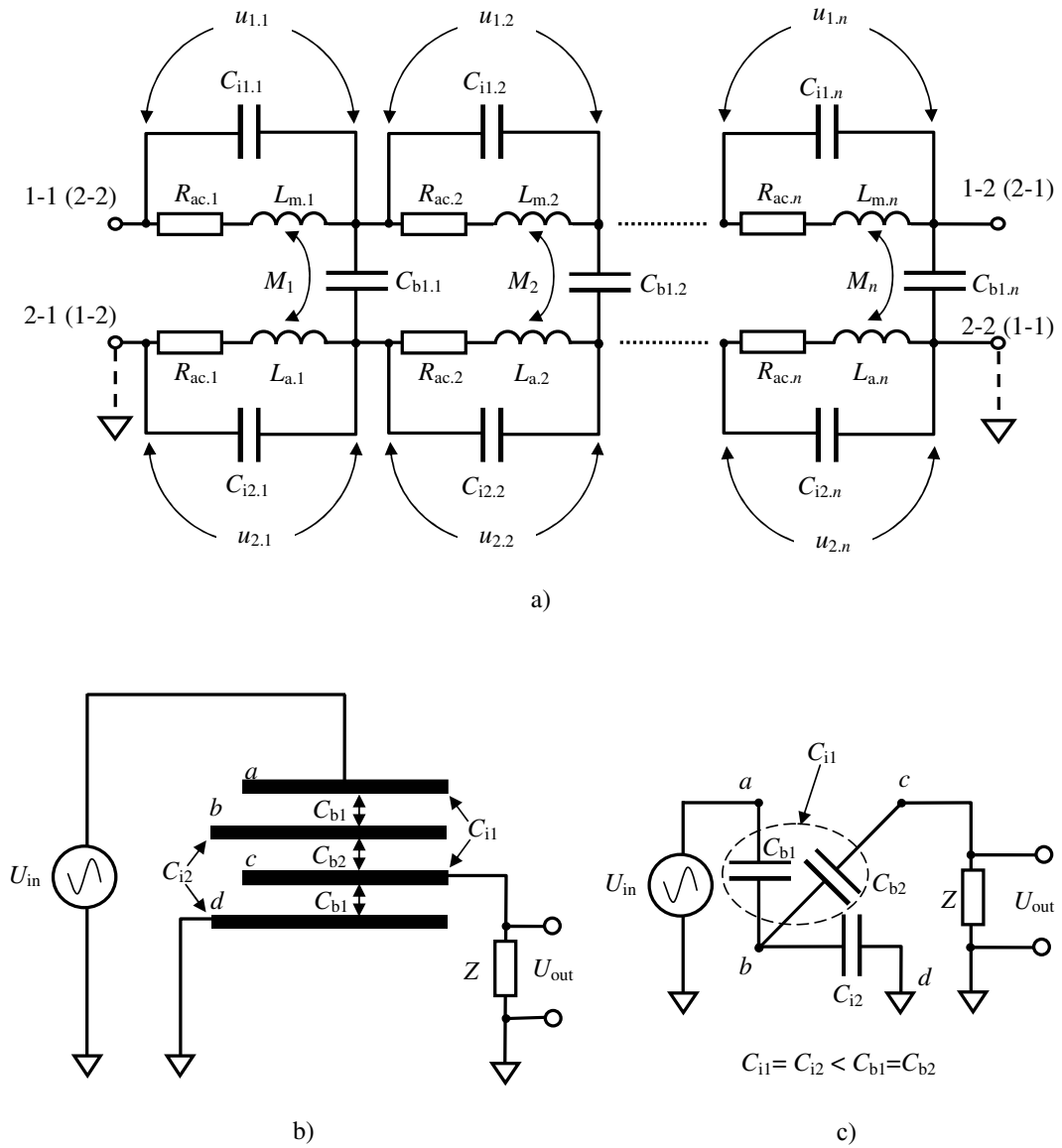


Figure 3.19. Hybrid LC filter representation at high frequencies. A part of the current travelling through such a system tends to flow via the intra capacitances. (a) Representation with distributed parameters. (b) Intra capacitances. (c) Equivalent electrical circuit showing the high-frequency signal paths through the intra capacitances of the main and auxiliary foils.

The main simulation results with different prototypes in the frequency domain are presented in Figures 3.20 and 3.21. These results show that the model presented in Figure 3.18 is adequate enough to simulate real equipment. The differences between the measured and simulated curves at frequencies above 10 MHz can be explained by the unaccounted impedances of connection wires. The simulations in the time domain are described in section 3.6.

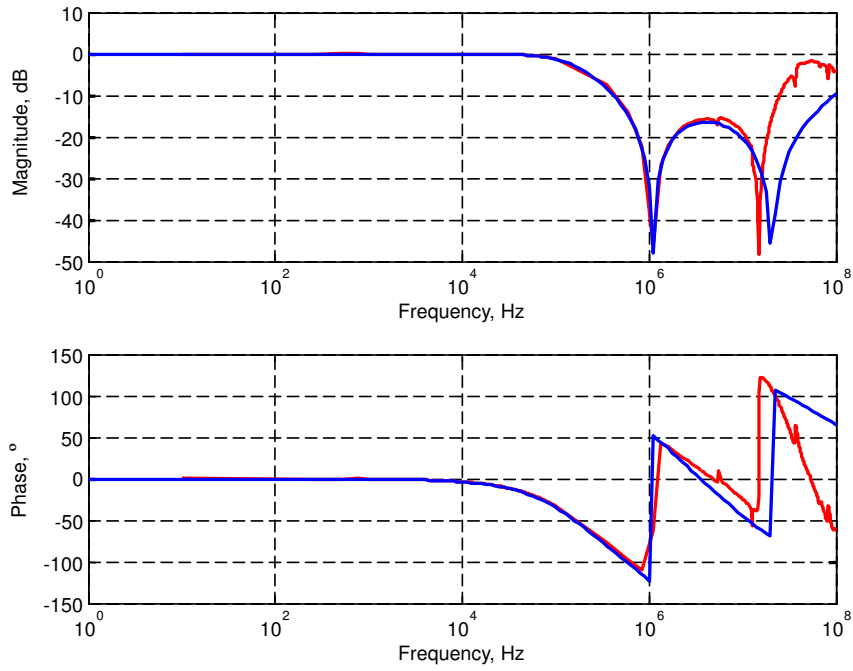


Figure 3.20. Prototype results with the main inductance $L_m = 5.3 \mu\text{H}$ and the main capacitance $C_{b1} = 38 \text{ nF}$. Measured (red curve) and simulated (blue curve): MAI 1-1 MAO 1-2 AE 2-2.

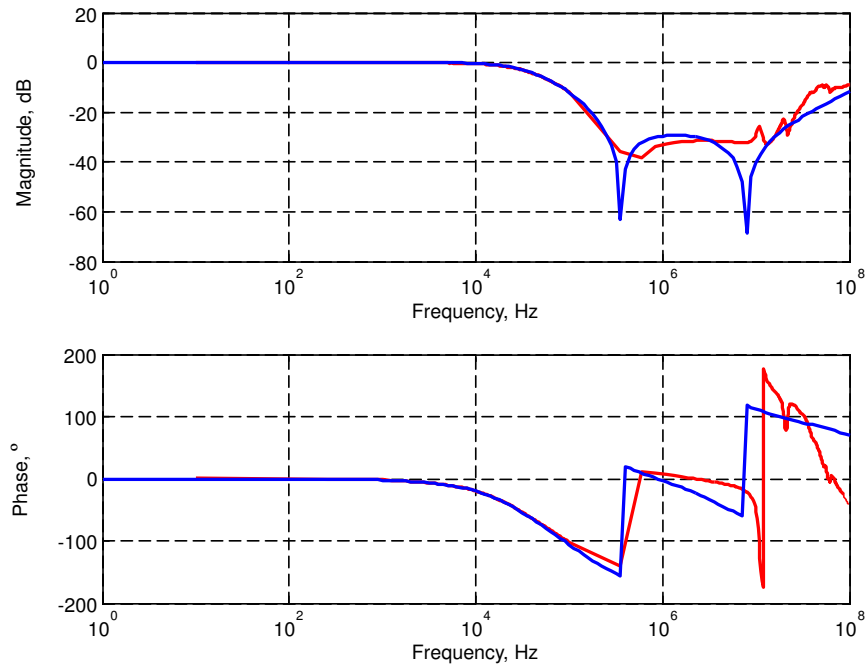


Figure 3.21. Prototype results with the main inductance $L_m = 50 \mu\text{H}$ and the main capacitance $C_{b1} = 215 \text{ nF}$. Measured (red curve) and simulated (blue curve): MAI 1-1 MAO 1-2 AE 2-2.

3.6 Hybrid LC filter simulations in the time domain

Let us now consider a hybrid LC filter used in the drive setup described further in section 4.1. The main inductance $L_m = 30 \mu\text{H}$, and the main capacitance can be selected to be either $C_{b1} = 140 \text{ nF}$ or $C_{b1} = 240 \text{ nF}$. The frequency responses of one phase of the HLCF in question are presented in Figures 3.22 and 3.23.

Mäki-Ontto (2006) describes the method which permits to simulate both differential and common modes of an electric drive simultaneously. It is, of course, advisable to do so but in this case the differential-mode noise (low-frequency phenomenon) and common-mode noise (high-frequency phenomenon) have been simulated separately. This may be justified by the fact that, normally, an electrical machine may be represented by two different circuits at low and high frequencies as it can be seen in Fig. 4.4 and (Consoli et al 1996, Boglietti and Carpaneto 1999, Doležel et al 2000, Ahola 2003). Experimental results also show good agreement with the simulation results obtained by this way.

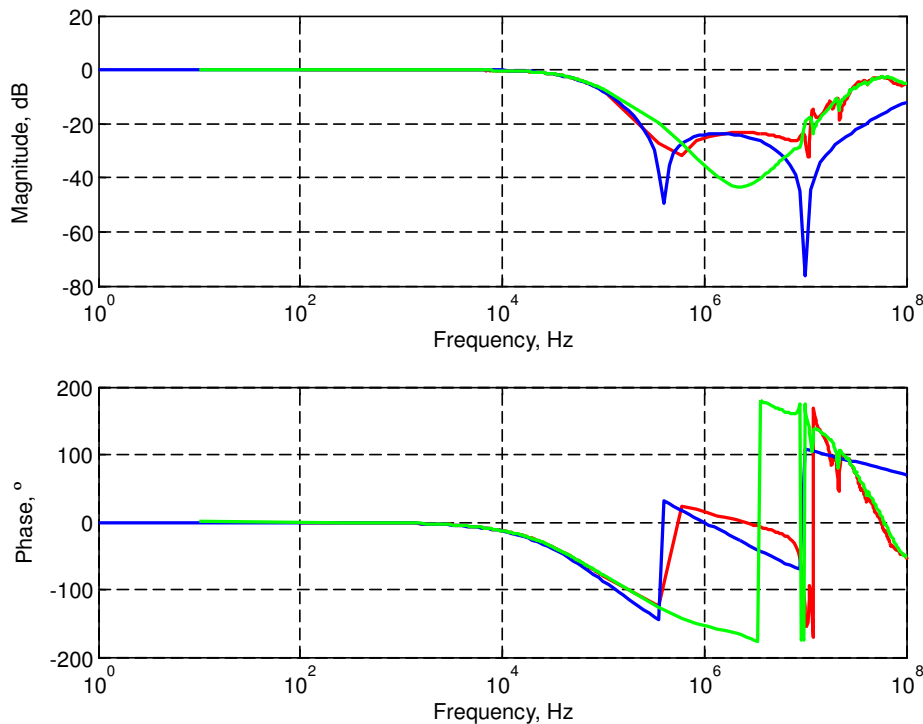


Figure 3.22. Hybrid LC filter for the drive setup (main capacitance $C_{b1}=140 \text{ nF}$). Measured (green curve): MAI 1-1 MAO 1-2 AE 2-1. Measured (red curve) and simulated (blue curve): MAI 1-1 MAO 1-2 AE 2-2.

The step response simulations for one phase are presented in Figure 3.24. During modelling, only the DC resistance of the foils ($8 \text{ m}\Omega$) was taken into account. The model contains input and output resistances similarly as in Figure 3.5. Now $R_{in} = 0.5 \Omega$, $R_{out} = 1.3 \text{ k}\Omega$ to represent the drive inverter and the motor discussed in Chapter 4. The cable is neglected.

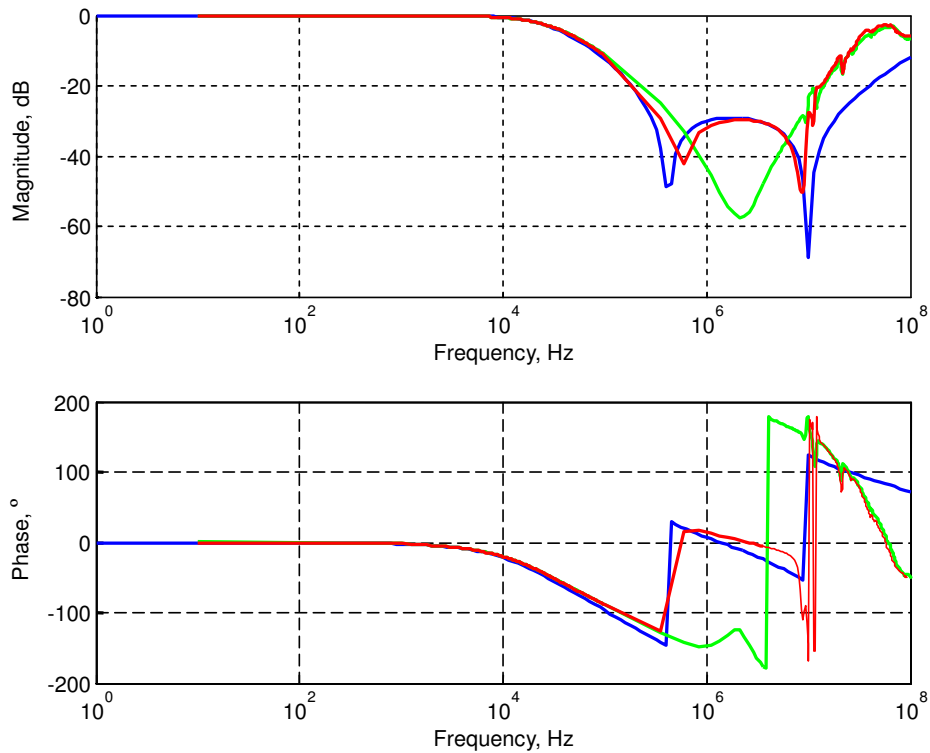


Figure 3.23. Hybrid LC filter for the drive setup (main capacitance $C_{b1}=240$ nF). Measured (green curve): MAI 1-1 MAO 1-2 AE 2-1. Measured (red curve) and simulated (blue curve): MAI 1-1 MAO 1-2 AE 2-2.

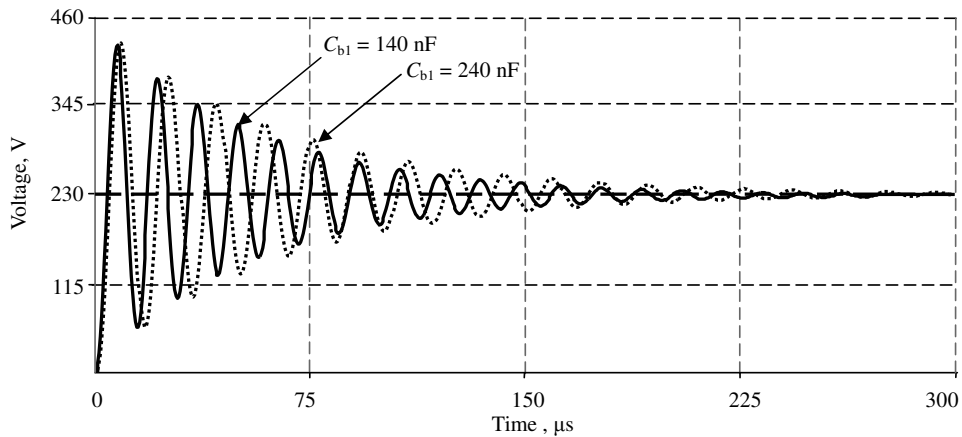


Figure 3.24. Simulated step responses (phase-to-ground voltage equivalent), MAI 1-1 MAO 1-2 AE 2-2.

Figure 3.24 shows that the step transient responses in all cases have oscillations mainly determined by the resonances between the main inductance and the main capacitance. With that, if the auxiliary foil is grounded at the output end of the main foil, the signal has a rise time equal to $3.3 \mu\text{s}$ at $C_{b1} =$

140 nF and 4.3 μ s at $C_{b1} = 240$ nF. These values are quite close to the values measured during the tests and presented in Figures 4.8–4.10.

Figure 3.25 shows the frequency responses for the chosen input and output resistances $R_{in} = 0.5 \Omega$, $R_{out} = 1.3 \text{ k}\Omega$. Both responses have resonance at frequencies defined by Eqs. (2.11) and (2.12) because the resistance R_{in} is not sufficient to damp it totally as it is with the fixed 50 Ω resistor used in the measurements with the frequency analyzer.

Common-mode simulations (discussed in more detail in Appendix A) were provided for the test setup presented in Chapter 4. The filter configuration was performed in accordance with Figure 1.18, where the common mode link is active. The simulation results showed that the common-mode current peaks without filter are 3.6 A on average. If the auxiliary foils of the HLCF are connected to neutral at the output terminal of the main foil, common-mode current peaks can be decreased to 0.8 A on average at the main capacitance $C_{b1} = 140$ nF. At the main capacitance $C_{b1} = 240$ nF, the common-mode current peaks can be reduced to 0.36 A on average. These data are quite indicative compared with the measured results presented later in section 4.3.4.

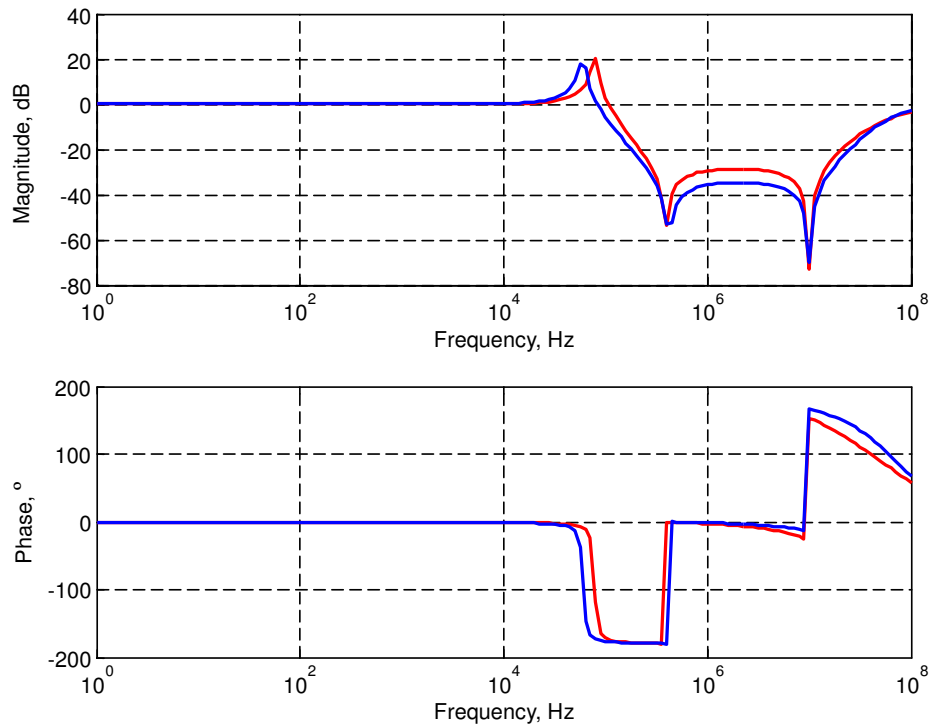


Figure 3.25. Simulated frequency responses at $R_{in} = 0.5 \Omega$, $R_{out} = 1.3 \text{ k}\Omega$, MAI 1-1 MAO 1-2 AE 2-2. Red curve: the main capacitance $C_{b1} = 140$ nF. Blue curve: the main capacitance $C_{b1} = 210$ nF.

Summary of Chapter 3

- In this chapter, two new hybrid LC filter models were proposed: a simplified model for low frequencies (below 2 MHz) and a general model for the frequency range 1 Hz–100 MHz. Both models can be used in hybrid LC filter design proposed in Chapter 2 for electrical behaviour estimations with the present-day computer facilities. The general model of the hybrid LC filter takes into account the main and mutual inductances, the main and intra capacitances of the windings as well as the AC resistance of foils. The simplified model takes into account the main inductance and main capacitance only. Adequacy of the models is verified by three prototypes.
- At low frequencies where the differential mode signal in the motor drive is dominating, an air-core hybrid LC filter can be described like a traditional LC filter, which is used in drive applications to decrease the du/dt of PWM voltages. At high frequencies where the common-mode current is dominating, the attenuation level becomes lower because of the stray and inserted impedances. Nevertheless, the filter still provides good attenuation.
- According to the measurements in the frequency domain, the best attenuation at high frequencies can be reached when one of the ends of the auxiliary foil is earthed. The shape of the Bode plot depends on the end at which the foil is earthed. If the hybrid LC filter is earthed at the outermost or the innermost hidden turn, the Bode plot has a smooth shape. If the hybrid LC filter is earthed at the outermost or the innermost exposed turn, the Bode plot has resonances.
- The current redistribution at high frequencies differs for different foil earthing alternatives because of different common fluxes produced by the coils. If the earthed turn of the auxiliary foil corresponds to the input turn of the main foil, the fluxes produced in the coils cancel each other, and the current redistribution effect from centre to the edges of the foils decreases. On the contrary, if the earthed turn of the auxiliary foil corresponds to the output turn of the main foil, the fluxes produced in the coils strengthen each other and the current redistribution effect increases. Thus, the first case may be characterized by better attenuation of resonances at intermediate frequencies.
- The simulations of the hybrid LC filter in the time domain with the proposed general model showed that the transient responses have significant oscillations as it is expected for a circuit containing reactive components and characterized by a high quality factor. The model indicates that the hybrid LC filter can significantly reduce the rise rates of PWM pulses as well as the common-mode current inside the drive.

4 Experimental investigations of the hybrid LC filter

4.1 Drive setup description

The experimental investigations were performed at Lappeenranta University of Technology (LUT) in the Laboratory of Electrical Motors and Drives. The drive setup is presented in Figure 4.1. The test squirrel cage induction motor was supplied by a two-level voltage source ABB SAMI GS IGBT frequency converter, which was supplied from the grid. Between the converter and the motor cable there was the hybrid LC filter studied in this work. The drive setup is presented in Figure 4.2. Table 4.1 gives the parameters of the test setup.

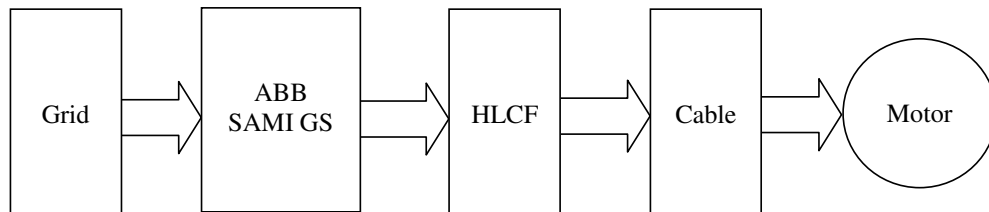


Figure 4.1. Basic structure of the drive setup.

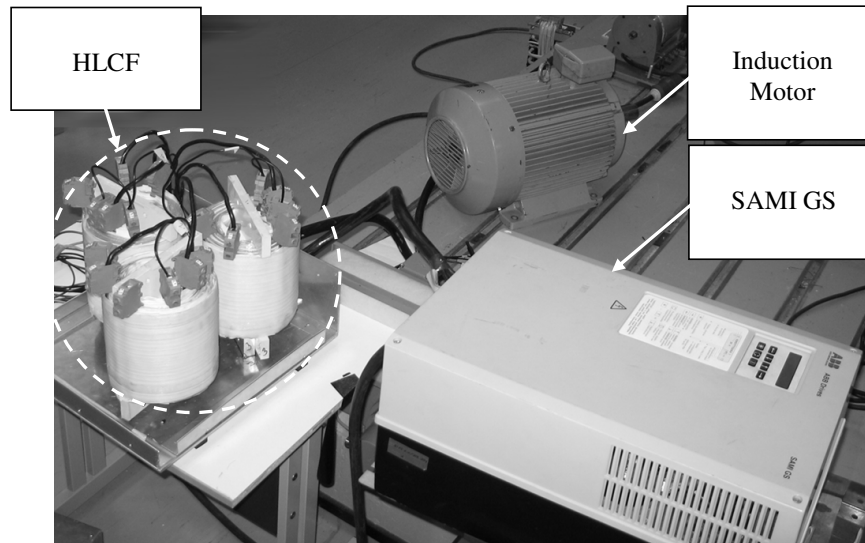


Figure 4.2. Main parts of the drive setup in the laboratory. HLCF: the hybrid LC filter.

All the tests were carried out in the motor no-load mode, which (applying to the phenomena under consideration) describes adequately the situation with loaded drives. According to subsection 1.2.3,

reflections do not depend on the load but the motor and cable characteristics. On the other hand, the common-mode current flows through all the cable wires simultaneously and then divides into different paths according to their impedances. If the load impedance is quite high, for example, if special protection measures are undertaken, the current will flow through the same paths as it flows without a load.

During the tests, voltages at the motor and inverter terminals were measured with a Yokogawa PZ4000 scope with a maximum 5MS/s resolution up to 2 MHz (Yokogawa 2000). The physical design of the hybrid LC filter is illustrated in Figure 4.3.

Table 4.1. Description of the test drive components.

Test setup element	Description
Motor	<p>Strömberg, three-phase induction motor, IEC 180L48.</p> <p>Nominal frequency 50Hz, nominal power 22kW, delta-connected phase windings, nominal voltage 380V, nominal current 43A, rated speed 1460 rpm, number of poles 4, power factor 0.86, mass 178 kg.</p> <p>The measured differential- and common-mode impedances are given in Figure 4.4.</p>
Cable	<p>Pirelli, MCCMK 3x35/16 AN 1kV (Prysmian 2006). Length 200 m, screened, three and a half conductor (three phases + protective earth). Phase DC resistance at 20 °C is 0.524 Ω/km, phase AC resistance 0.63 Ω/km, phase inductance 0.26 mH/km, operating capacitance 0.55 μF/km. The characteristic cable impedance calculated by Eq. (1.4) $Z_c = 21.7 \Omega$.</p>
Hybrid LC filter, HLCF (see Figure 4.3)	<p>Three-phase, each phase contains one column. Every column contains three foils: inductance of layer per phase 30 μH, measured capacitance between foil 1 and foil 2 (see Figure 4.3 (c)) per phase 240 nF, measured capacitance between foil 2 and foil 3 per phase 180 nF, measured capacitance between foil 1 and foil 3 140 nF.⁵ All foils made of aluminium. Thickness of foil 2 is 0.2 mm, thickness of foils 1 and 3 is 0.1 mm. Insulator type: Nomex T418, thickness 0.25 mm. Core-type: round glass-fibre tube. Dimensions of one column: height 150 mm, outer diameter 180 mm, inner diameter 100 mm. Inner ends of foils are denoted by 1 (1.1, 2.1, 3.1), while outer ends of foils are denoted by 2 (1.2, 2.2, 3.2). Frequency responses measured with the HP4194a analyzer presented in Figures 3.22 and 3.23. Only two foils were used in the practical tests (because of restrictions by the capacitance in the drive).</p> <p>Rated voltage 400V AC, rated current 50A AC.</p>
SAMI GS frequency converter (ABB 1995)	<p>Type: ACS 501-041-3-00P20.</p> <p>Two-level voltage source frequency converter, supply voltage: three-phase 380V/400V/415V, IGBT average switching frequency 3 kHz. Frequency used in tests was 2.14 kHz.</p>
Grid	Three-phase, 400V.

⁵ Manufacturer did not succeed in maintaining tight and uniform rolling, which may be the main reason for differences between capacitances.

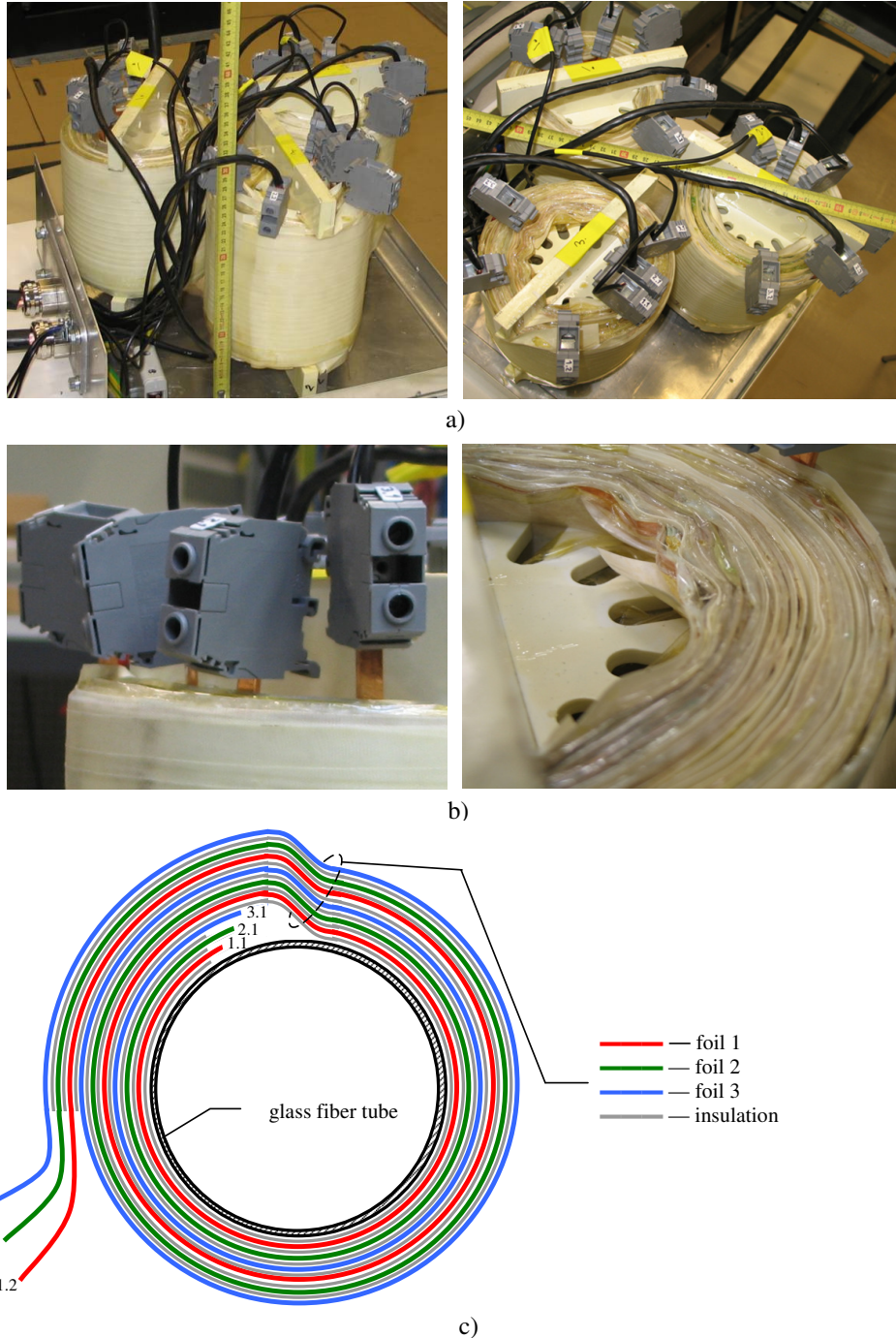


Figure 4.3. Hybrid LC filter used in the test setup: (a) General view of the three-phase HLCF. (b) Connection wires and the structure of one column. (c) Main configuration.

As it was discussed in Chapter 1, the hybrid LC filter has two tasks in the motor drive circuit: to work as an effective du/dt filter and as a common-mode filter. The HLCF was tested for both of these purposes, and the results are reported in the following.

First, the differential-mode and the common-mode impedances of the three-phase, 22 kW induction motor used in the test setup were measured. Figure 4.4 is in accordance with (Consoli et al 1996, Rendusara and Enjeti 1998, Boglietti and Carpaneto 1999, Ahola 2003, Weens et al. 2005). Motor phases are delta connected and three terminals are accessible from outside. The differential-mode impedance was measured between two phase terminals connected together and the third phase terminal. The common-mode impedance was measured between all phases combined together and non-earthed motor frame.

The motor differential-mode impedance starts on the inductive side. At 100 Hz the impedance is 2.8 Ω and increases as the frequency increases. In the range of about 80–90 kHz, the impedance changes to the capacitive side. After that, between 5 MHz and 6 MHz the impedance phase angle changes from the capacitive side to the inductive side.

The common-mode impedance at 100 Hz starts at 130 k Ω and decreases as the frequency increases. This is explained by the influence of the internal motor capacitances discussed in Chapter 1. The phase angle remains on the capacitive side up to about 2 MHz. At 100 kHz, the impedance has reduced to about 100 Ω , and the phase is almost zero after 100 kHz, but drops back close to -90 degrees at higher frequencies up to 2 MHz, where the impedance is 2.8 Ω , and the phase angle shifts to the inductive side at frequencies above 2 MHz. As the common-mode impedance is rather low at the whole range observed, it is easy to understand that common-mode currents can be high if large common-mode voltages are supplied to the motor as it was discussed in subsection 1.2.4.

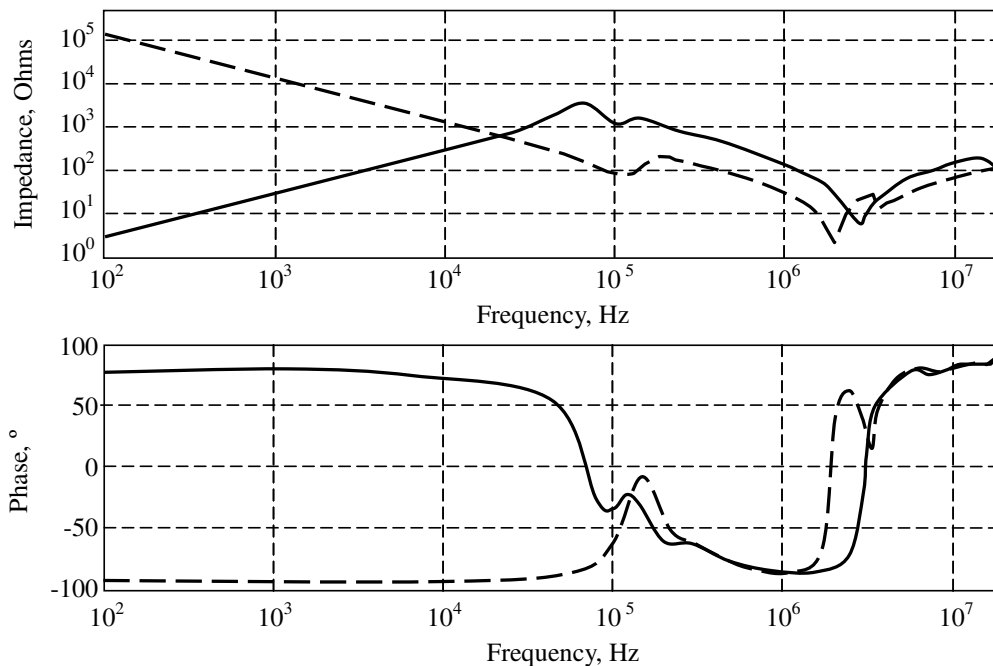


Figure 4.4. Differential-mode (solid lines) and common-mode (dashed lines), impedances of the Strömberg three-phase, 22 kW induction motor used in the test setup.

4.2 Background for the analysis of the step response

Before analysing the experimental results, let us consider some of the basic definitions used in the literature to examine the behaviour of the step response.

A system reaction to a step signal (Figure 4.5) can be described by a set of parameters (Dorf and Bishop 1998). Let us consider this terminology with respect to the question under consideration. The most important parameters characterizing PWM signals arriving at motor windings are the rise time t_r , the signal overshoot σ , the peak voltage U_m and the signal rise rate du/dt . The rise time t_r is related to the frequency of the signal across the first coils of an electrical machine winding, which may cause a failure of insulation (von Jouanne et al. 1998, Finlayson 1998, Kaufold et al. 2000) as well as a failure of bearings (Ollila et al. 1997). In overdamped circuits where there is almost no overshoot, the rise time t_{r1} is measured as the time during which the output signal changes from 10 % to 90 % of a required level of the voltage U_{req} . This required level may be measured at the inverter outputs. The peak voltage U_m and the signal overshoot $\sigma = (U_m/U_{req}) \cdot 100\%$ characterize a maximum voltage stress on a motor winding caused by the incoming signal. The rate du/dt describes how fast PWM voltage pulses injected to motor phases rise, and it is measured in the linear zone as it is shown in Figure 4.5.

Other important parameters that may be taken into account during the analysis are the time instant t_m at which the maximum overshoot takes place, the number of significant oscillations (four in Figure 4.5), the period of oscillations T_o , which gives approximate information about the lowest resonance frequency and the transient response time T_s that can be found when the oscillations are negligible, that is, they lie within a determined zone e_s .

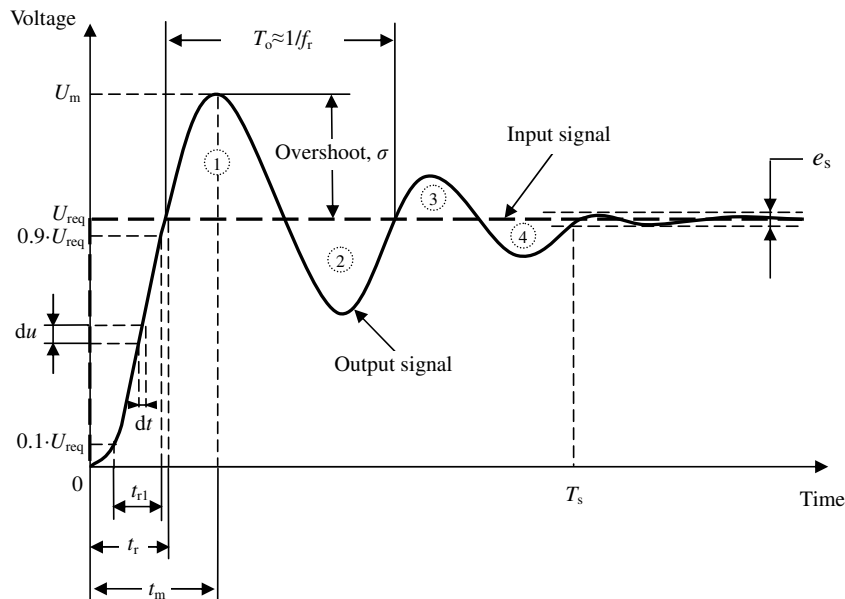


Figure 4.5. System reaction to a step signal and the main parameters that characterize this reaction.

It was discussed in subsection 1.2.3 that the motor impedance is usually notably higher than the characteristic impedance of the cable. In the case of an inverter-fed electrical drive, a pulse travelling from the cable to the motor terminal causes a reflection. The ratio of the reflected pulse and the incident pulse is expressed by the reflection coefficient defined by Eq. (1.6). If an LC filter without a resistor bank is used to decrease the signal rise speed, oscillations can also be expected.

4.3 Test results

In order to further simplify the presentation of the results obtained with the hybrid LC filter, let us apply the following terminology:

- MI for the inverter-connected terminal of the main foil,
- MC for the cable-connected terminal of the main foil,
- AP for the star-point-connected terminal of the auxiliary foil,
- ISP for the junction of the auxiliary foils in star at inverter-connected terminals of the main foils,
- CSP for the junction of the auxiliary foils in star at cable-connected terminals of the main foils.

From now on, we apply the foil end numbering according to Figure 4.3 (c).

4.3.1 System without a filter

First, let us observe the motor terminal voltages when there is no filter between the inverter terminals, the cable and the motor terminals. Measured results are given in Figure 4.6.

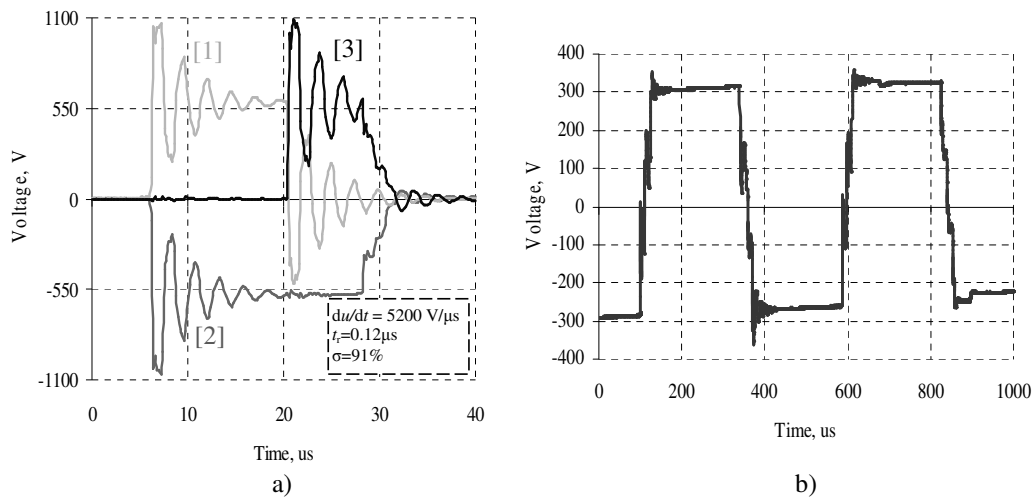


Figure 4.6. Voltages at the motor terminals without a filter on the 200 m cable. (a) Line-to-line voltages at the motor terminals ([1] between phases A and B, [2] between phases B and C, [3] between phases C and A). (b) Calculated common-mode voltage.

The voltage overshoot is more than 91 % at the rise time of about 0.12 μs and the du/dt value is 5200 $\text{V}/\mu\text{s}$. According to Gambica (2006), for a 200 m cable and motors with a 415 V three-phase

rated AC voltage, overvoltages above 1 kV and pulse rise times less than 1.2 μs may be dangerous for a motor insulation and have to be decreased with additional means, such as du/dt filters.

Because the stator windings of the motor used in the tests are delta connected, the simplest way to obtain the common-mode voltage is to measure the phase-to-earth voltages and then to use Eq. (1.1). The results of these calculations are presented in Figure 4.6 (b) and they show that common-mode voltage has amplitude of about 300 V and quite steep edges. Therefore, the high-frequency harmonic content of the common-mode voltage is quite high.

4.3.2 Hybrid LC filter in the choke mode

Let us consider the hybrid LC filter only in a choke mode reducing the du/dt , in other words, when only one of the three foils is used and the other two have no galvanic connections. The results are presented in Figure 4.7, and they show that the motor drive system becomes more oscillating compared with the situation of no filter at all, but the pulse rise time increases considerably. This is an expected result of an increase in the value of the series inductance, which interacts with the cable capacitance reducing the system resonance frequency. However, in line with Eq. (2.17), the increasing Q -factor of the system may lead to larger overshoots. It may also be stated that the system at different connections of foils demonstrates a very similar behaviour, increasing the rise time of pulses by a factor of 10 (from 0.12 μs to 1.2 μs) and decreasing the du/dt rate by a factor of 12.7 (from 5200 V/ μs to 410 V/ μs) compared with the case without filtering. The results also show that the air-cored inductor is a low-loss one and does not effectively damp the oscillations. With that, the intra capacitances of the HLCF windings are not degrading its ability to reduce the du/dt values at the motor terminals.

4.3.3 Hybrid LC filter in the du/dt filter mode

This subsection considers the influence of a hybrid LC filter when internal main capacitances are used but the common-mode link is not activated.

Let us consider the results obtained with the HLCF placed between the inverter and the cable. The main foil is foil 1 and the auxiliary is foil 3. Foil 2 is not used. The tests were performed for different alternatives of auxiliary foil connections in star. Figures 4.8 and 4.9 allow to conclude that with the ISP configuration the pulse rise times as well as the time periods of oscillations and the numbers of oscillations are less than with the CSP configuration.

The reason for this behaviour can be explained by the distributed nature of the hybrid LC filter as described in Chapter 3 (Figure 3.19 (a)). In the ISP configuration currents tend to flow through the first turns of the filter causing a high stress at these turns, so that some problems with reliability may be expected. Otherwise, in the CSP configuration currents have to flow through all the turns of the auxiliary foils, and hence, the capacitive couplings between the foils are used more effectively. These data also correlate with the time-domain simulations presented in section 3.6. Because the resistance in the HLCF and the cable circuit is relatively small, the Q -factor in both cases obtains high values and the overshoots at the motor terminals approach their theoretical maximum, that is, the doubled voltage value of the inverter voltage pulse (von Jouanne et al. 1998, Finlayson 1998). Then, because of the internal resistive losses of the filter and the cable, the oscillations fade out (in other cases auto-oscillations of the doubled inverter voltage amplitude could occur).

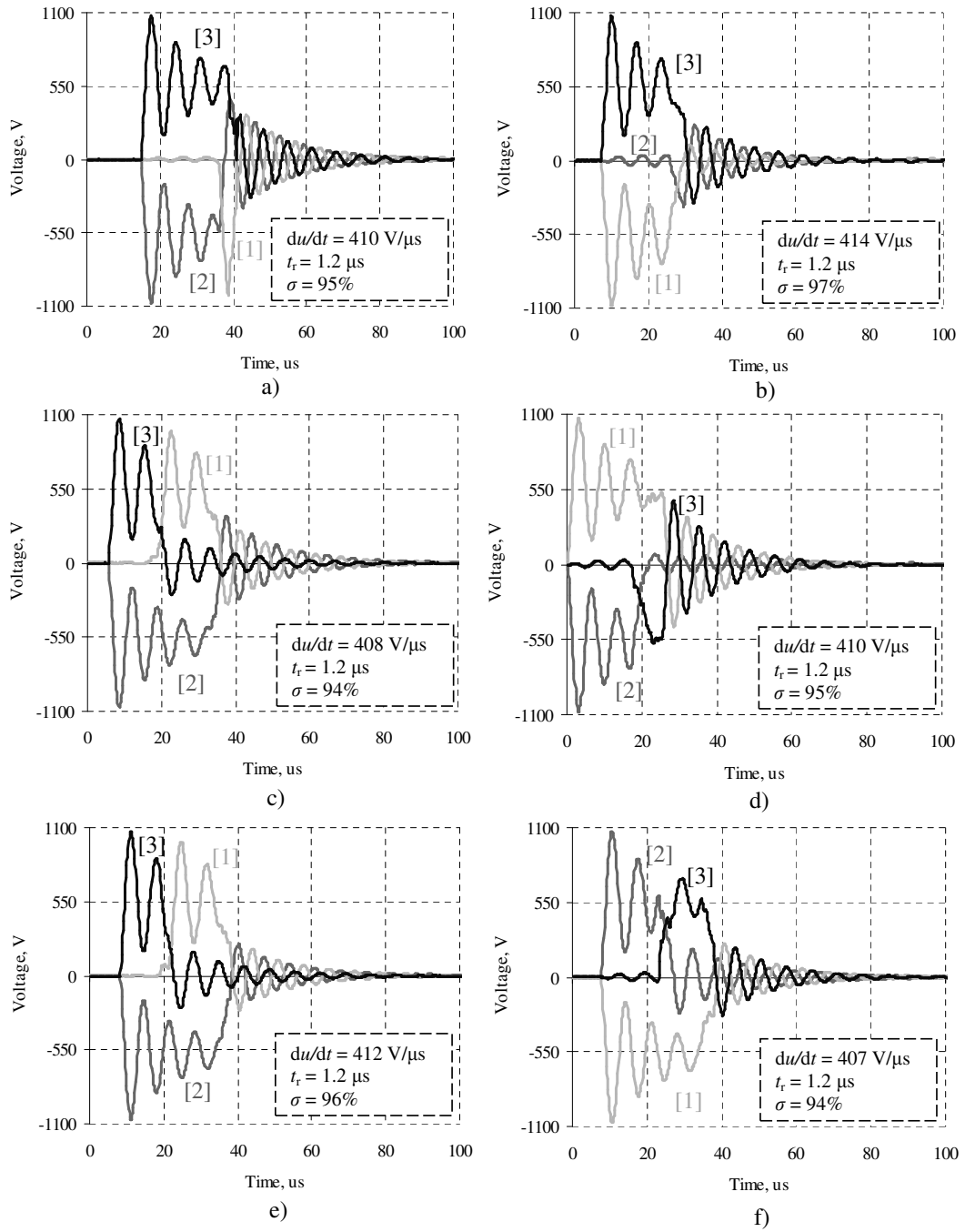


Figure 4.7. Line-to-line voltages with the HLCF in the choke mode ([1] between phases A and B, [2] between phases B and C, [3] between phases C and A). (a) MI 1.1 MC 1.2. (b) MI 1.2 MC 1.1. (c) MI 2.1 MC 2.2. (d) MI 2.2 MC 2.1. (e) MI 3.1 MC 3.2. (f) MI 3.2 MC 3.1.

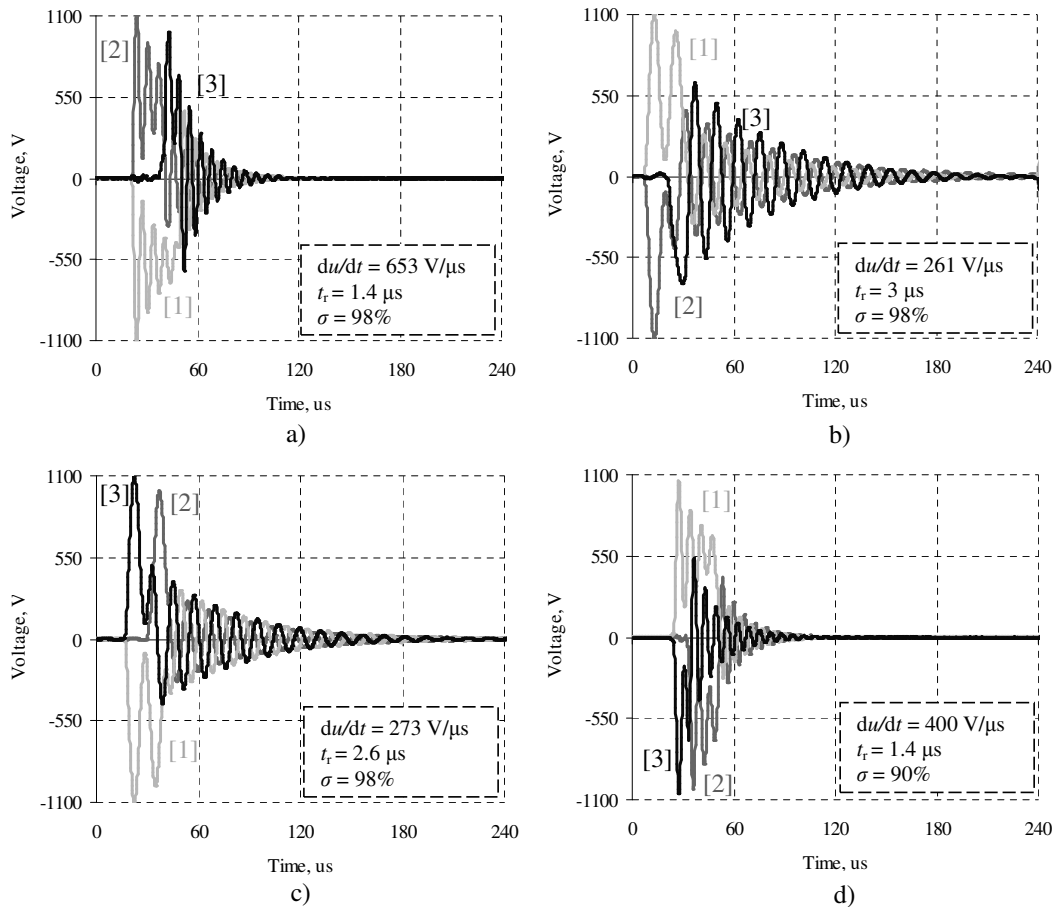


Figure 4.8. Line-to-line voltages with the HLCF in the du/dt mode ([1] between phases A and B, [2] between phases B and C, [3] between phases C and A). (a) ISP: MI 1.1 MC 1.2 AP 3.1. (b) CSP: MI 1.1 MC 1.2 AP 3.2. (c) CSP: MI 1.2 MC 1.1 AP 3.1. (d) ISP: MI 1.2 MC 1.1 AP 3.2.

Implementation of the CSP configuration permitted to increase the pulse rise times by a factor of 25 (from $0.12 \mu\text{s}$ to $3 \mu\text{s}$) and to decrease the du/dt rate by a factor of 20 (from $5200 \text{ V}/\mu\text{s}$ to $260 \text{ V}/\mu\text{s}$) compared with the case without filtering.

The results with an increased main capacitance (foil 3 was replaced by foil 2) are presented in Figure 4.10. In principle, they allow the same outcomes as for Figures 4.8 and 4.9. Implementation of the CSP configuration allows to increase the pulse rise time by a factor of 29 (from $0.12 \mu\text{s}$ to $3.5 \mu\text{s}$) and to decrease the du/dt rate by a factor of 25 (from $5200 \text{ V}/\mu\text{s}$ to $209 \text{ V}/\mu\text{s}$) compared with the case without filtering.

In fact, the filtered curves for the CSP configuration satisfy the IEC 60034-17 and NEMA MG Part 31 standards for motors supplied by a $400\text{V}/415\text{V}$ network.

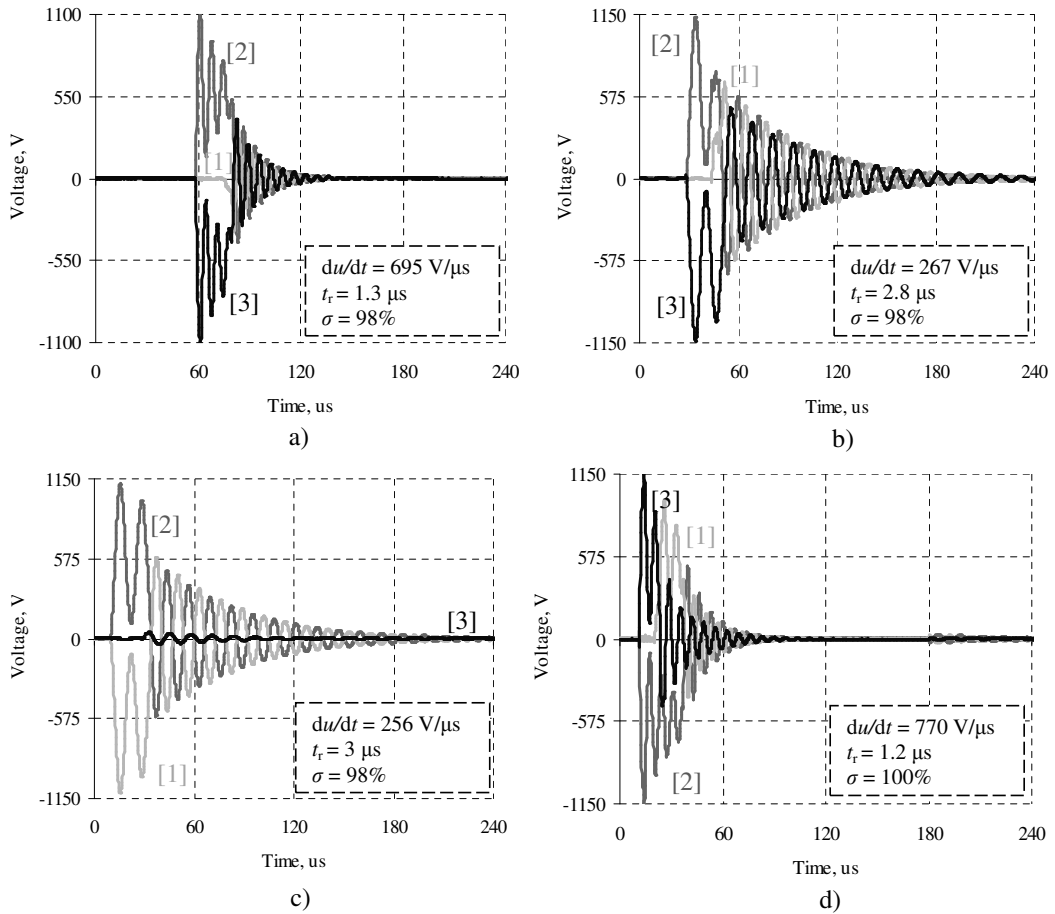


Figure 4.9. Line-to-line voltages with the HLCF in the du/dt mode ([1] between phases A and B, [2] between phases B and C, [3] between phases C and A). (a) ISP: MI 3.1 MC 3.2 AP 1.1. (b) CSP: MI 3.1 MC 3.2 AP 1.2. (c) CSP: MI 3.2 MC 3.1 AP 1.1. (d) ISP: MI 3.2 MC 3.1 AP 1.2.

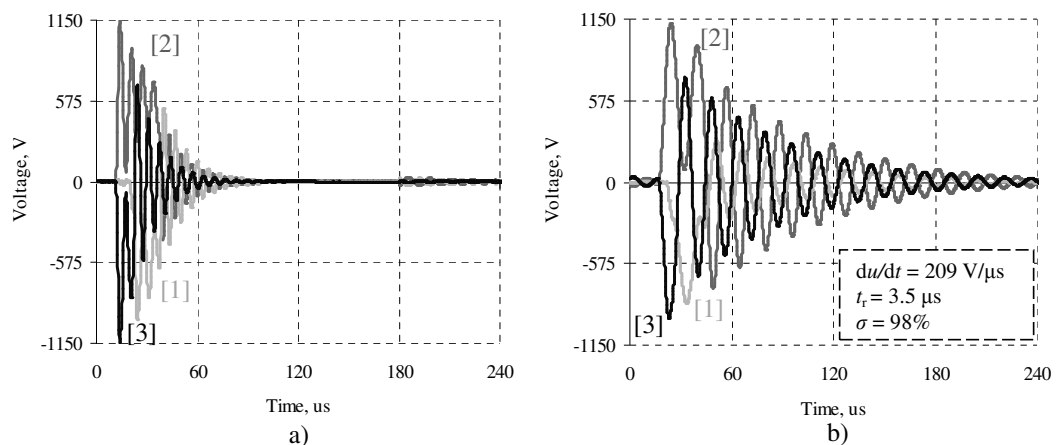


Figure 4.10. Line-to-line voltages with the HLCF in the du/dt mode at doubled main capacitance ([1] between phases A and B, [2] between phases B and C, [3] between phases C and A). (a) ISP: MI 1.1 MC 1.2 AP 2.1. (b) CSP: MI 1.1 MC 1.2 AP 2.2.

4.3.4 Hybrid LC filter in the du/dt filter mode with a common-mode link

It was mentioned in section 1.5 that common-mode noise can be effectively reduced with a link between the capacitor star point of the filter and the inverter DC link midpoint (Figure 1.18). This subsection discusses the applicability of the theory to hybrid LC filters. Common-mode link is implemented between the filter auxiliary foils star point and the inverter DC link midpoint.

Generally speaking, a hybrid LC filter demonstrates behaviour similar to filters consisting of separate components (Rendusara and Enjeti 1998). The voltage shapes are close to those presented in the previous subsections. The results for common-mode currents are presented in Figures 4.11, 4.12 and Table 4.2.

Table 4.2. Common-mode current with a hybrid LC filter as shown in Figure 1.18.

	Peak current without HLCF, A	With HLCF, without common-mode link		With HLCF, with common-mode link	
		Peak current, A	Maximal peaks attenuation, dB	Peak current, A	Maximal peaks attenuation, dB
ISP: MI 1.1 MC 1.2 AP 3.1 (Figure 4.11 (a))	5.7	1.5	11.6	0.5	21.7
CSP: MI 1.1 MC 1.2 AP 3.2 (Figure 4.11 (b))		1.8	9.8	0.5	21.9
CSP: MI 1.2 MC 1.1 AP 3.1		1.9	9.5	0.5	20.5
ISP: MI 1.2 MC 1.1 AP 3.2		1.5	12	1	15
ISP: MI 3.1 MC 3.2 AP 1.1		1.1	14.6	0.7	17.7
CSP: MI 3.1 MC 3.2 AP 1.2		1.6	10.8	0.5	20.5
CSP: MI 3.2 MC 3.1 AP 1.1		2.3	7.8	0.6	19.3
ISP: MI 3.2 MC 3.1 AP 1.2		1	15.1	0.8	17.2
ISP: MI 1.1 MC 1.2 AP 2.1 (Figure 4.12 (a))		1.3	12.5	No data	
CSP: MI 1.1 MC 1.2 AP 2.2 (Figure 4.12 (b))		1.9	9.4		

Figure 4.11 shows the common-mode currents at the motor terminals for the case when main is foil 1 and the auxiliary is foil 3. The noise without a common-mode link does not depend essentially on the terminal of the main foil next to which the auxiliary foils are combined in star. Moreover, in contrast with subsection 4.3.3, worse results are now obtained with the CSP configuration. Remembering that the common-mode signal is a high-frequency phenomenon, this can be explained with the intra capacitance (see section 3.5), which lets the current flow through the main foil if no extra means are provided.

The auxiliary foil connection to the common-mode link reduces the main foil intra capacitance by equalizing the potentials of the star point of the auxiliary foil capacitors and the DC link midpoint. Better attenuations were obtained by using the CSP configuration.

When foils 1 and 2 are used as the main and auxiliary foils, the capacitance between the foils is approximately doubled compared with the case where foils 1 and 3 are used as the main and auxiliary foils. The use of a common-mode link at such capacitance between the main and auxiliary foils in the test setup became impossible because of the earth fault indications of the inverter. Nevertheless, the phenomena that can be observed without a common-mode link are similar to Figure 4.11 but with better attenuation. The results are illustrated in Figure 4.12.

The data show that the common-mode link between the star point of the HLCF and the DC link midpoint is useful if common-mode problems in the drive are expected; further, a common-mode link may be recommended as a useful solution even if a hybrid LC filter is needed mainly as a du/dt filter.

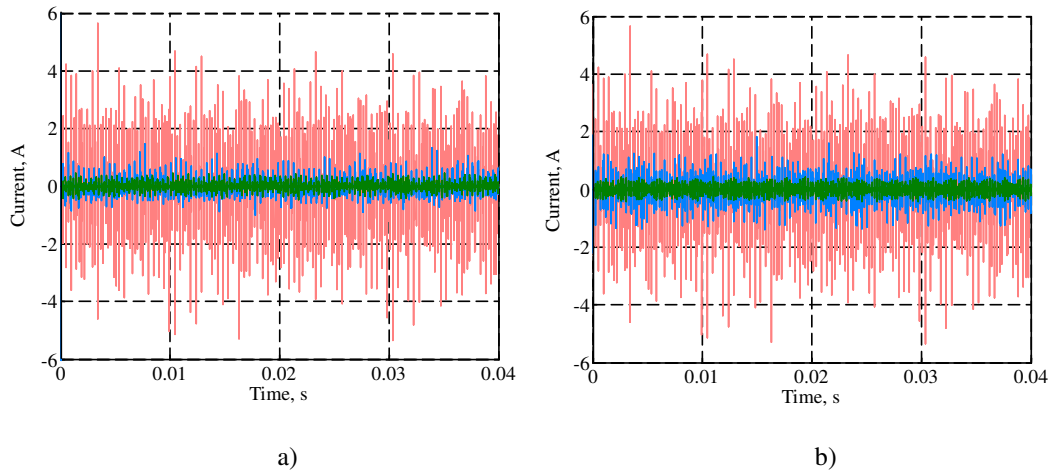


Figure 4.11. Common-mode current: (red – no HLCF, blue – with the HLCF without a common-mode link, green – with the HLCF with a common-mode link). (a) ISP: MI 1.1 MC 1.2 AP 3.1. (b) CSP: MI 1.1 MC 1.2 AP 3.2.

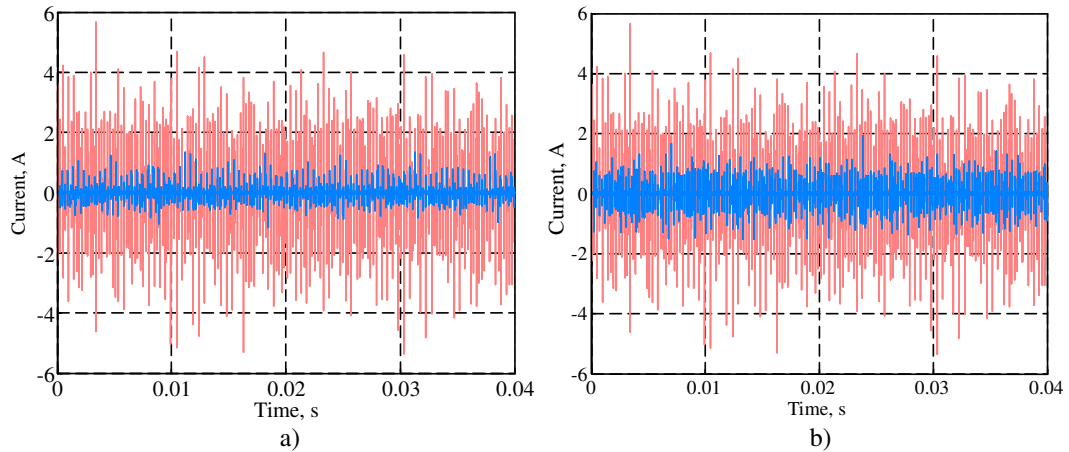


Figure 4.12. Common-mode current with large capacitance (foils 1 and 2 used): (red – no HLCF, blue – with the HLCF without a common-mode link). (a) ISP: MI 1.1 MC 1.2 AP 2.1. (b) CSP: MI 1.1 MC 1.2 AP 2.2.

4.3.5 Hybrid LC filter with additional resistances

The previous subsections show that a hybrid LC filter (similarly with a conventional LC filter) can satisfy the requirements if there are no restrictions by the overshoot level and the number of oscillations. In other cases, some resistive losses are needed as it was discussed in section 2.3. An

attractive solution would be to utilize the skin and proximity effects in the foils to increase the internal high-frequency resistance of the HLCF. This could probably provide low losses and less heating compared with a case with separate resistors, but the increase in the internal high-frequency resistance is not sufficient to provide adequate damping of overshoots. Future investigations in this area may be recommended. Some magnetic circuit losses could also be considered as a source of extra damping.

In the following we consider the behaviour of the HLCF with resistors. To this end, $100\ \Omega$ resistors were added to the capacitive branches of every phase of the HLCF. The results presented in Figures 4.13 and 4.14 show that the resistors decrease the number of oscillations as well as the pulse rise rate and the common-mode noise, but the transient responses still have acceptable shapes close to the requirements in the standards, and the attenuation of the common-mode signal is quite good.

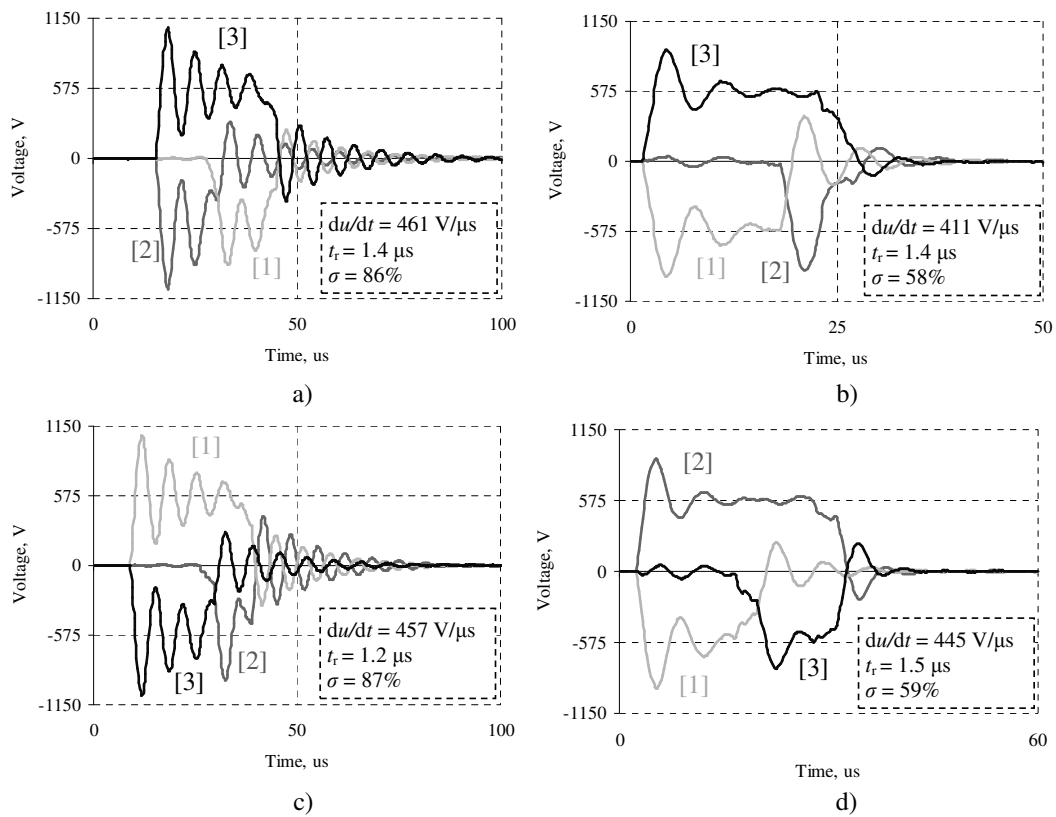


Figure 4.13. Line voltages with $100\ \Omega$ resistances in series with the main capacitances of the HLCF ([1] between phases A and B, [2] between phases B and C, [3] between phases C and A). No common-mode link: (a) ISP: MI 1.1 MC 1.2 AP 3.1, (b) CSP: MI 1.1 MC 1.2 AP 3.2. With a common-mode link: (c) ISP: MI 1.1 MC 1.2 AP 3.1, (d) CSP: MI 1.1 MC 1.2 AP 3.2.

Similarly as in the cases without an additional resistor, the system behaviour with the CSP configuration is more similar to the traditional LC filters and gives overshoots decreasing by a factor of 1.5 in all considered cases (60 % with the CSP configuration versus 90 % with the ISP configuration). With that the rise rates for all the considered cases remain almost the same.

If a common-mode link is used, the pulse shapes will not change considerably. With that, with the ISP configuration the common-mode link has practically no significance at all (Figure 4.14 (a)). Vice versa, with the CSP configuration the common-mode link provides a better noise damping (Figure 4.14 (b)) so that the maximal peaks attenuation increases from 13.5 dB to 15.6 dB (about 27 % more).

Thus, it may be recommended again to use the CSP configuration with the star-point connected to the DC link midpoint. With that, inserting resistances in the auxiliary foil circuit reduced the common-mode noise attenuation by 6 dB from 21.7 dB to 15.6 dB.

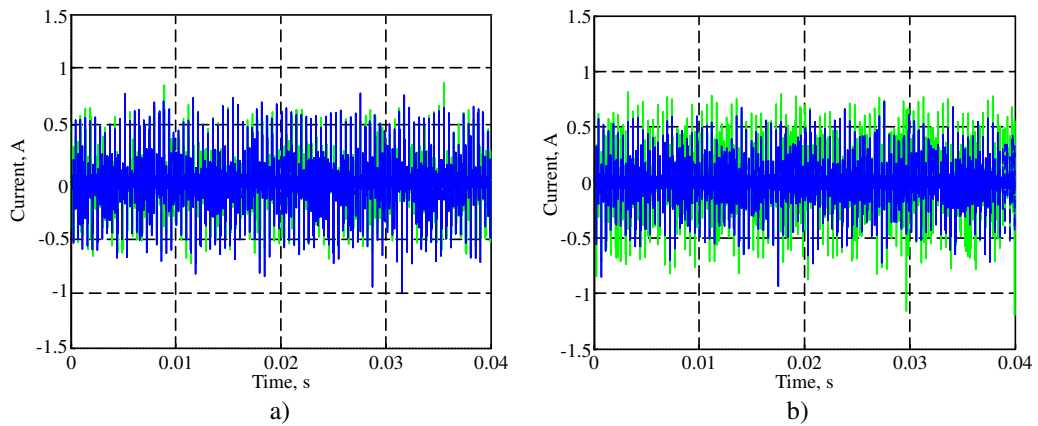


Figure 4.14. Common-mode current with $100\ \Omega$ resistances in series with the main capacitances using the common-mode link: (a) ISP: MI 1.1 MC 1.2 AP 3.1; (b) CSP: MI 1.1 MC 1.2 AP 3.2. Green curves – no common-mode link; blue curves – with common-mode link.

Summary of Chapter 4

- The investigations showed that the experimental squirrel cage induction motor drive test setup with a 200 m cable does not satisfy the standard requirements because of the excessively short pulse rise time, 0.2 μs , and too large a du/dt rate, 5200 V/ μs , unless some actions are taken to eliminate these issues. The voltage overshoot is high, about 90 %.
- A hybrid LC filter makes it possible to improve the pulse shapes so that they satisfy the IEC 60034-17 and NEMA MG Part 31 standards. The activation of the auxiliary foils increased the pulse rise time by a factor of 25 (from 0.12 μs to 3 μs) and decreased the du/dt rate by a factor of 25 also (from 5200 V/ μs to 209 V/ μs) compared with the case without filtering.
- A galvanic connection between the hybrid LC filter star point and the frequency converter DC link midpoint essentially decreased the common-mode noise with minimal attenuation up to 22 dB.
- Because of the internal resistance in the circuit (hybrid LC filter – cable) is very low, the voltages at the motor terminals oscillate heavily and have almost double voltage overshoots. Introduction of 100 Ω resistors in the best case reduced the overshoots by a factor of 1.7 (from 98 % to 58 %), but the pulse rise times decreased twice from 3 μs to 1.5 μs , while the du/dt rate increased from 256 V/ μs to 411 V/ μs (60 %) compared with the best case without resistors.
- Inserting resistors decreased the common-mode attenuation from 21.7 dB to 15.6 dB.
- According to the tests, it may be recommended to use a galvanic connection of those auxiliary foil terminals which correspond to the cable-connected terminals of the main foils. It also seems to make no notable difference which foil – inner or outer – is used as the main foil and which is used as the auxiliary foil. Thus, the designer can make the decision about the form of the design based on other factors, for example, cooling conditions, mechanical requirements, and so on.

5 Conclusions

This thesis aims at developing a new hybrid LC filter for power-electronic-converter-supplied motor drives. Such drives use pulse-width modulation that results in sequences of high-voltage high-frequency steep-edged signals. These signals contain a set of high harmonics not required for control issues. Harmonics cause reflections in the cable between the motor and the inverter leading to faster ageing of the motor winding insulation. Bearing failures and problems with electromagnetic compatibility may be also expected.

The filter proposed in this research work provides a very convenient design with integrated inductance and capacitance. This design not only proposes a solution that may be described as a traditional low-pass LC filter but also permits to minimize the stray impedances in the filter system.

The proposed hybrid LC filter is well compatible with the existent solutions of signal filtering in drive power electronics being thus relevant for filtration of both differential- and common-mode signals.

The key results of the work can be summarized as follows:

1. A new hybrid LC filter with common mode current damping properties and the filter construction are proposed.

Normally LC filters are built of separate components – inductors and capacitors. The hybrid LC filter has only a specially designed foil inductors: main and auxiliary foil layers isolated from each other and coiled on an air core. The main foils can be connected between the inverter and the motor cable. The auxiliary foils of the three-phase filters are connected together to create paths for the differential noise, and they can be connected to the DC link to guarantee a path for the common-mode currents. This way, there is a considerable capacitance between the main foils and the auxiliary foils. To the author's knowledge, the internal capacitance of a foil choke has not been used before to improve attenuation properties of filters in power drives. The additional auxiliary foil layer proposed in this work allows to use this considerable capacitance and to create LC filters without any additional capacitors. A second role of the auxiliary foil is to minimize the intra capacitance between the turns of the main foil.

2. Design principles of the LC filter are developed.

A specific feature of the proposed filter is its integrated inductance and capacitance. Therefore, the required attenuation properties of the hybrid LC filter are tightly related to its dimensioning. The new design method based on different existing and well-proven methods of electrical engineering is proposed in Chapter 2. It is possible to state that by increasing inductance and decreasing capacitance, low-cost solutions can be achieved. Considering the geometric dimensions, this means as low heights and as large outside diameters as possible in actual applications.

3. The electrical representations of a hybrid LC filter at low and high frequencies are proposed.

It is shown for the first time and verified by a number of tests with different prototypes in the frequency domain that at low frequencies the hybrid LC filter can be described as a regular LC filter. No hidden capacitances have to be taken into account. High frequency analysis in Chapter 3 shows that the system can be described by distributed parameters. A

total system representation is very difficult and complicated because of mutual couplings between the foils. This was the reason to develop a new lumped model that permits to evaluate the filter behaviour with the help of present-day computer facilities.

4. The behaviour of a hybrid LC filter as a part of an actual drive with a long cable is considered.

It is proven for the first time by a number of practical tests that the new hybrid filter provides a desired decrease in the pulse rise speed and proposes very good common-mode attenuation. With that, the hybrid LC filter demonstrates its LC nature by essential overshoots, which can be attenuated with external resistors. The test and analysis showed that the most suitable arrangement is to connect those ends of the auxiliary foils in star that correspond to the output terminals of the hybrid LC filter columns.

The results of this thesis are intended to be used both in practical development work and in further research. The proposed hybrid LC filter is practice oriented and provides a very suitable compact and inexpensive solution for modern drive applications. The presented calculation basis and recommendations can be applied not only to the hybrid LC filter design but also to conventional LC filters. Models and representations at low and high frequencies may be used in the simulation of a power drives with PWM converters and the analysis of hybrid LC filter behaviour during the design of the drive.

This thesis also aims at providing a basis for future investigations of the new design. An interesting practical research approach could be to study the use of a lossy ferromagnetic core material to partially replace the air core. Such an iron core may generate enough losses to replace the separate resistors used to damp significant oscillations resulting from the LC nature of the filter. Investigations of the hybrid LC filter temperature modes could facilitate in optimizing the filter design. This means that thermal models that are useful in practice as well as further research work are required. An open question is the behaviour of hybrid filters in large-scale drives. Special studies could be done in this field. Applicability of the proposed construction to sinusoidal filter design may also be considered, although it may lead to excessive filter dimensions. A solution to this problem can probably be found with multi-foil hybrid LC filters, which can increase the useful capacitive content. The analysed solution may also be implemented in small-scale, and not only in drive applications. This field may also be taken under consideration, and its future prospects are quite promising.

References

- ABB, 1995. *Frequency converters ACS 501 2.2 to 75 kW: User's Manual*. Helsinki, ABB Industry Oy.
- Ahola, J., 2003. *Applicability of Power-Line Communications to Data Transfer of On-Line Condition Monitoring of Electrical Drives*. Dissertation. Acta Universitatis Lappeenrantaensis 157. Lappeenranta University of Technology, Finland.
- Akagi, H. and Tamura, S., 2005. "A Passive EMI filter for Eliminating Both Bearing Current and Ground Current From an Inverter-Driven Motor." In *Power Electronics Specialists Conference, PESC'2005*, Recife, Brasil, pp. 2442–2450.
- Arrillaga J. and Watson N. R., 2003. *Power System Harmonics*. Chichester: John Wiley & Sons Ltd, pp. 269–286.
- Basavaraja, B., Sarma, V.S.S., 2008. "Analysis of the overvoltages in PWM-inverter fed induction motors". In *TENCON 2008 IEEE Region 10 Conference*, Hyderabad, India, November 18–21, 2008, pp. 1–6.
- Bentley, J. M., 1997. "Evaluation of Motor Power Cables for PWM AC Drives." *IEEE Transactions on Industry Applications*, March-April, 1997, Vol. 33, No. 2, pp. 342–358.
- Binder, A. and Muetze, A., 2007. "Scaling Effects of Inverter-Induced Bearing Currents in AC Machines." In *Proceedings of IEEE International Electric Machines & Drives Conference, IEMDC'2007*, Antalya, Turkey, May 3–5, 2007, pp. 1477–1483.
- Boglietti, A. and Carpaneto, E., 1999. "Induction motor high frequency model." In *Conference Record of the 34th IEEE-IAS Annual Meeting, IAS'99*, Phoenix, AZ, vol. 3, pp. 1551-1558.
- Boldea I. and Nasar S., 2002. *The Induction Machine Handbook*. Boca Raton: CRC Press, pp. 385–386.
- Bossche A. van den and Valchev, V., 2005. *Inductors and transformers for power electronics*. Boca Raton: CRC Press.
- Busse, D., Erdman, J., Kerkman, R., Schlegel, D. and Skibinski, G., 1995. "Bearing Currents and Their Relationship to PWM Drives." In *Proceedings of International Conference on Industrial Electronics, IECON'1995*, Orlando, FL, November 6–10, 1995, Vol. 1, pp. 698–705.
- Chen, S, Lipo, T. A. and Novotny, D. W., 1998. "Circulating Type Motor Bearing Current in Inverter Drives." *Industry Applications Magazine*, Vol. 4, No. 1, pp. 32–38.
- Consoli, A., Oriti, G., Testa, A. and Julian, A.L., 1996. "Induction Motor Modeling for Common Mode and Differential Mode Emission Evaluation." In *Conference Record of the 31st IEEE-IAS Annual Meeting, IAS'96*, San Diego, CA, vol. 1, pp. 595-599.
- Doležel, I., Valouch, V. and Škramlík, J., 2000. "High Frequency Models of Transistor Voltage Inverter-Fed Induction Motor Drives." In *Proceedings of IEEE International Conference on Industrial Technology, ICIT'00*, Goa, India, vol. 2, pp. 32-37.

Dorf R. C. and Bishop R. H., 1991. *Modern Control Systems*, 6th edition. Boston: Addison-Wesley.

Du Pont Teijin Films, 2003. Product Information: Mylar Polyester Film (Electrical Properties). [online], [Accessed 10 May 2009], http://usa.dupontteijinfilms.com/informationcenter/downloads/Electrical_Properties.pdf.

Du Pont, 2000A. Technical Data Sheet: Nomex Type 410. [online], [Accessed 10 May 2009], http://www2.dupont.com/Nomex/en_US/assets/downloads/energy_solutions/410.pdf.

Du Pont, 2000B. Technical Data Sheet: Nomex Type 418 and 419. [online], [Accessed 10 May 2009], http://www2.dupont.com/Nomex/en_US/assets/downloads/energy_solutions/418_419.pdf.

El-Husseini M., Venet P., Rojat G. and Joubert C., 2002. "Thermal Simulation for Geometric Optimization of Metallized Polypropylene Film Capacitors." *IEEE Transactions on Industry Applications*, Vol. 38, No. 3, pp. 713–718.

Erdman, J. M., Kerkman, R. J., Schlegel, D. W. and Skibinski, G.L., 1996. "Effect of PWM Inverters on AC Motor Bearing Currents and Shaft Voltages." *IEEE Transactions on Industry Applications*, Vol. 32, No.2, 1996, pp. 250–259.

Esmaeli, A., 2006. "Mitigation of the Adverse Effects of PWM Inverter Through Passive Cancellation Method." In *Proceedings of International Symposium on Systems and Control in Aerospace and Astronautics, ISSCAA'2006*, January 19–21, 2006, pp. 747–751.

Esmaeli, A., Sun, Y. and Sun, L., 2006. "Mitigation of the Adverse Effects of PWM Inverter Through Active Filter Technique." In *Proceedings of International Symposium on Systems and Control in Aerospace and Astronautics, ISSCAA'2006*, January 19–21, 2006, pp 770–774.

Finlayson P., 1998. "Output filters for PWM drives with induction motors." *IEEE Industry Applications Magazine*, Vol. 4, Issue 1, pp. 46–52.

Gambica Association, 2002. "Variable Speed Drives And Motors: Motor Shaft Voltages And Bearing Currents Under PWM Inverter Operation, Report №2 (2nd edition)." [online], [accessed on 10 May 2009], <http://www.rema.uk.com/pdfs/Report%20No%202.pdf>.

Gambica Association, 2006. "Variable Speed Drives And Motors: Motor Insulation Voltage Stresses Under PWM Inverter operation. Report №1 (3rd edition)." [online], [accessed on 10 May 2009], http://www.rema.uk.com/pdfs/tech_rep_no_1_web.pdf.

Ha I. and Harbrough R., 1976. "A Lossy Element For EMC filters." *IEEE Transactions on Elecromagnetic Compatibility*, Vol. EMC-18, No. 4, November 1976, pp. 141–148.

Hanigovszki, N., Poulsen, J. and Blaabjerg, F., 2004. "A novel output filter topology to reduce motor overvoltage." *IEEE Transactions on Industrial Applications*, Vol. 40, No. 3, pp. 845–852.

Hongfei, M., Dianguo, X. and Lijie, M., 2004. "Suppression Techniques of Common-Mode Voltage Generated by Voltage Source PWM Inverter." In *Proceedings of Power Electronics and Motion Control Conference, IPEMC'2004*, August 14–16, Vol. 3, pp. 1533–1538.

Hoppler, R. and Errath, R., 2007. "Motor bearings, not just a piece of metal." In *Cement Industry Technical Conference Record*, Charleston, SC, April 29–May 2, 2007, pp. 214–233.

- Horowitz P. and Winfield H., 1989. *The Art of Electronics*. Cambridge: University Press, p. 11.
- HP/Agilent 4194A Impedance/Gain-Phase Analyzer, 1996. Operation Manual. [online], [accessed on 10 May 2009], <http://cp.literature.agilent.com/litweb/pdf/04194-90011.pdf>.
- Isovolta, 2004. CALMICA® S 100 0902 Compoziție. [online], [accessed on 10 May 2009], http://www.isovolta.ro/pdf/R_CALMICA_S_100_0902.pdf.
- Isovolta, 2007. CALMICA® 70 0866, 70 0867 Description. [online], [accessed on 10 May 2009], http://www.isovolta.ro/pdf/R_CALMICA_70_0866_7.pdf.
- Jouanne A. von, Zhang H. and Wallace, A. K., 1998. “An Evaluation of Mitigation Techniques for Bearing Currents, EMI and Overvoltages in ASD Applications.” *IEEE Transactions on Industrial Applications*, Vol. 34, No. 5, pp. 1113–1122.
- Jouanne, A. von and Enjeti, P., 1997. “Design Considerations for an Inverter Output Filter to Mitigate the Effects of Long Motor Leads in ASD Applications.” *IEEE Transactions on Industrial Applications*, Vol. 33, No. 5, pp. 1138–1145.
- Kalantarov P. and Tseitlin L., 1986. *The calculation of the inductances*, 3rd edition (in Russian). Leningrad: Energoatomizdat, pp. 257–271.
- Kaufold M., Auinger H., Berth M., Speck J. and Eberhardt M., 2000. “Electrical Stress and Failure Mechanism of the Winding Insulation in PWM-Inverter-Fed Low-Voltage Induction Motors.” *IEEE Transactions on Industrial Electronics*, Vol. 47, No. 2, April 2000, pp. 396–402.
- Kazmierkowski M., Krishnan R. and Blaabjerg F., 2002. *Control in Power Electronics*. New York: Academic Press: pp. 89–160.
- Kerkman, R. J., Leggate, D. and Skibinski, G. L., 1997. “Interaction of Drive Modulation and Cable Parameters on AC Motor Transients.” *IEEE Transactions on Industrial Applications*, 1997, Vol. 33, No.3, pp. 722–731.
- Kuisma, M., Dzhankhotov, V., Pyrhönen, J., Silventoinen, P., 2009. “Air-Cored Common-Mode DC Filter with Integrated X and Y Capacitors”. In *Proceedings of 13th Conference on Power Electronics and Applications, EPE'2009*, September 8–10, 2009.
- Langsdorf A. S., 1955. *Theory of Alternating-Current Machinery*. 2nd edition. New York & London: McGraw-Hill.
- Lee S. and Nam, K., 2003. “Overvoltage Suppression Filter Design Methods Based on Voltage Reflection Theory”, In *Proceedings of Electric Machines and Drives Conference, IEMDC'2003*, June 1–4, 2003, Vol. 3, pp. 1808–1812.
- Leggate, D., Pankau, J., Schlegel, D. W., Kerkman, R. J. and Skibinski, G. L., 1999. “Reflected Waves and Their Associated Current.” *IEEE Transactions on Industry Applications*, 1999, Vol. 35, No. 6, pp. 1383–1392.
- Lide D., 2003. *Handbook of Chemistry and Physics*, 84th edition. Boca Raton: CRC Press, pp. 12-43–12-44, 12-219–12-220.
- McLyman C. W. T. *Transformer and Inductor Design Handbook (Electrical and Computer Engineering)*. New York – Basel: Marcell Dekker, Inc.

Mecker, S.L., 1992. "Considerations in Derating Induction Motors for Applications on Variable Frequency Drives." *Conference Record of 1992 Annual Pulp and Paper Industry Technical Conference*, June 8-12, 1992, pp. 191-197.

Mei, C., Balda, J. C., Waite, W. P. and Carr, K., 2003. "Minimization and Cancellation of Common-Mode Currents, Shaft Voltages and Bearing Currents for Induction Motor Drives." In *Proceedings of Power Electronics Specialist Conference, PESC'2003*, June 15–19, 2003, Vol. 3, pp. 1127–1132.

Mohan N., Underland T. M. and Robbins W. P., 2003. *Power Electronics: Converters, Applications and Design*. Hoboken (NJ): John Wiley & Sons Ltd.

Moreira, A. F., Santos, P. M., Lipo T.A. and Venkataramanan G. "Filter Networks for Long Cable Drives and Their Influence on Motor Voltage Distribution and Common-Mode Currents", *IEEE Transactions On Industry Electronics*, Vol. 52, No. 2, April 2005, pp. 515–522.

Muetze, A. and Binder, A., 2003. "Experimental evaluation of mitigation techniques for bearing currents in inverter-supplied drive-systems – Investigations on induction motors up to 500 kW." In *IEEE International Electric Machines and Drives Conference, IEMDC'2003*, June 1–4, 2003, pp. 1859–1865.

Mäki-Ontto, P., 2006. *Modeling and Reduction of Shaft Voltages in AC Motor Fed by Frequency Converters*. Dissertation, Helsinki University of Technology, Finland.

Ollila, J., Hammar, T., Iisakkala, J. and Tuusa, H., 1997. "On the bearing currents in medium power variable speed AC drives." In *IEEE International Electric Machines and Drives Conference Record*, 1997, Milwaukee (WI), May 18–21, pp. MD1/1.1–MD1/1.3.

Palma, L. and Enjeti P., 2002, "An Inverter Output Filter to Mitigate dv/dt Effects in PWM Drive System." In *Proceedings of IEEE Applied Power Electronics Conference, APEC'2002*, Dallas, TX, Vol. 1, pp. 550–556.

Palma, L., Morán, L. and Wallace, L. A., 2000. "A Simple and Cost Effective Solution to Reduce Motor Bearing Currents In PWM Inverter Drives." In *Proceedings of the 2000 IEEE International Symposium on Industrial Electronics, ISIE'2000*, Cholula, Puebla, Mexico, Volume 2, pp. 425–429.

Pavlic, T. P., 2008. Review of Circuits as LTI systems. [online], [accessed 12 July 2009], http://www.tedpavlic.com/teaching/osu/ece209/support/circuits_sys_review.pdf

Pohl, R.W, 1960. *Elektrizitätslehre*, 17th edition. Berlin-Göttingen-Heidelberg: Springer-Verlag.

Popović, Z. and Popović, B. D., 2000. *Introductory Electromagnetics*. New Jersey: Prentice Hall.

Prysmian, 2006. MCCMK 3½: 1 kV EMC power cable with PVC insulated copper conductors. [online], [accessed 10 May 2009], http://www.ms-proekt.ru/netcat_files/158_51.pdf.

Persson, E., 1992. "Transient Effects in Application of PWM Inverters to Induction Motors." In *IEEE Transactions On Industry Applications*, Vol. 28, No. 5, pp. 1095–1101.

Pyrhönen, J., Jokinen, T. and Hrabovcová, V., 2008. *Design of Rotating Electrical Machines*. Chichester: John Wiley & Sons Ltd.

Pyrhönen, J., Silventoinen, P., Kuisma, M., Dzhanhotov, V., 2009. "A Filter Appliance for a Multiphase Electrical Converter Device", Finnish Patent Application No. 20095541.

Rendusara, D.A. and Enjeti, P. N., 1998. "An Improved Inverter Output Filter Configuration Reduces Common and Differential Modes dv/dt at the Motor Terminals in PWM Drive Systems", *IEEE Transactions on Power Electronics*, Vol. 13, No. 6, pp. 1135–1143.

Robert, F., Mathys, P. and Schauwers, J.-P., 2001. "A Closed-Form Formula for 2-D Ohmic Losses Calculation in SMPS Transformer Foils." *IEEE Transactions on Power Electronics*, Vol. 16, pp. 437–444.

Salomäki, J., 2007. *Sensorless Control of AC Drives Equipped With an Inverter Output Filter*, Dissertation, Helsinki University of Technology, Finland.

Schlegel, D., Wrate, G., Kerkman, R., Skibinski, G., 1999. "Resonant Tank Motor Model For Voltage Reflection Simulations With PWM Drives." In *Electric Machines and Drives: International Conference IEMD '99 Digest*, pp. 463–465.

Schwartz M., 2002. *Encyclopedia of Materials, Parts and Finishes*. Boca Raton: CRC Press.

Shahruz, S. M., 2003. "Vibration of Wires Used in Electro-Discharge Machining (EDM)." In *Proceedings of IEEE Conference on Decision and Control*, 2003, December 9–12, 2003, Vol. 1, pp. 815–820.

Skibinski, G., Kerkman, R., Leggate, D., Pankau, J. and Schlegel, D., 1998. "Reflected Wave Modeling Techniques for PWM AC Motor Drives." In *Proceedings of Applied Power Electronics Conference and Exposition*, Anaheim (CA), February 15–19, 1998, Vol. 2, pp. 1021–1029.

Skibinski, G., Leggate, D. and Kerkman, R., 1997. "Cable Characteristics and Their Influence on Motor Overvoltages." In *Proceedings of Applied Power Electronics Conference and Exposition, APEC '1997*, Atlanta (GA), February 23–27, 1997, Vol. 1, pp. 114–121.

Skibinski, G., Tallam, R., Reese, R., Buchholz, B. and Lukaszewski, R., 2006. "Common Mode and Differential Mode Analysis of Three Phase Cables for PWM AC Drives." In *Conference Record of the IEEE Industry Applications Conference*, Tampa (FL), October 8–12, 2006, pp. 880–888.

Terman F.E., 1943. *Radio Engineers' Handbook*. New York and London: McGraw-Hill.

Weens Y., Idir N., Franchaud J.J. and Bausiére R., 2005. "High Frequency model of a shielded 4-wire energy cable". In *EPE '2005*. Dresden, September 11–14, 2005, pp. P1–P10.

Yokogawa, 2000. *PZ4000 Power Analyzer User's Manual*, 2nd edition. [online], [accessed on 10 May 2009], http://gscatalogs.us.yokogawa.com/im/TMI&Recorders/IMs/Power/IM253710-01E_021.pdf.

Young, D.W., 1964. "Development and Use of a Single Curve to Predict the apparent inductance of toroidal inductors", *IEEE Transactions on Component Parts*, Vol. 11, No. 3, pp. 26–31.

Appendix A

AIR-CORE HYBRID LC FILTER – A DESIGN EXAMPLE

Let us consider as an example a hybrid LC filter used in the test setup. The structure of the hybrid LC filter is presented in Figure 4.3. Let us calculate the filter neglecting foil 2 (except the space it takes).

For the 22 kW AC induction motor and the 200 m cable described in Table 4.1 from (Gambica, 2006) we can determine that the pulse rise time should be $t_r > 1.3 \mu\text{s}$. We choose $t_r = 3.8 \mu\text{s}$ in order to have time reserve for experimental investigations.

The resonance frequency from Eq. (2.5)

$$f_r \approx \frac{1}{4t_r} = \frac{1}{4 \cdot 3.8 \cdot 10^{-6}} = 66 \text{ kHz.}$$

In accordance with the recommendations given in section 2.4, as a compromise between the number of turns, the volume of the materials used and the dimensions, we selected the hybrid LC filter aspect ratio h_D equal to 0.8.

For all filter windings we selected an aluminium foil, $d_{\text{main}} = 0.1 \text{ mm}$, $d_{\text{aux}} = 0.2 \text{ mm}$. We selected Nomex Type 418 as the insulator because of its good electrical and mechanical properties ($\epsilon_{\text{ins}} = 4.1$, $d_{\text{ins}} = 0.25 \text{ mm}$). The tightness of rolling in manufacturing is taken into account by a gap layer $d_{\text{gap}} = 0.14 \text{ mm}$ between each surface of the winding and the insulator.

Using the flow chart in Figure 2.4 with the help of program facilities such as MATLAB or Octave we can find the data describing the electrical and geometric parameters of one hybrid LC filter column. The program increases in cycles the inner diameter D_{in} , the outer diameter D_{out} and the height h of the hybrid LC filter. The limits and the steps of the changes in dimensions are determined by the user. The calculated data and the data measured from the real prototype are presented in Table A.1. For comparison, the last column of Table A.1 contains information on the relation between the measured and calculated values, which in the best case should be 1.

Table A.1. Calculated and measured values and their comparison.

Parameter	Calculated value	Measured value	Relation between measured and calculated values, times
Inner diameter of the coil D_{in} , mm	100	100	1
Outer diameter of the coil D_{out} , mm	180	180	1
Height h , mm	150	150	1
Number of turns N	20	20	1
Main inductance L_1 , μH	30	30	1
Main capacitance C_{b1} , nF	194	240	1.24
Intra capacitance C_i , nF	0.17	0.065	0.38

Let us consider a cycle of calculations with the inner diameter D_{in} , the outer diameter D_{out} and the height h chosen for the prototype.

The number of turns in accordance with (2.6)

$$N = \frac{r_{out} - r_{inn}}{d_{main} + d_{aux1} + d_{aux2} + n_f d_{ins} + 2n_f d_{gap}} = \frac{0.5 \cdot (183 - 100)}{0.1 + 0.2 + 0.1 + 3 \cdot 0.25 + 6 \cdot 0.15} = 20.24.$$

We choose $N=20$.

The main inductance L_1 was calculated as follows.

$$\text{Middle radius: } r_{mid} = \frac{D_{out} + D_{in}}{4} = \frac{183 + 100}{4} = 70.75 \text{ mm.}$$

$$\text{Thickness of the winding: } d_w = \frac{D_{out} - D_{in}}{2} = \frac{183 - 100}{2} = 41.5 \text{ mm.}$$

$$\text{Geometric relations: } \alpha = \frac{h}{2 \cdot r_{mid}} = \frac{145}{2 \cdot 70.75} = 1.025, \rho = \frac{d_w}{2 \cdot r_{mid}} = 0.29, \gamma = \frac{\rho}{\alpha} = 0.28.$$

Because $\alpha > 1$, we have to use Figure 2.6 (b). With that $\frac{1}{\alpha} = \frac{1}{1.025} = 0.98$. Now from Figures 2.6–2.7 we can find that $K_a = 0.7$ and $k = 0.15$.

Thus, the main inductance

$$L_1 = \frac{\pi}{4} \cdot \mu \cdot \mu_0 \cdot N^2 \cdot \frac{2 \cdot r_{mid}}{\alpha} \cdot (K_a - k) = \frac{\pi}{4} \cdot 1 \cdot 4\pi \cdot 10^{-7} \cdot 20^2 \cdot \frac{2 \cdot 0.07075}{1.025} \cdot (0.7 - 0.15) = 30 \text{ } \mu\text{H.}$$

The main capacitance can be estimated with Eq. (2.9)

$$C_b = \varepsilon \cdot \varepsilon_0 \cdot \frac{2\pi \cdot r_{mid} \cdot h \cdot N}{d_{ins}} = 4.1 \cdot 8.854 \cdot 10^{-12} \cdot \frac{2\pi \cdot 0.07075 \cdot 0.15 \cdot 20}{0.25 \cdot 10^{-3}} = 194 \text{ nF.}$$

The difference between the calculated and measured capacitance can be explained by the fact that the relative permittivity of Nomex is an average value provided by the manufacturer, as it is pointed out in the technical data sheet (Du Pont, 2000B).

Resonance frequency can be determined with (2.11) and (2.12)

$$f_r = \frac{1}{2\pi \sqrt{L_1 C_b}} = \frac{1}{2\pi \sqrt{30 \cdot 10^{-6} \cdot 194 \cdot 10^{-9}}} = 66 \text{ kHz,}$$

which is the same as the required resonance frequency obtained from Eq. (2.5).

Filter corner frequency in accordance with (2.21)

$$f_c \approx \frac{0.25}{\sqrt{30 \cdot 10^{-6} \cdot 194 \cdot 10^{-9}}} = 103.6 \text{ kHz.}$$

Required common-mode attenuation range, according to section 2.1, is 250 kHz – 6 MHz. Thus, the filter should provide attenuation in the frequency range 103.6 kHz – 6 MHz.

Step response simulations can be easily performed with MATLAB 6.5. The model in Simulink is presented in Figure A.1. Similarly as in section 3.6, we used an input and output resistances $R_{in} = 0.5 \Omega$, $R_{out} = 1.3 \text{ k}\Omega$, which represent, to a certain degree, the drive application impedances per one phase near the resonance frequency f_r . Alternatively, more complicated model including motor differential-mode equivalent circuit, for instance, proposed by Ahola (2003), may be used. It was mentioned in section 3.5 that the magnetic coupling factor between the main and auxiliary foils obtains values in the range of 0.9 – 0.98. For further simulations we selected a coupling factor equal to 0.98.

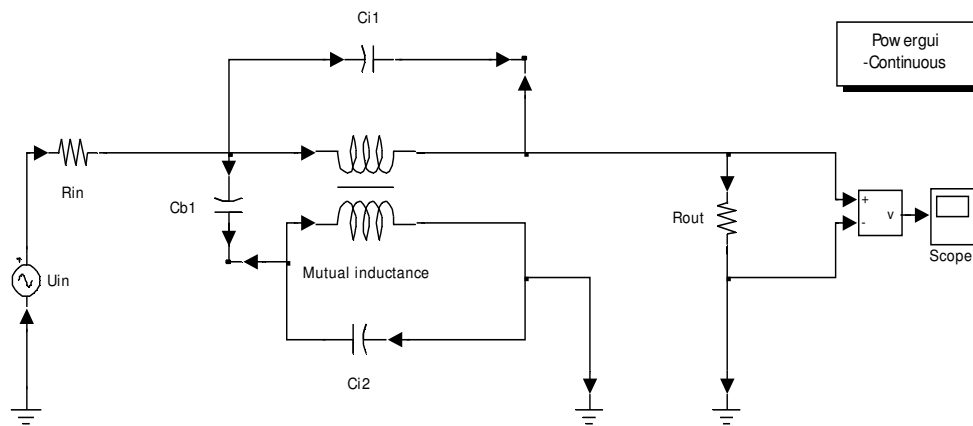


Figure A.1. Hybrid LC filter column model.

The simulation results of one column in the frequency domain are presented in Figure A.2 (a). According to our estimations, the intra capacitance of the main foil defined by equation (2.25) can be decreased to 1/15–1/16 if the auxiliary foil is activated. The model indicates that the calculated filter has resonance at the frequency of $f_r = 66 \text{ kHz}$, a corner frequency f_c at 101 kHz and provides attenuation in the frequency range of 101 kHz – 6.3 MHz fulfilling the determined frequency requirements. From 95.6 kHz up to 360 kHz the frequency response has a slope of approximately -40 dB/dec . Then, two resonances at 360 kHz and at 10 MHz take place. In this range, the filter column provides the best attenuation, -35 dB . At frequencies above 10 MHz there is deterioration of attenuation with the slope of about 40 dB/dec up to 100 MHz.

The simulation results of one column in the time domain are presented in Figure A.2 (b). The transient response has many oscillations with a maximum overshoot of 84% at the time instant $t_m = 7.7 \mu\text{s}$. The rise time $t_r = 3.9 \mu\text{s}$ is in accordance with the condition determined at the start of calculations. The phase-to-ground voltage rise speed in the considered case is $78 \text{ V}/\mu\text{s}$. The line-to-line voltage can be estimated if to scale voltage axis in accordance with the line-to-line voltage. In this case, the estimated rise speed is $194 \text{ V}/\mu\text{s}$. The presented simulation results are quite indicative if we take a look, for example, at Figure 4.10 (b).

\

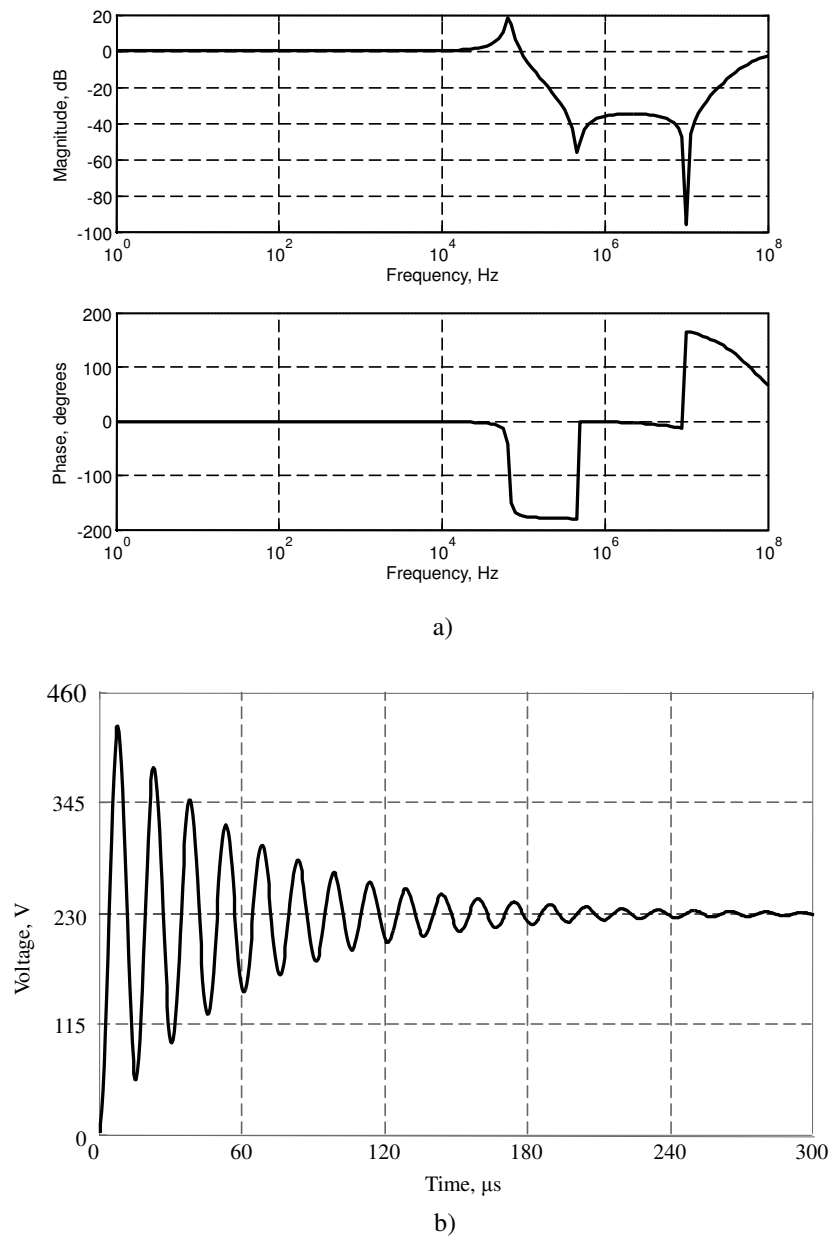


Figure A.2. Frequency (a) and time (b) responses for the calculated hybrid LC filter.

The SAMI GS inverter has an accessible DC link midpoint, and thus we can select the topology shown in Figure 1.18. The motor used in the test setup has a shaft height below 280 mm. In line with section 1.2.4, the probability of bearing failures in such motors is quite low and therefore no common-mode link is required. For the test purposes we considered also the topology with a common-mode link.

A simplified model with the HLCF at the chosen topology is presented in Figure A.3. We found LTspice very convenient for our estimations. In order to simplify simulations, we changed the inverter by three pulse sources generating in cycle the same illustration as shown in Figure 1.5 with rise and fall times equal to $0.2 \mu\text{s}$. Each source with a series resistance $R_{in} = 0.5 \Omega$ generates square voltage with an amplitude $1.35 \cdot \frac{U_{\text{DC-link}}}{2} = 270 \text{ V}$ and a frequency equal to the switching frequency in the test drive 2.14 kHz . For simplicity, we supposed that the earth potential and the potential of the middle point (internal drive neutral) are equal. We assumed that the cable has lumped parameters and a common-mode model of the motor was used in accordance with Ahola (2003) instead of the resistance R_{out} used in the model shown in Figure A.1. The cable capacitances in our common-mode model were short-circuited so that it was possible to neglect them. The inductance of our 200 m cable was found from Table 4.1: $L_{cab} = 50 \text{ mH}$. The parameters of the motor common-mode model were $L_{hf} = 145 \text{ nH}$, $C_{hf} = 4.9 \text{ nF}$ and $R_{hf} = 2 \Omega$.

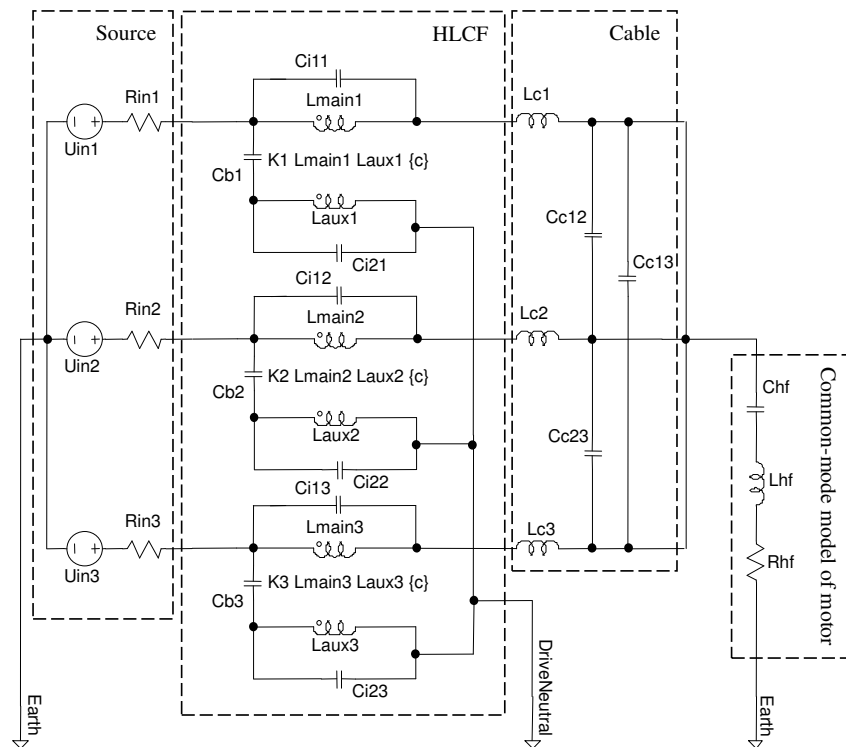


Figure A.3. Model for the common-mode simulations of the designed HLCF in LTspice IV.

Remembering that the real intra capacitance with a grounded foil can be 1/15 of its calculated value, we can get results of the common-mode simulations presented in Figure A.4. These results show that the common-mode current without filtration (peaks are about 3.5 A) can be decreased if the hybrid LC filter star-point is connected to the system neutral. In this case the common-mode current peaks are decreased to 0.4 A, that is, the noise level can be decreased to almost one ninth (19 dB), which is a very good value for practice. That is the reason to recommend the use of the common-mode link proposed by Rendusara and Enjeti (1998) for testing (Figure 1.18). These data of the simplified simulations are again quite indicative compared with the measured results in Table 4.2 and in Figure 4.12.

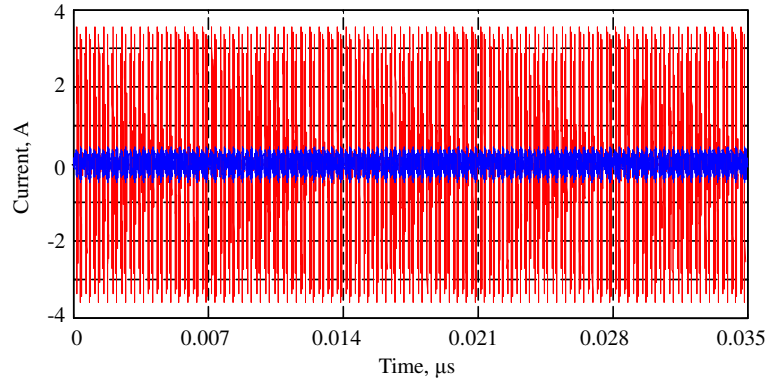


Figure A.5. Simulated common-mode current: red response – without HLCF, blue response – with the HLCF with earthing.

The thermal simulations were performed with the simplified 2D model in Students' QuickField version 5.6. The hybrid LC filter was replaced with a copper toroid with the same dimensions hanging in an air cage without any support. The external temperature of the cage is 20 °C. The axial cross-section was considered as shown in Figure A.5. The toroid generates heat with a volumetric heat density defined with the help of the phase current I_{ph} by equation

$$Q_t = \frac{I_{ph}^2 R_{dc}}{h \cdot \pi \left(\frac{D_{out}^2 - D_{in}^2}{4} \right)} = \frac{8 I_{ph}^2 \rho_{main} \cdot r_{mid} \cdot N}{h^2 \cdot d_{main} \cdot (D_{out}^2 - D_{in}^2)} = \frac{8 \cdot 43^2 \cdot 0.024 \cdot 10^{-6} \cdot 0.07075 \cdot 20}{0.15^2 \cdot 0.1 \cdot 10^{-3} \cdot (0.18^2 - 0.1^2)} = 10 \text{ kW/m}^3.$$

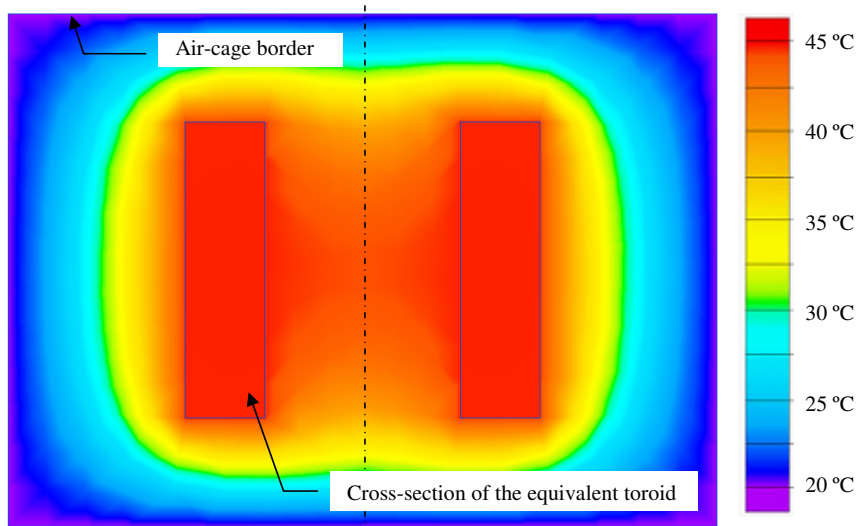


Figure A.5. Results of the hybrid LC filter thermal simulations in Students' QuickField.

In this case, the method of heat transfer is convection. As we can see from Figure A.5, heating up to about 50 °C is expected with natural cooling. This temperature is not harmful for the chosen insulator Nomex T418. Thus, no special cooling system is needed for our test purposes. The experimental results showed that the surface of the hybrid LC filter was also heating up to about 45–50 °C.

The columns can be placed symmetrically, as it is shown in Figure 4.3 (a), with a distance of 2–4 cm in order to eliminate their mutual thermal interaction (in accordance with Figure A.5) and to symmetry their mutual electromagnetic influence to prevent unbalances. For our test purposes we used a metallic box with a smooth surface as a cover in order to magnetically separate the filter and the environment. All the box surfaces are at a distance of about 4–5 cm from the columns. In an actual application, all the surfaces of such a box should be electrically isolated to prevent accidental electric short-circuits.

Table A.2 shows the comparison between the measured and calculated data for other two prototypes (Figure A.6), designed using the calculation technique presented in section 2.3. These prototypes were built for preliminary estimations and were not intended to work inside of a real drive.

Prototype 1 (Figure A.6 (a)) contains copper main and auxiliary foils, $d_{\text{main}} = d_{\text{aux}} = 0.1$ mm, each foil separated by a technical paper ($\epsilon_{\text{ins}} = 2.5$, $d_{\text{ins}} = 0.15$ mm). Prototype 2 (Figure A.6 (b)) contains copper main and auxiliary foils, $d_{\text{main}} = d_{\text{aux}} = 0.15$ mm, each foil separated by Mylar insulator ($\epsilon_{\text{ins}} = 3.3$, $d_{\text{ins}} = 0.13$ mm).

The calculation results are very close to the measured values especially for prototype 2 as a result of the tightest rolling between all three considered prototypes.

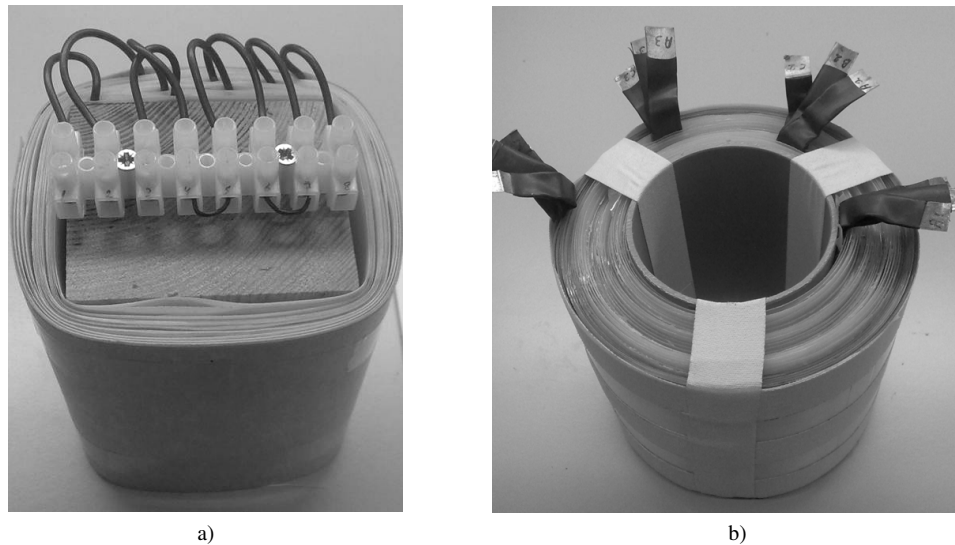


Figure A.6. Photographs of the preliminary prototype 1 (a) and prototype 2 (b).

Table A.2. Calculated and measured values and their comparison for the test prototypes.

Parameter	Calculated value		Measured value		Relation between measured and calculated values, times	
	Prototype 1	Prototype 2	Prototype 1	Prototype 2	Prototype 1	Prototype 2
Inner dimension, mm	80	75	80	75	1	1
Outer dimension, mm	120	128	120	128	1	1
Height, mm	100	100	100	100	1	1
Number of turns N	10	30	10	30	1	1
Main inductance, μH	5.3	50	5.2	47	0.98	0.94
Main capacitance, nF	38	215	40	210	1.05	0.98
Intra capacitance, nF	0.23	0.071	0.09	0.054	0.39	0.76

ACTA UNIVERSITATIS LAPPEENRANTAENSIS

311. RITVANEN, VIRPI. Purchasing and supply management capabilities in Finnish medium-sized enterprises. 2008. Diss.
312. PYNNÖNEN, MIKKO. Customer driven business model – connecting customer value to firm resources in ICT value networks. 2008. Diss.
313. AL NAZER, RAMI. Flexible multibody simulation approach in the dynamic analysis of bone strains during physical activity. 2008. Diss.
314. The Proceedings of the 7th MiNEMA Workshop. Middleware for Network Eccentric and Mobile Applications. Ed. by Pekka Jäppinen, Jouni Ikonen and Jari Porras. 2008.
315. VÄÄTÄNEN, JUHA. Russian enterprise restructuring – the effect of privatisation and market liberalisation on the performance of large enterprises. 2008. Diss.
316. DABAGHMESHIN, MAHSA. Modeling the transport phenomena within the arterial wall: porous media approach. 2008. Diss.
317. HAIMALA, JUHA. Supplier's position in project marketing networks. 2008. Diss.
318. UOTILA, TUOMO. The use of future-oriented knowledge in regional innovation processes: research on knowledge generation, transfer and conversion. 2008. Diss.
319. LAPPALAINEN, TOMMI. Validation of plant dynamic model by online and laboratory measurements – a tool to predict online COD loads out of production of mechanical printing papers. 2008. Diss.
320. KOSONEN, ANTTI. Power line communication in motor cables of variable-speed electric drives – analysis and implementation. 2008. Diss.
321. HANNUKAINEN, PETRI. Non-linear journal bearing model for analysis of superharmonic vibrations of rotor systems. 2008. Diss.
322. SAASTAMOINEN, KALLE. Many valued algebraic structures as measures of comparison. 2008. Diss.
323. PEUHU, LEENA. Liiketoimintastrategisten vaatimusten syntyminen ja niiden toteutumisen arviointi keskisuurten yritysten toiminnanohjausjärjestelmähankkeissa: Tapaustutkimus kolmesta teollisuusyrityksestä ja aineistolähtöinen teoria. 2008. Diss.
324. BANZUZI, KUKKA. Trigger and data link system for CMS resistive plate chambers at the LHC accelerator. 2008. Diss.
325. HIETANEN, HERKKO. The pursuit of efficient copyright licensing – How some rights reserved attempts to solve the problems of all rights reserved. 2008. Diss.
326. SINTONEN, SANNA. Older consumers adopting information and communication technology: Evaluating opportunities for health care applications. 2008. Diss.
327. KUPARINEN, TONI. Reconstruction and analysis of surface variation using photometric stereo. 2008. Diss.
328. SEPPÄNEN, RISTO. Trust in inter-organizational relationships. 2008. Diss.
329. VISKARI, KIRSI. Drivers and barriers of collaboration in the value chain of paperboard-packed consumer goods. 2008. Diss.
330. KOLEHMAINEN, EERO. Process intensification: From optimised flow patterns to microprocess technology. 2008. Diss.
331. KUOSA, MARKKU. Modeling reaction kinetics and mass transfer in ozonation in water solutions.

2008. Diss.

332. KYRKI, ANNA. Offshore sourcing in software development: Case studies of Finnish-Russian cooperation. 2008. Diss.
333. JAFARI, AREZOU. CFD simulation of complex phenomena containing suspensions and flow through porous media. 2008. Diss.
334. KOIVUNIEMI, JOUNI. Managing the front end of innovation in a networked company environment – Combining strategy, processes and systems of innovation. 2008. Diss.
335. KOSONEN, MIIA. Knowledge sharing in virtual communities. 2008. Diss.
336. NIEMI, PETRI. Improving the effectiveness of supply chain development work – an expert role perspective. 2008. Diss.
337. LEPISTÖ-JOHANSSON, PIIA. Making sense of women managers' identities through the constructions of managerial career and gender. 2009. Diss.
338. HYRKÄS, ELINA. Osaamisen johtaminen Suomen kunnissa. 2009. Diss.
339. LAIHANEN, ANNA-LEENA. Ajopuusta asiantuntijaksi – luottamushenkilöarvioinnin merkitys kunnan johtamisessa ja päätöksenteossa. 2009. Diss.
340. KUKKURAINEN, PAAVO. Fuzzy subgroups, algebraic and topological points of view and complex analysis. 2009. Diss.
341. SÄRKIMÄKI, VILLE. Radio frequency measurement method for detecting bearing currents in induction motors. 2009. Diss.
342. SARANEN, JUHA. Enhancing the efficiency of freight transport by using simulation. 2009. Diss.
343. SALEEM, KASHIF. Essays on pricing of risk and international linkage of Russian stock market. 2009. Diss.
344. HUANG, JIEHUA. Managerial careers in the IT industry: Women in China and in Finland. 2009. Diss.
345. LAMPELA, HANNELE. Inter-organizational learning within and by innovation networks. 2009. Diss.
346. LUORANEN, MIKA. Methods for assessing the sustainability of integrated municipal waste management and energy supply systems. 2009. Diss.
347. KORKEALAAKSO, PASI. Real-time simulation of mobile and industrial machines using the multibody simulation approach. 2009. Diss.
348. UKKO, JUHANI. Managing through measurement: A framework for successful operative level performance measurement. 2009. Diss.
349. JUUTILAINEN, MATTI. Towards open access networks – prototyping with the Lappeenranta model. 2009. Diss.
350. LINTUKANGAS, KATRINA. Supplier relationship management capability in the firm's global integration. 2009. Diss.
351. TAMPER, JUHA. Water circulations for effective bleaching of high-brightness mechanical pulps. 2009. Diss.
352. JAATINEN, AHTI. Performance improvement of centrifugal compressor stage with pinched geometry or vaned diffuser. 2009. Diss.

